UNIVERSIDADE DE ÉVORA

Numerical study of the tidal disruption of stars by the supermassive black hole Sgr A* in the Galactic Center

---

João Pedro Mendes Rocha

Thesis submitted to the Universidade de Évora
in partial fulfilment of the requirements for the degree of
Ph.D. in Computational Astrophysics

Supervisor *Prof. Doctor Miguel Ângelo Pignatelli de Avillez*

July, 26, 2019

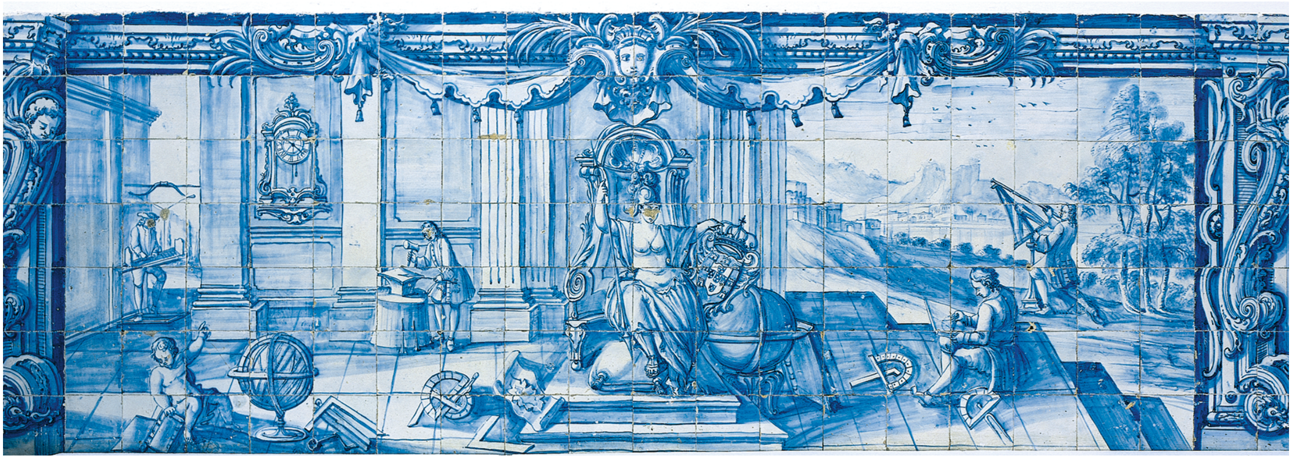

INSTITUTO DE INVESTIGAÇÃO E FORMAÇÃO AVANÇADA

UNIVERSIDADE DE ÉVORA

School of Sciences and Technology

Department of Mathematics

Numerical study of the tidal disruption of stars by the supermassive black hole Sgr A* in the Galactic Center

João Pedro Mendes Rocha

Supervisor *Prof. Doctor Miguel Ângelo Pignatelli de Avillez*

Ph.D. in Computational Astrophysics

Thesis

July, 26, 2019

I dedicate this thesis to the love of my life Leonela, my daughters Catarina and Joana and to my mother.

Acknowledgments

I would like to thank first of all to my supervisor Prof. Dr. Miguel de Avillez who gave me the chance to work in such an interesting topic as tidal disruption events and their feedback. His knowledge and physical insight of the problem as well as, his constant support gave me the will to pursue such complicated matter and keep finding the best ways to reach my objectives.

A special thanks goes to Prof. Dr. João Corte Real† for his support, advice and friendship. He will be always remembered.

I also would like to express my thanks to Prof. Dr. Ana Sampaio, Prof. Dr. Alfredo Palace de Carvalho and Prof. Dr. António da Silva with whom I had the privilige to strongly interact during my graduate studies. Further thanks go to Prof. Dr. Marília da Conceição Pires and Prof. Dr. Paulo Correia that lectured courses in the Computational Astrophysics Ph.D. program.

A sincere thanks to Prof. Dr. Mourad Bezzeghoud with whom i started to work in the Geophysical Centre of Évora in advanced seismology and also to Prof. Dr. José Borges and Prof. Dr. Bento Caldeira, who also lectured me courses in the Master Science program in Geophysics.

I thank also to Prof. Dr. António Correia with whom i worked in applied geophysics and to Prof. Dr. Paula Faria and Prof. Dr José Carrilho for their support and recomendations.

Of course, I can not forget my colleagues in arms: Gervásio Jorge Anela, Nuno Sidónio Pereira, Nuno da Câmara Manoel and Jorge Coveiro. A friendly thanks for all the moments we had in this academic experience.

A thankful word to my treasured family for their remarkable support and encouragement that replenished my strength and will to acomplish this work.

This research was supported by the projects (lead in Évora by M.Avillez) "Hybrid Computing using Accelerators & Coprocessors - modelling nature with a novell approach" (HCUAC), InAlentejo program, CCDRA, Portugal (PI: M.Avillez), PRACE Fifth Implementation Phase Project (PRACE-5IP) (reference EINFRA-730913, European Comission) @ U.Évora, and "Enabling Green E-science for the SKA Research Infrastructure (ENGAGE SKA) @ U. Évora" (reference POCI-01-0145-FEDER-022217, funded by COMPETE 2020 and FCT). The calculations presented in this thesis were performed in the Xeon Phi cluster (1174 cores) of the Computational Astrophysics Group of the University of Évora funded by HCUAC project.

Contents

List of Figures

List of Tables

Abstract

A Super Massive Black Hole (SMBH) with a mass of $\sim 4 \times 10^6 M_\odot$ lurks in the center of the Milky Way known as Sagittarius A* (Sgr A*). Its presence affects both the Galactic Center (GC) interstellar gas, of which the central molecular zone is an example, as well as the stellar system in which it resides.

A direct effect of the presence of Sgr A* is the capture of objects, in particular stars, leaving a trace of of X-ray (soft and hard) and gamma-ray emissions. A secondary effect is the origin and powering of the Fermi Bubbles, large superbubbles extending 8 kpc above and below the GC. Their energetic content (10^{55} erg) points towards an origin due to the tidal disruption of stars that end up being captured into an orbit around the black hole. Such captures release up to 10^{53} erg of energy, which, at a rate of 1 capture every 10^5 years is enough to energize the Fermi Bubbles.

Two paramount issues require a detailed attention: (i) what is the amount of energy released in a Tidal Disruption Event (TDE) that is available to power the black hole's surrounding medium, and thus, the Fermi Bubbles and (ii) how is the energy injected into the Fermi Bubbles. This thesis deals with the first point of this quest and looks into the second issue.

When a star is scattered from its trajectory and enters in a fatal orbit onto the SMBH, the tidal forces of the black hole overcome the star's self-gravity disrupting it partially or completely. A fate that depends on the strength of the encounter, which is determined by the proximity of the star to the black hole. Therefore, in order to understand the evolution of the captured star and the energy that is released during the process, a parametric study of the evolution of TDEs, its dependence on the penetration parameter and of their orbit (parabolic and elliptic) was carried out using smoothed particle hydrodynamics simulations.

The main results of this work concern the passage of the star at pericentre and the effects on the stellar structure due to the tidal forces of the SMBH. One of such effects caused by these forces is known as the *pancake phase* as the star acquires a stretched shape during its passage at pericentre. Immediately after this passage the star will develop two tidal tails of debris (gas that is removed from the stellar surface) that can evolve into a narrow stream of gas and the tail faced on to the black hole will fall on a steady rate of accretion onto the compact object. The penetration parameter defines how deep the star falls onto the black hole and the amount of energy that is released by the star. TDEs that result from parabolic orbits represent the cases where larger amounts of energy is released for the surrounding medium in the galactic center and can contribute potentially to power up the Fermi Bubbles.

Keywords: Tidal Disruption Events, Black Hole, Galactic Centre, Fermi Bubbles, Hydrodynamics, X-rays

Resumo

Estudo numérico de eventos de disrupção de estrelas pelo Buraco Negro Super Massivo Sgr A* no Cento Galáctico

Um Buraco Negro Super Massivo (SMBH) com uma massa de $\sim 4 \times 10^6 M_\odot$ reside no centro da Via Láctea e é conhecido como Sagittarius A* (Sgr A*). A sua presença afecta tanto o gás interestelar do centro galáctico, do qual a Zona Molecular Central é um exemplo, assim como o sistema estelar no qual se inclui.

Um efeito directo da presença de Sgr A* é a captura de objectos, em particular estrelas, deixando vestígios de emissões de raios X e de raios gama. Um efeito secundário é a origem e energização das Bolhas de Fermi, superbolhas gigantes com cerca de 8 kpc que se estendem acima e abaixo do centro galáctico. O seu conteúdo energético (10^{55} erg) aponta no sentido da origem se dever a eventos de disrupção de estrelas que são capturadas numa órbita em torno do buraco negro. Estas capturas podem libertar até 10^{53} erg de energia que, á razão de uma captura a cada 10^5 anos poderá ser suficiente para energizar as Bolhas de Fermi.

Duas questões da maior importância exigem atenção detalhada: (i) qual a quantidade de energia libertada num evento de disrupção de uma estrela que fica disponível para alimentar o meio circundante ao buraco negro, e assim, das Bolhas de Fermi e (ii) como é injectada a energia nas Bolhas de Fermi. Esta tese trabalha na primeira questão e lança a atenção sobre a segunda questão.

Quando uma estrela é dispersada da sua trajectória e entra numa órbita fatal em direcção ao SMBH, as forças de maré gravitacional do buraco negro sobrepõem-se á autogravidade da estrela, promovendo a sua disrupção parcial ou total. Este destino depende da força com que o encontro ocorre e é determinado pela proximidade da estrela ao buraco negro. Assim e para compreender a evolução da estrela capturada e a energia que é libertada durante este processo, foi realizado um estudo paramétrico da evolução de eventos de disrupção de estrelas, da sua dependência do parâmetro de penetração e das suas órbitas (parabólicas e elípticas) usando simulações hidrodinâmicas de partículas.

Os resultados mais importantes obtidos neste trabalho são relativos á passagem da estrela no pericentro e os efeitos na estrutura estelar devido ás forças por efeito de maré gravitacional do SMBH. Um desses efeitos devido a estas forças é conhecido como a *fase da panqueca* uma vez que a estrela adquire uma forma achatada durante a sua passagem pelo pericentro. Imediatamente após esta passagem a estrela desenvolve duas estrias de detritos (gás que é removido da superfície da estrela) que evoluem para um longo e estreito sulco de gás e a estria voltada para o buraco negro será atraída numa taxa de acreção estável para o objecto compacto. O parâmetro de penetração define a profundidade com que a estrela é atraída para o buraco negro e a quantidade de energia que esta liberta.

Os eventos de disrupção de estrelas em órbitas parabólicas libertam mais energia para o meio circundante no centro galáctico e podem contribuir potencialmente para alimentar as Bolhas de Fermi.

Palavras-chave: Eventos de Disrupção, Buraco Negro, Centro Galáctico, Bolhas de Fermi, Hidrodinâmica, Raios-X

Abbreviations list

ADAF Advection Dominated Accretion Flow

ADIOS Advection Dominated Inflow Outflow Solutions

AGN Active Galactic Nuclei

AMR Adaptive Mesh Refinement

CR Cosmic Ray

CMZ Central Molecular Zone

FB Fermi Bubbles

GC Galactic Center

GCL Galactic Center Lobe

GR General Relativity

HD Hydrodynamics

Hz Hertz

IC Inverse Compton

MC Molecular Cloud

MHD Magnetohydrodynamics

MS Main Sequence

pc parsec

RIAF Radiative Inefficient Accretion Flow

Sgr A* Sagittarius A*

SPH Smoothed Particle Hydrodynamics

SMBH Super Massive Black Hole

SNe Super Nova explosion

SNR Super Nova Remnant

TDE Tidal Disruption Event

UV Ultra Violet

WMAP Wilkinson Microwave Anisotropy Probe

yr year

1

Introduction

1.1 Astrophysical context of Tidal Disruption Events (TDEs)

Over the years observational studies coupled with theoretical arguments established Sgr A* as the dynamical center of the galaxy and due to its mass concentration it should inevitably correspond to a Super Massive Black Hole (SMBH) (Balick and Brown 1974; Alexander 2005).

The black hole itself is surrounded by the stellar bulge of the GC and interacts gravitationally with it. Thus, when a star is scattered from its trajectory and approaches the black hole, it eventually comes to a distance where the tidal forces of the compact object act upon it producing deformation and even destryoing it. These effects take place at the pericentre distance (R_P) to the black hole that is limited by the tidal radius (R_T); R_P represents the boundary for a star to survive or to be destroyed during the encounter. If the star reaches a pericentre distance that is smaller than the tidal radius, the star will be destroyed because the tidal forces overcome the stellar self-gravity and shred the star.

The limit between survival and destruction is defined by the penetration parameter (b) which represents the relation between the pericentre distance and the tidal radius (Cheng et al. 2011; Guillochon and Ramirez-Ruiz 2013). If the star passes at R_P imparted on an orbit whith $b \leq 1$ it will suffer some deformation or even partial disruption but will keep its stellar core intact (Alexander 2005). On the other hand, with a penetration parameter $b > 1$, a stronger encounter occurs, the star suffers disruption and the stellar material is ripped off from the stellar surface and spreaded around due to the orbital energy imparted on the debris (Evans and Kochanek 1989). The latter will evolve into an elongated and narrow stream where a portion of it stays bound to the star and the other portion will be forcefully ejected into the surrounding medium.

The shocks induced by the debris can produce hot plasma ($\sim$ 10 keV) generating velocities of $\sim 10^3$ km s^{-1} that expand into the halo heating up the gas to $\sim$ 1 keV, producing thermal X-rays. The subsequent shocks due to the hot plasma injection can accelerate electrons to $\sim$TeV energies with radio emission through synchrotron radiation and gamma (γ) rays through Inverse Compton effect (Cheng et al. 2011).

Recent data from Fermi-LAT (Large Area Telescope) have unveiled two gigantic features in the gamma-ray emission with $\sim$ 10 kpc[1] ($\sim 50°$) above and below the GC known as the Fermi Bubbles (FB) (Guo and Mathews 2012). Such features may have their origin in a large episode of energy injection in the GC, like accretion events onto the black hole during the last $\sim 10^7$ yr.These accretion events may correspond to successive star captures that can lead to TDEs from the SMBH of the Milky Way. In fact the energy of the FB (10^{55} erg) implies that either 100 captures of stars (with release of 10^{53} erg/capture) occured in a short period of time or 10^4 Super Nova explosions (SNe; with a canonical explosion energy of 10^{51} erg) occured. Hence, energetic arguments favour TDEs as the source of the FB.

1.2 Previous studies of TDEs

The initial studies of TDEs by black holes started during the 1970s in the hope to explain the observations of Quasars[2] (Hills 1975; Young et al. 1977; Frank 1978). This attempt to explain Quasars by TDEs was soon abandoned due to the fact that it would require very high rates of TDEs in order to explain the Quasars and that would represent an unrealistically high stellar density rate in the center of galaxies. A few years later TDEs gained another interest with the work done by Rees (1988) that brought a more realistic view of TDEs by black holes with estimated mass between 10^6–$10^8 M_\odot$ and sustained the idea that TDEs could be used to detect black holes in the center of galaxies.

The trivial work on TDEs rates comprised the idea of a black hole surrounded in a star cluster, with an isotropic distribution of the stellar velocities. Due to two body interactions with other stars, their orbits can be altered and send an unlucky star towards the black hole that can be destroyed in a dynamical time. In this way there is a continuous supply of stars to the disruption zone of a black hole. If stars are lost to the black hole through fatal orbits then these orbits are in the "loss cone", which is the region where stars can fall onto the black hole (Frank and Rees 1976).

For smaller distances from the black hole the velocity variations due to gravitational encounters is not enough to refill the loss cone as Frank and Rees (1976) and Lightman and Shapiro (1977) determined. It seems that the majority of disrupted stars comes from the loss cone regime and a more diffusive regime with an associated energy E_{crit}. As this energy overwhelms the energy of circular orbits on the disruption zone, then stars heading to the black hole should describe approximately parabolic orbits (Magorrian and Tremaine 1999).

The observational results of the first views of the external galactic nuclei inside the black hole radius of influence came from the Hubble Space Telescope in the second half of the 1990s. The results were used to determine tidal disruption rates for the first time in real galaxies by Syer and Ulmer (1999). From these calculations they derived tidal disruption rates of $10^{-7} - 10^{-4}$ yr^{-1} Mpc^{-3} per galaxy, which was found later on to be too high. Wang and Merritt (2004) computed these rates using the relation for the black hole mass to stellar velocity dispersion MBH $- \sigma_*$ having determined the value of 10^{-5} for non dwarf galaxies of $\sim 10^{-5} yr^{-1} Mpc^{-3}$.

In the last years a considerable amount of work has been developed concerning TDEs by massive black holes. Some of these work treat TDEs in a Newtonian frame with moving stars around a black hole on

---

[1] 1 pc $= 3.08567758 \times 10^{18}$ cm

[2] Quasi Stellar Radio Sources or the "black tidal" model.

the Schwarschild[3] spacetime as in Tejeda and Rosswog (2013), where a generalized potential is used to study parabolic TDEs and new approaches with SPH codes. The importance of the penetration parameter on TDEs has also been studied by Guillochon and Ramirez-Ruiz (2013) that worked on the disruption of stars by SMBHs of $10^6 M_\odot$ in order to reach to a limit for a star to be destroyed. Finally and regarding the relativistic aspect of TDEs, some of the previous work concerns the TDEs by rotating black holes with the relativistic hydrodynamical evolution of the fluids with Newtonian SPH codes, e.g., Tejeda et al. (2017).

1.3 The relation between stars and the SMBH

The relation between stars and the SMBH varies according to their mass ratios such that stars whose orbits are near the black hole may be treated as test particles, where the gravitational potential is dominated by the black hole. Stars may survive to it if these lie outside the event horizon or if they escape the black hole's R_T. For an approximation to first order, stellar orbits that have pericentre distances similar to those of the gravitational radius can be interpreted as keplerian (Guillochon et al. 2014b) or if observational data is accurate enough, post-Newtonian effects can be detected in those orbits and so a relativistic approach (probing the General Relativity, GR) must be taken into account (Alexander 2005).

The stellar density at the surroundings of the SMBH is very high and due to the presence of a high number of stars near the black hole these cannot be treated as a particle mass if stars are close enough to the compact object, because effects of tidal distortions and disruption itself are likely to occur (Rees 1988). This proximity to the black hole by stars can lead to interactions which are relevant for the feeding of the black hole, potentially producing observable signals of its self existence.

The extreme environment of the $\sim$ 0.1 pc of the GC, where high densities, large orbital velocities and strong tidal field occur, make this central region of the galaxy suitable for stellar collisions (Alexander 2005). Tidal disruptions are the result of the interaction between stars and the SMBH. The estimated rate at which the SMBH captures a star is $\Gamma_t \sim 10^{-4} yr^{-1}$ to $5 \times 10^{-5} yr^{-1}$ according to more detailed calculations by Syer and Ulmer (1999); Ayal et al. (2000); Cheng et al. (2011); Strubbe and Quataert (2009).

When a star is scattered from pc distances, its eccentric orbit brings it to the vicinity of the black hole, where finally the star can no longer resist to the gravitational pull and the tidal forces of the black hole exerted on the star promote its disruption. This shredding of the star is only possible when the star's R_P is smaller then the black hole's R_T and in this scenario strong interactions between the star and the SMBH will occur. Considering such interactions, if a star crosses the event horizon of the black hole it will be completely shredded such no TDE can occur in this conditions and if the star passes the R_T without falling into the event horizon, tidal disruption will occur with the gaseous debris of the star being accreted by the black hole (Rees 1988; Hills 1975; Lightman and Shapiro 1977).

The length-scales that describe the tidal disruption of a star by the SMBH are the stellar radius (R_*), the Schwarzschild radius (R_S) and the tidal radius (R_T). These length-scales ratios can be determined in terms of their mass ratios and escape velocities by (Alexander 2005):

i) $R_T/R_* \sim (m/M_*)^{1/3}$,

ii) $R_T/R_S \sim (c/V_e)^2 (m/M_*)^{-2/3}$,

iii) $R_S/R_* = (c/V_e)^{-2}(m/M_*)$

with $V_e^2 = 2GM_*/R_*$, being the escape velocity from the surface of the star, c is the speed of light and $G \approx 6,67408 \times 10^{-8}$ cm$^3 kg^{-1} s^{-2}$ is the universal gravitational constant considering a solar type star[4].

---

[3] Known as the Schwarschild solution, describes the gravitational field outside a spherical mass assuming that the electric charge of the mass, angular momentum and universal cosmological constant are zero.

[4] $M_* = 1M_\odot, R_* = 1R_\odot; 1M_\odot$ - 1 solar mass; $1R_\odot$ - 1 solar radius

Both the star and the black hole have physical properties that contribute to the nature of the encounter, like the stellar self-gravity, the black hole tidal field or the gas pressure. So if these effects are not taken into account by the time of disruption, the star particles may have free-fall trajectories under the gravitational pull of the black hole (Kochanek 1994). After the event, the stream of the disrupted gas achieves a complete orbit around the black hole and self-intersection of the stream debris can occur producing shocks. As long as $R_P > R_T$ the tidal interaction lasts for $\sim \tau_t b^{3/2}$ ($b = R_T/R_P$ is the penetration parameter and τ_t is the dynamical timescale). As the tidal interaction gets longer then the stellar dynamical timescale the hydrodynamics and the stellar self-gravity must be accounted for and so the limit for the disruption to take place must be determined, as the Newtonian limit is $R_T/R_S \geq 10$ and the General Relativity limit (GR) is $R_T/R_S \leq$ few (Alexander 2005).

1.4 TDEs outcome

There is a release of energy during the TDE which can be achieved by two distinct processes that complement each other. TDEs effects can last for $\sim 10^4$ yr. One of these effects is a luminous flare that occurs due to accretion that can take a few years and the other is a shock wave that is propagated through the ISM lasting for $\sim 10^5$ yr (Alexander 2005).

The properties of the TDEs in terms of its hydrodynamics and radiative pressure in the Newtonian and relativistic limits have been studied analytically and with simulations by different authors (Rees 1988; Kochanek 1994; Loeb and Ulmer 1997). Considering the results of the work achieved so far, a global frame for TDEs has emerged. To approach the TDE process there are some considerations to account for in terms of the energy involved. Initially the total energy of the system remains on the stellar binding energy, due to the star describing a parabolic orbit which implies that the star's orbital energy is $E_{orb} \simeq 0$.

The aftermath of the TDE is the extraction of the orbital energy of the star, unbinding it and accelerating the debris. On the initial stage, a portion of the mass of the star (M_{in}) is roughly $M_{in} \sim M_*/2$ and will become bound to the black hole with an initial energy (E_{in}) of $-E_{in} \gg E_*$. The other portion of the stellar mass (M$_{out}$), about $M \sim M_*/2$ will be ejected with an energy E$_{out}$, such $+E_{out} \gg E_*$ and $E_* = E_{in} + E_{out}$ (Alexander 2005). The dissipation mechanism can produce the emission of radiation or induce particle acceleration, where by the time of the last stable orbit of the gas, the energy can be extracted. Though, if the dissipation mechanism of the energy is to be inefficient, the heat can be transported through the flow (by advection) to the SMBH rest mass (Rees 1988; Narayan and Yi 1995).

The post disruption is dominated by the kinetic energy, where the debris self gravity and the gas pressure are to be dinamically insignificant inducing the stream to follow ballistic keplerian orbits. These orbits can be quite eccentric with $1 - \langle e \rangle = R_P/a = 2b(M_*/M_{BH})^{2/3}$, where e represents the eccentricity and a is the semi-major axis, with a large spreading of the orbital period (P) ranging from $P \to \infty$(R_a-apocentre distance) to the minimum period P_{min}, where $R_a \simeq R_T(M_{BH}/M_*)^{1/3}$ (Alexander 2005). The bound debris has a spread of energy which is $dM/dE =$ const (Evans and Kochanek 1989; Ayal et al. 2000). When tidal interactions are stronger corresponding to $R_P > R_S$, these leads to higher energy spreading with increasing debris return rate (Ulmer 1999; Evans and Kochanek 1989).

After the TDE an exotic phenomena can occur, producing a luminous flare. Such flare must combine the time for circularization of the debris and the time scale for the viscous dissipation to occur, both must be short enough for accretion to take place. The bound debris will circularize, driven by shocks due to the stream self-intersection that tend to return to the original point at R_P. After the second passage at R_P the debris can become unbound because of the heating and shocks, with $\sim M_*/4$ expected to stay bound to the SMBH (Ayal et al. 2000). There will be a rapid circularization of the debris and the corresponding timescale shall be $t_{circ} \sim \mathrm{few} \times P_{min}$ (Ulmer 1999).

TDEs can produce an observational signature due to tidal flares that may last for months to years in its luminous phase. As the return rate of the debris drops below the Eddington rate (a few years after a TDE) there will be an efficient cooling of the gas that will accrete to a thin accretion disc through a viscous timescale and the accretion disc is expected to decrease with time (Cannizzo et al. 1990). Though there is some discrepancy between the luminosity due to accretion and the one observed at the GC, as the luminosity from accretion of the debris from a past TDE is of $\sim 2-4$ orders of magnitude higher than the luminosity at the GC. This difference can be understood as most of the debris being blown off during the super-Eddington phase, which could stop early because the accretion disc could turn to a low radiative state with $\dot{M} \leq 10^{-2}\dot{M}_{Edd}$ or the outer parts of the disc become neutral, uncapable to support the magnetohydrodynamic (MHD) turbulence, therefore turning forcefully inviscid (Menou and Quataert 2001; Alexander 2005).

The evidences of TDEs in the GC can assume the form of energy release, in the sense that the energy of the debris that is ejected can present a long term signature of the disruption. TDEs can produce short flares on the UV/X-ray emission and during the propagation of the X-ray component (photons) from the SMBH, will meet clouds of gas and will be scattered into the line of sight in the 6.4 KeV kα (X-ray reflection nebula) with the X-ray emission being a potential signature of a TDE (Alexander 2005; Dogiel et al. 2009).

When a star describes an orbit where $R_T > R_P$ its trajectory lies outside the R_T and the star can survive to such an encounter with the black hole. This fortunate encounter of the star has nevertheless a consequence, which is the loss of orbital energy ($\Delta\varepsilon$). A star that keeps a near radial velocity during several orbital periods can cause the loss of the dissipational energy that will accumulate resulting in an orbital decrease that can lead to the inspiral of the star onto the SMBH (Alexander 2005). If the star keeps orbiting repeatedly under these conditions it can be destroyed by the black hole or can suffer disruption through the dissipational energy.

Though a close encounter by the star with the black hole is not a guaranty for the disruption to take place or for the star to achieve the final inspiral stage. The star may be a target for scattering during the inspiral timescale (which is orders of magnitude longer than the orbital timescale) which can suffer a deflection into a low angular momentum (J) orbit and then can experience a second scattering where it can enter in a loss-cone orbit, where it will be shredded. Stars that experience a non disruptive tidal encounter with the SMBH at the GC ($R_T > R_S$) get to be dispersed to larger orbits, though before reaching a safe survival orbit stars may experience some extreme effects such as tidal distortion, spinning and mass loss, that will constrain their evolution (Alexander 2005).

The fate of a star that suffers tidal inspiral (or tidal capture) is its disruption with consequent loss of stellar mass due to accretion onto the SMBH, being similar to the contribution of direct disruption as hypothesized by Frank and Rees (1976); Magorrian and Tremaine (1999). Tidal capture is less efficient then TDEs as mass contributor for the black hole due to inspiral processes that are much supressed when compared to direct infall and taking into account the scattering effects, it can be found that only a small fraction of mass contributes above that obtained by a TDE (Alexander and Hopman 2003).

The stellar debris resultant after disruption will evolve, forming a stream of gas that will return to the black hole in fallback. An accretion disc is likely to form due to circularization of the stellar debris, where viscous accretion will contribute for the emission of a thermal flare in the UV/X-ray, which in turn can be related to radio signals due to a relativistic jet that can have its origin in the inner region of the disc (Bonnerot et al. 2016).

The stellar debris rate can decrease by $t^{-5/3}$ (Lacy et al. 1982; Rees 1988; Evans and Kochanek 1989) in terms of the fallback onto the SMBH, though this rate can be dependent of the stellar structure. The accretion disc formation concerns several aspects that play a role in this process, mainly, the dissipation of the kinetic energy of the stellar debris, where the new disc will be injected with thermal energy (Bonnerot et al. 2016).

The mechanisms that may be responsible for the energy transfer and relative efficiency are the pancake shock and self-intersection. The energy transfer efficiency due to the pancake shock means that a fraction of the stellar material of the disrupted star is forcefully sent out of the initial ortbital plane resulting in the debris bound in the stream orbits in a range of inclinations and it intersects vertically the orbital plane near pericentre leading to the formation of a pancake shock due to strong compression. The self-intersection of the stream results from the meeting portions of the incoming debris and the outgoing counterpart that collide and produce shocks (Evans and Kochanek 1989; Alexander 2005).

Accretion discs are process dependent in terms of the efficiency due to circularization, viscous accretion and radiative cooling, where the timescales of these processes can be described respectively by t_{circ}, t_{visc} and t_{cool} (Alexander 2005). Considering different regimes of disc formation to take place if $t_{visc} < t_{circ}$ means that the viscosity may influence the circularization process. If $t_{visc} > t_{circ}$, accretion will occur after the disc formation. With $t_{cool} < t_{circ}$ the disc will be thin due to radiative cooling and finally if $t_{circ} < t_{cool}$ the disc will burst up during its formation because of the excess of thermal energy (Bonnerot et al. 2016). For the Milky Way case, at present time there is no evidence of an accretion disc at the GC (Alexander 2005).

1.5 Objectives of the current work

Many studies have been made about TDEs and the relation between stars and black holes in general, as in Frank and Rees (1976); Lacy et al. (1982); Evans and Kochanek (1989). There is today a more clear understanding about how TDEs occur and how stars that enter in the fatal influence of black holes suffer the effects of tidal forces from these massive compact objects. Most of the work done on this matter relates stars with black holes of masses $\sim 10^6 M_\odot$. It is known that the galactic SMBH has an estimated mass of $\simeq 4 \times 10^6 M_\odot$ (Ferrarese and Merritt 2000) and that its mass is $\sim$ 1/500 of the stellar bulge mass where it resides (Alexander 2005).

The discovered Fermi Bubbles at the GC have unveiled questions about its origin and energetics. As TDEs can release significant amounts of energy to the surroundings of the GC, these represent a good tool to trace the possible contribution for feeding the FB with the energy released from TDEs. Therefore, one strong motivation for this work is to have a better understanding of TDEs on stars that are disrupted by the SMBH Sgr A* and the amounts of energy that can be released in such events.

For this work two sets of simulations of TDEs with a solar type star falling on parabolic and elliptic orbits onto the SMBH were implemented. The recent Smoothed Particle Hydrodynamics code Phantom (Price et al. 2017) was used in these simulations.

1.6 Structure of the thesis

This thesis is structured as follows: Chapter 2 deals with the physical mechanisms of the disruption of a solar type star by the SMBH Sgr A* at the center of the Milky Way. The influence of the SMBH in the surrounding medium over stars is described in terms of the strong correlation between the black hole and the stellar velocity dispersion of the host galaxy (Tremaine et al. 2002).

The tidal disruption rates at which stars are deflected to the loss cone due to the gravitational encounters is described, where the two regimes of the loss cone theory define the rates at which stellar disruptions occur. The pericentre approach of the star to the black hole is characterized by a parabolic orbit and the penetration parameter at which the star crosses the R_P, where the tidal forces from the black hole exert distortions and deformation on the stellar surface until it disrupts the star in the case of the deeper encounters (Rees 1988) . As the star plunges onto the black hole it enters in the fallback phase and the star is splitted in distinct portions of matter.

The rate at the material falls back onto the black hole is characterized by a decay rate where the stream of the debris resultant from disruption follows ballistic trajectories (Guillochon et al. 2014b) around the black hole and if relativistic effects would be taken into account the stream of the debris would enter in the accretion disc formation phase (Bonnerot et al. 2016), though this stage is not considered for this work, which treats the tidal disruption events under the keplerian regime.

The numerical method used in this work is briefly described in Chapter 3. This method deals with the fluid equations using discrete particles that are carried in the flow and the hydrodynamic properties are evaluated at particle positions. This method was initially developed by Lucy (1977) and Gingold and

Monaghan (1977). Lagrangian and Eulerian methods have a primary difference between them for the fluid representation, once the Eulerian method follows the behaviour of the fluid through a fixed volume in space and the Lagrangian method follows the behaviour of a part of the fluid with respect to other parts (Monaghan 1992).

Computing the density from a set of particles can be achieved with SPH (Price 2011) where every particles have constant mass and the volume is inversely proportional to the number of particles in the neighbouring area. A smoothing kernel turns the particle smoothed over a volume and the density at any point can be obtained by the sum of the masses that lie in the region weighted by this kernel (Gingold and Monaghan 1977). For this work the SPH code Phantom (Price et al. 2017) was used for the numerical simulations of TDEs.

In Chapter 4 the tidal disruption of a solar type star by a Schwarschild black hole with mass of $\sim 4 \times 10^6 M_\odot$ is investigated. Two sets of parabolic and elliptic TDEs were implemented with different penetration parameters in order to study the effects that the tidal forces produce on the star at R_P and immediately after. The energies involved in this process are imparted to the spread debris of the star, which in turn is related to the mass fallback rate decay. Also the tidal energy transfer is evaluated in terms of the kinetic energy of the star that is converted into thermal energy imparted from the resultant debris during the disruptive process.

Chapter 5 describes the energetics of TDEs in the GC with a brief description of the central SMBH of the Milky Way and a possible application to the Fermi Bubbles case. An approximation to the possible evidence of the so called *smoking gun* through the γ rays source and the energetics of the lobes that integrate the thermal energies at the same order of magnitude from those obtained in the TDEs from this work is also described. Of reference is the recent data from the XMM-Newton (Ponti et al. 2015; Ponti et al. 2019) which gathered new data from the central $1^\circ, 5$ parsec region of the Milky Way. The structures detected on the X-ray emitting band correspond to two bi-polar lobes which are symmetric in relation to the galactic plane. Due to their unknown origin, these might have been originated by some large episode of energy injection in the GC like Super Novae (SNe) or stellar capture processes Ponti et al. (2019) and may be attributed to the base of the Fermi Bubbles larger structure.

Chapter 6 closes this thesis with final remarks and future work.

2

Tidal Disruption Events

2.1 Introduction

A Super Massive Black Hole (SMBH) resides in the center of most of the galaxies, which is surrounded by a stellar cluster interacting gravitationally between them. From time to time, a star can be scattered from its quiescent state and enters on eccentric orbits (from pc distances) that approximates the star to the SMBH and leads to the disruption of the star by the tidal forces of the compact object (Rees 1988). This scenario is achieved when the star has a pericentre distance (R$_P$) shorter than the tidal radius (R$_T$). The rate of these encounters happen is approximately of one every $10^4 - 10^5$ yr (Cheng et al. 2011).

The pericentre passage of the star is characterized by its shredding by tidal forces from the black hole and the resultant material of this effect is spreaded in orbital energy (Guillochon and Ramirez-Ruiz 2013). The effects of the disruption on the star are somehow different, due to the typical encounters between the two objects. If the star suffers a weak encounter, the tidal effects of the black hole on it can result in a partial disruption where a self-gravitating core still holds to the interaction. In the case of a strong encounter the star can experience a strong compression that can result large amounts of thermal energy (Rees 1988). In any case the resultant debris, due to the orbital spreading, evolves into an elongated structure with a thin profile limited by self-gravity.

The portion of matter that stays bounded to the black hole and the one which is ejected overcoming the gravitational pull of the compact object can be as much as about a half for each portion. The material that escapes becoming unbound will interact with the surrounding medium with radio and γ-ray emissions. The bound material of the stream will eventually fall back to the compact object in a period of several days to a few months after the TDE occurs (Alexander 2005).

2.2 SMBH influence on surrounding stars

A SMBH can influence the stellar distribution and respective stellar orbits in the inner regions of its host galaxy. With a stellar density distribution in the galaxy of N_* and a well defined core of radius (R_C), the stellar velocity (σ) of the stars can be defined by (Rees 1988)

$$\sigma \simeq \left(\frac{GM_*}{R_C}\right)^{1/2}, \tag{2.1}$$

where M_* represents the stellar mass. If the SMBH has a mass $M_{BH} \ll N_* R_C^3$, with the stellar mass being $M_* \simeq N_* R_C^3$, the trajectory of a typical star would be preferentially influenced by other stars rather than by the black hole and the stellar dynamics can be dominated by the SMBH until a certain distance of influence (Rees 1988). The tidal disruption radius R_T is the distance to the SMBH at which a star can be disrupted by it and the largest distance in terms of R_T is called the *loss cone* radius R_{lc} (Merritt 2013).

The strong correlation between the black hole mass and the stellar velocity dispersion of the host galaxy follows the $M_{BH} - \sigma$ relation (Tremaine et al. 2002). This frame characterizes the initial phase of a TDE, as the velocity dispersion matches with the keplerian circular velocity and the initial conditions for the disruption of a star are satisfied. When star that is orbiting at a distance $R \gg R_T$ may be scattered and describe a trajectory that crosses the R_T where the angular momentum (J) falls below some critical value ($J \leq J_{crit}$, where $J_{crit} \equiv J_{lc}$). When the star reaches R_P and so lies inside the R_T its velocity vector falls onto the loss cone and the star will be shredded in a dynamical timescale (Frank and Rees 1976). At this time the angular momentum J must be smaller than that of the loss cone J_{lc} for an orbit where $R_P \leq R_T$ (i.e. $R_P \equiv R_{lc}$) and for a star that reaches the distance $R = R_{lc}$ the angular momentum is defined by (Merritt 2013)

$$J_{lc}^2 = 2R_{lc}^2[E - \Phi(R_{lc})] \approx 2GM_{BH}R_{lc}, \tag{2.2}$$

from this expression $|E|$ is the orbital energy with $|E| \ll GM_{BH}/R_{lc}$ which means that the star must be on an orbit where the semi-major axis *a* $\gg R_{lc}$ and Φ represents the gravitational potential. The expression *loss cone* is derived from the loss cone orbits, where $J \ll J_{lc}$ and can be defined by a set of velocity vectors at a distance R from the SMBH that are related with orbits that pass inside the R_{lc} and this condition is satisfied if the velocity vector of the star lies within a cone of semi-angle θ_{lc} (Figure 2.1) that can be approximated by (Merritt 2013)

$$\theta_{lc} \approx \begin{cases} (R_{lc}/R)^{1/2}, & R \lesssim R_{BH} \\ (R_{lc}R_{inf}/R^2)^{1/2}, & R \gtrsim R_{BH} \end{cases} \tag{2.3}$$

where R_{BH} is the SMBH gravitational field of influence and R_{inf} will be the influence radius of the SMBH, that is defined for the central velocity dispersion σ as (Merritt 2013)

$$R_{inf} \equiv \frac{GM_{BH}}{\sigma^2} \approx 2.25 \text{ pc} \left(\frac{M_{BH}}{10^6 M_\odot}\right)\left(\frac{\sigma}{200 \text{ km s}^{-1}}\right)^4, \tag{2.4}$$

considering the $M_{BH} - \sigma$ with the $M_{BH} \approx 1.8 \times 10^6 M_\odot$ with an estimated interval of 1.5 ± 2.2 for the Milky Way (Ferrarese and Merritt 2000). For the central black hole Sgr A* with a mass of $M_{BH} \approx 4.0 \times 10^6 M_\odot$ the radius of influence is $R_{inf} \approx 5.0\ pc$.

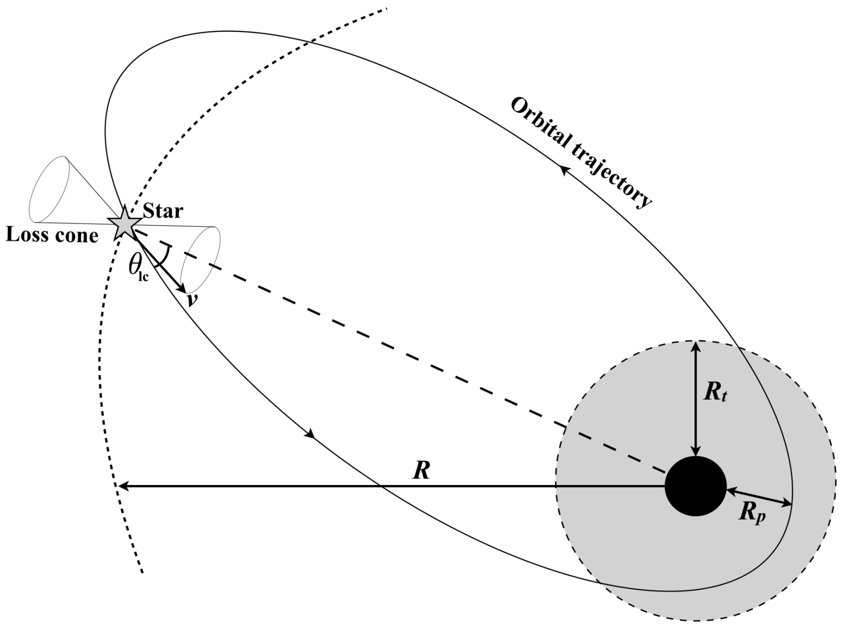

Figure 2.1: The orbital trajectory of a star inbound onto the black hole at the surface of the loss cone (Freitag and Benz 2002).

2.2.1 Relaxation time

When penetrating the loss cone, the star orbital elements suffers perturbations due to two-body encounters with other stars. These gravitational encounters have an associated timescale that corresponds to the *relaxation time* during which the stellar velocities have a variation of order unity with $\Delta\sigma \approx \sigma$ and for an infinite homogeneous medium the two-body relaxation time is (Spitzer 1987; Merritt 2010)

$$\begin{aligned} t_r &= \frac{0.33\sigma^3}{G^2\, M_*^2\, \rho\, ln(\Lambda)} \\ &= 1.272 \times 10^9 \left(\frac{\sigma}{200\ km\ s^{-1}}\right)^3 \left(\frac{M_*}{M_\odot}\right)^{-2} \left(\frac{\rho}{10^6 M_\odot\ pc^{-3}}\right)^{-1} \left(\frac{ln\Lambda}{15}\right)^{-1} yr \end{aligned} \tag{2.5}$$

with ρ representing the density of the stars, M_* is the mass of one star, σ is the velocity dispersion of the stars and the Coulomb logarithm is $\ln\,\Lambda$, which is roughly given by (Merritt 2010)

$$\begin{aligned} ln\Lambda &\approx ln\left(\frac{M_{BH}}{M_*}\right) \\ &\approx ln(N_h), \end{aligned} \tag{2.6}$$

where $N_h \equiv M_{BH}/M_*$ is the number of stars whose mass equals the M_{BH}.

2.2.2 Tidal disruption rates

At the GC, the rate of stellar scattering onto the SMBH, i.e., the number of stars that are deflected into the loss cone due to gravitational encounters with other stars can be represented by $F(\varepsilon)$ which describes the flux of stars into the loss cone and can be defined by (Wang and Merritt 2004)

$$F_{lc}(\varepsilon) = 4\pi^2 \Delta J^2(\varepsilon) \frac{f(\varepsilon)}{ln(R_0^{-1})}, \tag{2.7}$$

where ε is the orbital energy and $R_0(\varepsilon)$ represents the value of R for which f decreases to 0 as stars that scatter into the loss cone are removed, therefore the scattering of stars into loss cone orbits allows $f \neq 0$ even if $J < J_{lc}$. The approximation to $R_0(\varepsilon)$ can be defined by (Wang and Merritt 2004)

$$R_0(\varepsilon) = R_{lc}(\varepsilon) \begin{cases} exp(-q), & q(\varepsilon) > 1 \\ \\ exp(-0.186q - 0.824\sqrt{q}), & q(\varepsilon) < 1 \end{cases} \tag{2.8}$$

The typical change in angular momentum that a star receives in terms of the orbital period $P(\varepsilon)$ can be written as the ratio to the loss cone angular momentum defined by the function $q(\varepsilon)$ as (Cohn and Kulsrud 1978)

$$q(\varepsilon) \equiv \frac{\Delta J^2(\varepsilon)}{J_{lc}^2(\varepsilon)} = \frac{P(\varepsilon)}{t_J(\varepsilon)} \tag{2.9}$$

where $t_J(\varepsilon)$ is the typical time scale for stars during trajectories in angular momentum J_{lc} through two-body relaxation process such (Cohn and Kulsrud 1978; Lightman and Shapiro 1977)

$$t_J(\varepsilon) \approx \left(\frac{J_{lc}(\varepsilon)^2}{J_c(\varepsilon)} \right) t_r, \tag{2.10}$$

as t_r is the relaxation time from (2.5).

The function $q(\varepsilon)$ can be limited by two different scenarios:

(1) The empty loss cone rate is appropriate for $\Delta J \ll J_{lc}$, where ΔJ is the angular momentum for the stellar distribution, which means that the loss cone refills more gradually than it is depleted. When stars enter the loss cone the chances of being scattered out in an orbital period are very few, these are disrupted by the passage at pericentre R_P and the loss cone is essentially empty. This stage is known as the *diffusion limit* as stars diffuse towards the loss cone through many orbital periods

(2) The full loss cone rate is the opposite case and is set for $\Delta J \gg J_{lc}$ and is characterized by the *pinhole limit* where the stars scattering *per-orbit* is large when compared to the size of the loss cone

For an isotropic distribution of stars, the flux into the loss cone scales linearly with the tidal radius R_T due to the loss cone being full and the rate is size dependent of the loss cone ($J_{lc}^2 \propto R_T$). If the loss cone is empty, the variations in its size will not affect the rate, which is set by the diffusion process.

The pinhole and diffusion limits are the relevant limits which can be taken from (2.7) as (Lightman and Shapiro 1977)

$$F_{lc}(\varepsilon) \propto \begin{cases} J_{lc}^2 \propto R_T & q(\varepsilon) \gg 1(\text{pinhole}), \\ \\ ln(J_{lc}^2) \propto ln(R_T) & q(\varepsilon) \ll 1(\text{diffusion}). \end{cases} \tag{2.11}$$

In the empty loss cone and for time scales greater than the dynamical time t_{dyn} the loss cone will be empty. When a star is in the loss cone it will be removed in a dynamical time, so the capture rate $\dot{N}_{empty}$ is limited

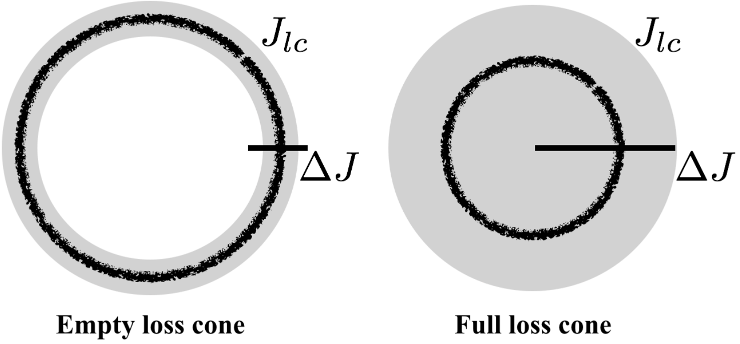

Figure 2.2: Empty and full loss cone regimes. The rate of the empty loss cone regime is set by the number density × the relaxation time (Novikov et al. 1992).

by diffusion into the loss cone and is given by (Syer and Ulmer 1999)

$$\frac{d\dot{N}_{empty}}{dN} = \frac{1}{ln(2/\theta_{lc})t_r}$$
$$\dot{N}_{empty} = \int_0^{R_{crit}} \frac{1}{ln(2/\theta_{lc})t_r} dN. \tag{2.12}$$

In the full loss cone stage there is an isotropic velocity dispersions and the portion of stars in the loss cone is simply θ_{lc}^2. In this case the capture rate $\dot{N}_{full}$ *per star* is

$$\frac{d\dot{N}_{full}}{dN} = \frac{\theta_{lc}^2}{t_{dyn}}$$
$$\dot{N}_{full} = \int_{R_{crit}}^{+\infty} \frac{\theta_{lc}^2}{t_{dyn}} dN \tag{2.13}$$

where N is the number of stars within a radius R. The total loss cone rate is therefore

$$\dot{N} = \dot{N}_{empty} + \dot{N}_{full} \tag{2.14}$$

and both rates are equal at a certain distance $R = R_{crit}$. The stellar tidal disruption rate for the GC of the Milky Way follows the rate of scattering of stars into the SMBH's tidal disruption sphere where $R \leq R_T$ and can be defined as (Merritt 2010; Wang and Merritt 2004)

$$\dot{N} = \int F_{lc}(\varepsilon) d\varepsilon. \tag{2.15}$$

Assuming solar type stars ($M_* = M_\odot; R_* = R_\odot$) and the $M_{BH} \approx 4 \times 10^6 M_\odot$, the consumption rate of the Milky Way's SMBH can be set as (Merritt 2010)

$$\dot{N} \approx 4.6 \times 10^{-4} \left(\frac{\sigma}{90 \text{ km s}^{-1}}\right)^{7/2} \left(\frac{M_{BH}}{4 \times 10^6 M_\odot}\right)^{-1} yr^{-1}. \tag{2.16}$$

2.3 The pericentre approach

As a star approaches the black hole at a distance where its periapsis R_P lies inside the tidal radius R_T, it will be tidally disrupted. The tidal forces from the black hole will be approximatelly equivalent to the star's self-gravity at a distance R_T. The self-gravity acceleration $a_G \approx GM_*/R_*^2$ and the tidal acceleration $a_T \approx GM_{BH}R_*/R^3$ can be equated in order to obtain the critical distance and therefore the tidal radius by R_T (Rees 1988)

$$\begin{aligned} a_G &\equiv a_T \\ \frac{GM_*}{R_*^2} &\equiv \frac{GM_{BH}R_*}{R_T^3} \\ R_T &\equiv \left(\frac{M_{BH}}{M_*}\right)^{1/3} R_*. \end{aligned} \tag{2.17}$$

For a typical solar type star ($M_* = 1M_\odot; R_* = 1R_\odot$) and a typical black hole of mass $M_{BH} = 10^6 M_\odot$ the tidal radius will be $R_T = 100R_\odot \approx 2.254 \times 10^{-6}$ pc. The Milky Way's SMBH with a mass of $M_{BH} = 4 \times 10^6 M_\odot$ will have a tidal radius of

$$R_T = 3.584 \times 10^{-6} \left(\frac{M_{BH}}{10^6 M_\odot}\right)^{1/3} \left(\frac{M_*}{M_\odot}\right) \left(\frac{R_*}{R_\odot}\right)^{-1/3} pc, \tag{2.18}$$

that is $R_T \approx 159R_\odot$. The strength of the encounter between the star and the black hole can be evaluated by a dimensionless impact parameter b defined by (Shen and Matzner 2014)

$$b \equiv \frac{R_T}{R_P}. \tag{2.19}$$

The orbit of the star can be characterized by its semi-major axis a_* and consequently by its eccentricity ecc (for bound orbits $0 \leq ecc < 1$). For higher values of ecc the debris produced during the disruption of the star will stay bound to the black hole, if $ecc \leq ecc_{crit}$ and so the eccentricity can be defined by (Hayasaki et al. 2016)

$$e < e_{crit} = 1 - \left(\frac{2}{b}\right)\left(\frac{M_{BH}}{M_*}\right)^{-1/3}. \tag{2.20}$$

and the semi-major axis is defined by (Bonnerot et al. 2016)

$$a_* = \frac{R_P}{1 - ecc}. \tag{2.21}$$

Considering, for example, the case of $b = 1$ and $M_{BH} = 10^6 M_\odot$ the orbit of the star with an eccentricity of $ecc = 0.8$ will have its semi-major axis of $a_* = 1.127 \times 10^{-5}$ pc. For the case of the Milky Way, stars that are inbound to the SMBH ($M_{BH} = 4 \times 10^6 M_\odot$) with a penetration parameter of $b = 1$, their orbits will be characterized by a semi-major axis of $a_* \approx 1.792 \times 10^{-5}$ pc. Associated to these orbits the correspondent orbital period of the star is defined by (Guillochon and Ramirez-Ruiz 2015)

$$P_* = 2\pi \left(\frac{GM_{BH}}{a_*^3}\right)^{-1/2} \tag{2.22}$$

For the resident SMBH ($M_{BH} = 4 \times 10^6 M_\odot$) of the Milky Way the orbital period of the star is $P_* \approx 31$ h (the star here is considered to be of solar type). TDEs can be detected if the event occurs out of the *event horizon*[1] of the black hole, which corresponds approximately to twice its gravitational radius (R_G)

---

[1] The limit where a particle reach the *point of no return*, i.e., the limit where the gravitational pull of the black hole is so high that even light cannot escape to it.

and is given by (Guillochon and Ramirez-Ruiz 2015)

$$R_G \equiv \frac{GM_{BH}}{c^2} = 1.911 \times 10^{-7} \left(\frac{M_{BH}}{10^6 M_\odot} \right) pc \tag{2.23}$$

where c is the speed of light and the mass of the SMBH is the typical value for the Milky Way's compact object.

Through the influence of tidal forces from the BH, the star that initially was in hydrostatic equilibrium starts to suffer deformation at a certain distance R_T and is gradually compressed with θ_T representing the true anomaly suffered by the star as it is confined by the two orbital planes that make an angle α between them (Figure 2.3). The gravitational pull stretches the star in a mean radial direction due to stellar elements near the black hole. Partial tidal disruption occurs when the penetration parameter is $b \approx 1$ and the star just scratches the tidal sphere making the self-gravitating core to escape to the pericentre passage (Bonnerot et al. 2016; Guillochon and Ramirez-Ruiz 2013).

As the star reaches the R_T the stretching can develop a quadrupole distortion achieving an amplitude of order unity by the time of disruption at R_T and the pressure that results from this stretching causes a spread in the orbital energy $\Delta\varepsilon$ of the debris Rees (1988). This is a consequence of the star being unaffected until it reaches the R_T where the trajectory of the debris is significantly modified. A decrease in orbital energy can relate the proximity of the stellar elements to the black hole rather than to the center of mass of the star, while an increase of this energy can relate further distances to the black hole by the stellar elements.

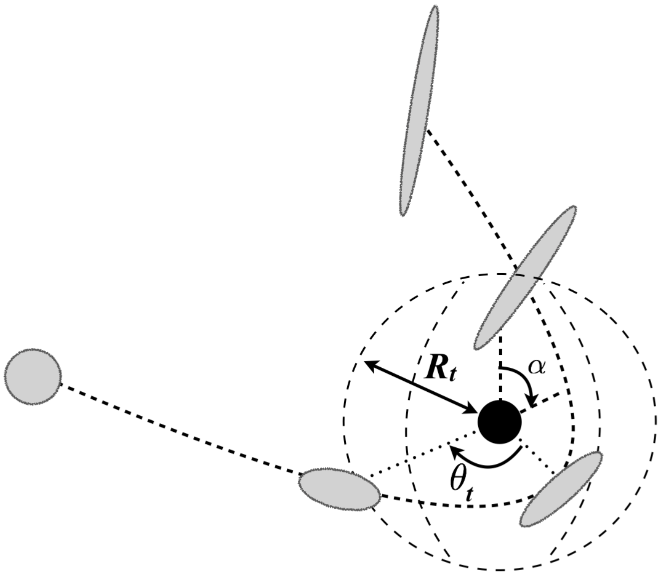

Figure 2.3: A star passing the pericenter of the black hole inside the tidal sphere on a ballistic trajectory (Coughlin 2016).

The evolution of the debris in this perspective is similar to the stellar binding energy (ε_b), with $\varepsilon_b \approx GM_*/R_*$ (Rees 1988; Evans and Kochanek 1989), that in fact satisfies $\varepsilon_b/\Delta\varepsilon \approx (M_{BH}/M_*)^{-1/3} \ll 1$. The gas moves with ballistic trajectories in the influence of the tidal sphere because the gravitational forces of the black hole are dominant over all the forces and so the orbital energy of the debris is *frozen-in* (Guillochon and Ramirez-Ruiz 2013) in the R_T with no dependency of the penetration parameter b. Stars approach the vicinity of the tidal sphere with highly eccentric orbits with $1 - e \approx R_{inf}/R_T = 10^{-6}$, being described by a parabola where the orbital energy is ≈ 0. This energy is symetrically spreaded over the debris being imparted into two categories: (1) stellar matter that has an energy increase gets unbound from the black hole with orbital energy $\Delta\varepsilon$ and (2) stellar matter that loses orbital energy $-\Delta\varepsilon$ (Rees 1988).

The matter that falls back has a mass rate that is specified by the energy distribution within the debris. The stream falls back to it in $\sim 1/2$ while the other $\sim 1/2$ escapes the black hole's gravitational pull. When the penetration parameter is $b \sim 1$, the star just grazes the tidal sphere and such encounters are more likely to occur for such values, especially in the empty loss cone regime. In such conditions disruption is partial and the self gravitating core of the star survives the pericentre passage (Guillochon and Ramirez-Ruiz 2013; Mainetti et al. 2017). Moreover mass loss is asymmetric due to the fact that more stellar matter is lost from the side facing the black hole, since the gas on this side is more bound to it and the partial disruption results in the increase of velocity to the surviving core (like the escape velocity of the star).

The star, describing a ballistic trajectory inside the tidal sphere gradually suffers compression from two orbital planes that intersect at pericentre and causes on the star a change in its shape, turning it into a flat *pancake* shape (Figure 2.3).

2.4 The fallback phase

After the disruption of a star by the black hole the splitting of the stellar matter can occur on two distinct portions of matter. About one half of the matter becomes bound to the SMBH describing elliptical trajectories where R_P is similar to the star's initial R_P. The other half of the stellar matter acquires orbital energy during the disruption process and will describe hyperbolic trajectories (Guillochon et al. 2014b). The bound material will return to the initial disruption point and the mass rate of the fallback debris can be evaluated in terms of the stellar matter. As this rate decreases with time $\sim$ t$^{-5/3}$ and the stream follows ballistic trajectories around the black hole, the most bound material will have a fallback time t_{fb} given by Kepler's third law for the most bound debris of (Hayasaki et al. 2016; Lodato et al. 2015),

$$\begin{aligned} t_{fb} &= \frac{\pi}{\sqrt{2}} \left(\frac{R_T}{R_*}\right)^{3/2} \sqrt{\frac{R_T^3}{GM_{BH}}} \\ &= 3.538 \times 10^6 \left(\frac{M_{BH}}{M_*}\right)^{1/2} \left(\frac{M_*}{M_\odot}\right)^{-1} \left(\frac{R_*}{R_\odot}\right)^{3/2} s, \end{aligned} \tag{2.24}$$

which for the same parameters from the example given above gives a fallback time of the most bound debris of $t_{fb} \approx 41$ days. For the Milky Way case the fallback time will be $t_{fb} \approx 82$ days. The debris reaches the black hole with a rate of the fallback mass of $\dot{M} = dM/dt$ and the spread in energy can be traced to a return time to R_P for the bound debris to the black hole by (Kocsis and Loeb 2014)

$$\dot{M}_{fb} = \frac{dM}{dt} = \frac{dM}{d\varepsilon}\frac{d\varepsilon}{dt} = \frac{(2\pi GM_{BH})^{2/3}}{3}\left(\frac{dM}{d\varepsilon}\right) t^{-5/3}. \tag{2.25}$$

The peak of the fallback mass rate ($\dot{M}_P$) is achieved when the mass of a star is $M_*/2$ and reaches the black hole by a time $t \geq P_{orb}$ if the fallback rate decay is $\dot{M} \propto t^{-5/3}$ (Rees 1988; Phinney 1989) and so the fallback rate can be written as (Evans and Kochanek 1989)

$$\begin{aligned} \dot{M}_{fb} &= \frac{M_*}{3t_{fb}} \left(\frac{t}{t_{fb}}\right)^{-5/3} \\ &= 3M_\odot \left(\frac{M_{BH}}{10^6 M_\odot}\right)^{-1/2} \left(\frac{R_*}{R_\odot}\right)^{3/2} \left(\frac{M_*}{M_\odot}\right)^{2} yr^{-1}. \end{aligned} \tag{2.26}$$

The debris stream that stays bound to the black hole (i.e. about half of the portion of the disrupted star that can return to the disruption point) can generate luminous flares. The debris that falls back to the black hole suffers vertical and horizontal compression which, in turn, can generate a shock that can heat the gas and dissipate thermal and kinetic energy (Rees 1988; Evans and Kochanek 1989). Furthermore, the debris that crosses the pericenter for the second time will suffer an orbital rotation through general relativistic precession angle which can reach $\sim 10^{\circ}$ for a solar type star being disrupted by a $10^6 M_{\odot}$ black hole, also assuming that the star's $R_P \approx R_T$ at the time of disruption (Rees 1988).

Receding from the black hole for a second time, the debris will impact the portion of debris that is still crossing its way to the black hole and this self intersection of the debris will deplete its kinetic energy by heating it viscously (Piran et al. 2015a). By means of such interactions the bound debris from a TDE is assumed to dissipate its ordered kinetic energy, which consequently results in the material moving close to the black hole. As the gas continues to lose energy efficiently, the debris can be funneled onto the black hole while a large amount of radiation is released during this process. Through this sequence of events the bound debris can produce intense accretion onto the black hole, during a certain period of time, which continues as portions of the debris stream returns to the pericenter of the original star, developing the conditions to form an accretion disc around the black hole.

If the SMBH mass is $\leq 10^7 M_{\odot}$ and assuming that the rate at which the material returns to pericentre is nearly the accretion rate onto the black hole, then this accretion will be *super-Eddington*[2] for months to years (Strubbe and Quataert 2009). This phase is characterized by isotropic radiation that in association with the accretion luminosity will exceed the gravitational pull of the black hole and so, the material can be blown off in a large scale wind (Strubbe and Quataert 2009), producing a spread on the disc to account for the high luminous output and redistribution of angular momentum (Shen and Matzner 2014), or the material can be heated till the point where the accretion disc becomes *quasi-spherical* (Loeb and Ulmer 1997).

2.5 Accretion disc formation

Stars that are tidally disrupted in realistic galactic nuclei are inbound to the SMBH on nearly zero energy orbits with their apocenters lying to parsec scales (Magorrian and Tremaine 1999; Wang and Merritt 2004). It is possible then to establish the relevance of the specific energies as $\varepsilon_{orb} \ll \Delta\varepsilon$ where ε_{orb} is the orbital specific energy and $\varepsilon_* = GM_*/R_*$ represents the star's approximate specific binding energy before disruption and as $\varepsilon_{orb} \ll \Delta\varepsilon$, $\Delta\varepsilon$ sets the fallback timescale for the most bound debris as in (2.24). After a few fallback times, the energy dissipation through shocks will circularize the tidal debris that falls back into an accretion disk that can induce gas transport to the SMBH through viscous processes.

The viscous timescale of the disk, at a certain radius R, given by (Shakura and Sunyaev 1973)

$$t_{visc} = \alpha^{-1}\Omega^{-1}(R)\left(\frac{H}{R}\right)^{-2}, \tag{2.27}$$

must be shorter than the mass fallback timescale and the time since disruption, where $\alpha < 1$ represents the dimensionless viscosity parameter , $H(R)$ is the disk scale height and $\Omega(R)$ represents the orbital frequency.

The debris that returns to the disk will be quickly accreted onto the SMBH in an approximate steady-state accretion flow. This accretion flow can be represented by the fallback rate $\dot{M} = (dM/d\varepsilon)(d\varepsilon/dt)$ from (2.25). In the case of keplerian orbits, the orbital energy derivative with respect to the orbital period P_* is $d\varepsilon/dt \propto t^{-5/3}$ (Phinney 1989). Assuming late times, where the distribution of stellar debris mass $dM/d\varepsilon$ is approximately flat with orbital specific energy and the fallback mass will be $\dot{M}_{fb}$ from (2.26). With such a fallback mass rate, this equation can be taken by evidence that the luminosity of a TDE flare

---

[2] The Eddington limit is considered the maximum luminosity for a star to avoid the radiative acceleration at its surface to exceed gravity (Eddington 1926; Langer et al. 2015)

can decrease as $t^{-5/3}$, considering a *bolometric luminosity*[3] (Lodato and Rossi 2011). The quickly accreted debris can relate the accretion rate of the mass in the disk to the fallback rate from (2.26). If the rest mass energy has a fraction η that can be radiated efficiently with $0 < \eta < 1$, its luminosity can be greater than the Eddington luminosity by (Langer et al. 2015)

$$\frac{\dot{M}_{fb}}{\dot{M}_{Edd}} = 1.38 \times 10^2 \left(\frac{\eta}{0.1}\right) \left(\frac{M_{BH}}{10^6 M_\odot}\right)^{-3/2} \left(\frac{t}{P_*}\right)^{-5/3}, \tag{2.28}$$

with the Eddington accretion rate given by $\dot{M}_{Edd} = 1.37 \times 10^{21}$ kg s^{-1} (Piran et al. 2015a). Through time the accretion luminosity decays as $L_{acc} = \eta \dot{M}_{fb} c^2 \propto t^{-5/3}$, having a peak luminosity near that of the Eddington luminosity given by (Piran et al. 2015a)

$$L_{acc} \approx L_{Edd} = 10^{44}\, erg\ s^{-1} \left(\frac{M_{BH}}{10^6 M_\odot}\right) \tag{2.29}$$

with the accompanying effective temperature of (Ulmer 1999)

$$T_{acc} = \left(\frac{L_{acc}}{4\pi R_{ph}^2 \sigma_{SB}}\right)^{1/4} = 2 \times 10^5 \left(\frac{R_{ph}}{R_P}\right)^{-1/2} \left(\frac{M_{BH}}{10^6 M_\odot}\right)^{1/4} K \tag{2.30}$$

where the Stefan-Boltzman constant is represented by σ_{SB}, with a photospheric radius of $R_{ph} \approx R_P$, wich corresponds to the torus dimensions (Rees 1988; Ulmer 1999; Lodato and Rossi 2011; Miller 2015).

A star crossing the R_T should conserve its orbital angular momentum before and after the disruption moment, if no mechanism can redistribute it. The dissipation of orbital energy will then circularize the stellar debris that is orbiting, due to shocks from orbit crossing that conserve the orbital angular momentum before and after, the stream debris semi-major axis will approach the circularization radius of the initial stellar orbit. To achieve an accretion disc one of the most important factors regards the efficiency of the dissipation mechanism. To dissipate the circularization energy $\Delta\varepsilon = GM_{BH}/(4R_P)$ in a dynamical timescale, a rapid circularization of the stream has to occur. Two main dissipation mechanisms have to be taken into account:

(1) The strong compression of the debris stream at pericentre, since this stream is less dense then the star its tidal radius will be further away. As a consequence, there will be strong vertical compression as the stream intersects its own tidal radius (Figure 2.4) Due to the shock produced during this intersection the energy dissipation of the stream is about the same of that experienced by the star and (Guillochon et al. 2014b)

$$\Delta\varepsilon_{no} = v_c^2 \approx b^2 \frac{GM_*}{R_*} \tag{2.31}$$

is the dissipated energy, with v_c given by (4.10). For a black hole of $\sim 10^6 M_\odot$ and $b = 1$ then $\Delta\varepsilon_{no}/\Delta_{circ} \approx b\,(M_{BH}/M_*)^{-2/3} \sim 10^{-4}$ and so a complete circularization of the debris cannot be driven by this dissipation mechanism.

(2) Self-intersection of the stream debris (Figure 2.4) can be an effective dissipation mechanism as this intersection occurs when the most bound stream crosses at pericentre and its orbit precesses due to relativistic precession impacting the portion of the stream that describes a later approach to the black hole. The collision of these two portions of the stream produce shocks that can dissipate a significant amount of the orbital energy of the stream debris into heat. The dissipation of the energy

---

[3] The energy emitted across the whole electromagnetic spectrum.

due to shocks by self-intersection can be obtained by

$$\Delta\varepsilon_{si} = \frac{\nu_{si}^2}{2} sin^2(\psi/2) \approx \frac{GM_{BH}}{R_{int}} \tag{2.32}$$

where $\nu_{si} \approx (GM_{BH}/R_{int})$ is the velocity at the shock point, R_{int} is the intersection radius and the angle formed by the incoming and outgoing stream is ψ, which in fact corresponds to the angle between the velocity vectors of the two portions of the stream (Dai et al. 2015; Bonnerot et al. 2017a).

As the two portions of the stream are crossing in opposite directions it means that $sin(\psi/2) \approx 1$. The intersection radius R_{int} should be near the semi-major axis of the bound debris, as $R_{int} \approx a_{min}$. For low values of ϕ, $\Delta\epsilon_{si}/\Delta\epsilon_{circ} \approx R_P/a_{min} \approx 10^{-2}$ (for the standard $M_{BH} = 10^6 M_\odot$; b = 1), which means that self-intersection shocks cannot also circularize completely the debris. The stream debris can achieve a complete circularization when the intersection radius decreases to $R_{int} \approx R_P$. For $M_{BH} \geq 10^7$ or a penetration parameter $b \geq 5$ the precession angle is expected to increase and so reducing the intersection radius for $R_{int} \approx R_P$. The above analysis allows the conclusion that self-intersection shocks represent a more efficient mechanism for energy dissipation in presence of black holes whose masses are of a few $M_{BH} \approx 10^6 M_\odot$, though none of the above mechanisms are effective enough to achieve a complete circularization of the stream debris, which will be possible only after several passages around the BH (Guillochon et al. 2014b) .

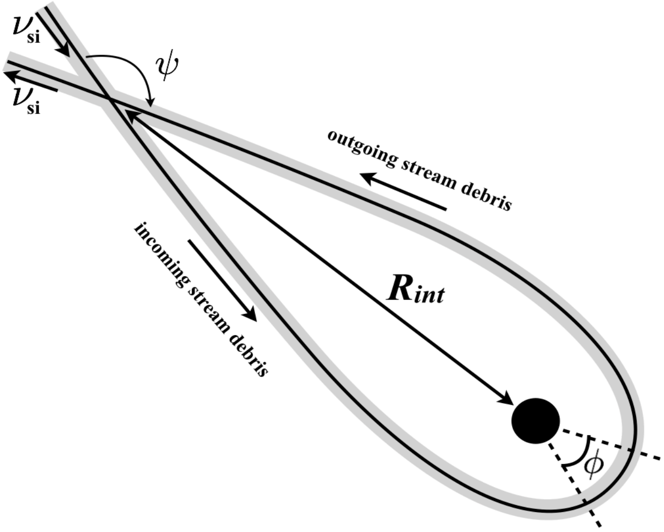

Figure 2.4: The self-intersection of the most bound debris is precessed by an angle ϕ after passing R_P. The outgoing debris intersects the portion of the debris still approaching the black hole (Coughlin 2016).

Another phenomena that affects the accretion disc formation is related to radiative cooling. If radiative cooling is inefficient than the accretion disc will not settle and the heat injected in the gas by the shocks (due to self-intersection) will not be radiated away efficiently. The diffusion time of the gas stream $t_{dif} = H\tau/c$ with the stream width given by H and $\tau = k_T \rho H$ is the optical depth (for $k_T = 0.4$ cm^2 g^{-1} which is the opacity for Thomson scattering). A stream element has density $\rho \approx \dot{M}_P/(\pi H^2 \nu_{sh})$ (by mass conservation) where the velocity of the stream is given by $\nu_{sh} \approx R_P/t_{dyn}$, which sets the heat injection region with a length of $\sim R_P$. The ratio between diffusion and the dynamical timescale is (Metzger and Stone 2016)

$$\frac{t_{dif}}{t_{dyn}} \approx \frac{\dot{M}\rho k_T}{\pi R_P c} \tag{2.33}$$

giving a slow cooling of the gas that suffers expansion in its distribution at near constant total energy. The energy $f\Delta\varepsilon_{circ}$ dissipated to circularize a portion f of the imparted gas the initial energy $\Delta\varepsilon$ of the debris yelds $f = \Delta\varepsilon/\Delta\varepsilon_{circ} \approx b\,(M_{BH}/M_*)^{-1/3} \approx 10^{-2}$, therefore about 1% of the circularized debris can dissipate enough energy that consequently will unbind the remaining debris (Bonnerot et al. 2017b).

Studies carried out on the process of accretion disc formation confirm that self-intersection of the stream debris is generally the most efficient mechanism of dissipation of energy. The hydrodynamical simulations, achieved so far, for the disc formation process have been made for the simplified cases where the stream length is artificially reduced, because the elongated geometry of the stream debris (for the standard $M_{BH} = 10^6 M_\odot$ and b = 1) represent a large computational cost (Ayal et al. 2000). In order to avoid such a constraint these simulations have been made for black hole masses of $M_{BH} = 10^3 M_\odot$ (Ramirez-Ruiz and Rosswog 2009; Rosswog et al. 2009; Guillochon et al. 2014b; Shiokawa et al. 2015) or the injection of the star have been made to a bound orbit, instead of a parabolic one (Bonnerot et al. 2016; Hayasaki et al. 2016).

The accretion disc formation process have been targeted with proposals for different sources of emission in an atempt to explain the possible origin for the low energy optical /UV emission that has been detected in certain TDEs. Forward shocks are indicated as a major source of optical emission source (Lodato 2012; Piran et al. 2015b). One consequence for the dissipated energy by shocks to be approximate to that of (2.32) for self-intersection due to shocks, comes from the fact that most of the gas resides at distances of $\sim a_{min}$, after disc formation, with $R_{int} \approx a_{min}$. For such case the peak luminosity can be obtained by (Piran et al. 2015a)

$$L_{sh} = \dot{M}_P \Delta\varepsilon_{si} \approx 7 \times 10^{43}\, erg\ s^{-1} \left(\frac{M_{BH}}{10^6 M_\odot}\right)^{-1/6} \tag{2.34}$$

with an associated temperature of (Piran et al. 2015b)

$$T_{sh} = \left(\frac{L_{sh}}{4\pi R_{ph}^2 \sigma_{SB}}\right)^{1/4} = 3 \times 10^4 \left(\frac{M_{BH}}{10^6 M_\odot}\right)^{-3/8} K \tag{2.35}$$

and the radiation is assumed to surface from a photosphere based at a distance of $R_{ph} \approx a_{min}$ from the BH, such temperature is consistent with the temperature found on optical TDEs. The luminosity that results from these shocks (when the recent fallback debris encounters the new disc) is thought to scale as $\dot{M}_{fb} \propto t^{-5/3}$ (as observed). During this process the emission of X-rays may not occur due to magnetic stresses developed on the gas located at the accretion disc, which can drive it to the event horizon and inhibitting any accretion luminosity (Svirski et al. 2017), though none X-ray emission is expected to occur as the gas gets closer to the gravitational radius (R_G; Bonnerot et al. (2017b)). The resulting debris from TDEs form a disc of gas that spreads radially in a continuous mode due to angular momentum redistribution (Pringle 1981) induced by viscosity. During the accretion onto the SMBH, the outer radius (R_{out}) keeps growing and its viscous timescale will be near the current time $\approx R_{out}^2/v \approx t$. This implies an increasing R_{out} as $R_{out} \propto t^{2/3}$ and viscosity scales with distance as $v \propto R^{1/2}$, considering a thick disc where $H \approx R$ and $c_s \approx \nu_k$, so hydrostatic equilibrium is imposed in the vertical direction[4].

The model proposed by Rees (1988) was able to resolve the initial TDEs class detected in the soft

---

[4] In the vertical direction $\nu_k \propto R^{-1/2}$ is the keplerian circular velocity and viscosity evolves with radius $\nu \propto R^{1/2}$.

X-rays with luminosities of $\sim 10^{44}$ erg s^{-1} and $t^{-5/3}$ until a few years ago. As recent optical TDEs have been detected with lower effective temperatures of $\sim 10^4\ K$, this model can no longer account for this more recent class of TDEs, as new understanding of this phenomena dynamics arise, new proposals of emission sources gain visibility attempting to explain such observations.

2.6 Summary

The theoretical developments on TDEs over the last years allowed to establish the basis for the work presented in Chapter 4.

The influence of the galactic SMBH over the surrounding stars constrains the stellar distribution and respective stellar orbits on the GC and can determine the fate of stars that fall on the sphere of influence of the black hole. When a star suffers such influence it enters on fatal trajectories inbound onto the compact object where it no longer escape from and such dynamic process is known as the loss cone.

During its approach to the SMBH the star suffers the influence of tidal forces (from the black hole) that are exerted over the star producing its deformation and disruption. Such effects are determined by the deepness of the plunge that the star takes during its fatal fall onto the compact object which is a function of the penetration parameter (b). This phase is known as the pancake phase.

After the TDE the material that is ripped off from the stellar surface can evolve dynamically forming two tidal tails where one tail represents the portion of the stellar debris that stays bound to the black hole and the other portion of the stellar debris will be forcefully ejected on hyperbolic trajectories.

The bound debris will be accreted on a fallback phase that is determined by the fallback rate decay $\dot{M} \propto t^{-5/3}$ to the debris that settles in a steady rate of accretion. The stellar debris that circularizes around the black hole can eventually form an accretion disc, which is determined by the mechanism that can efficiently dissipate the energy of the orbiting stellar debris.

3

Smoothed Particle Hydrodynamics

3.1 Introduction

The two main approaches to computational simulations of fluids are based on Eulerian and Lagrangian methods. The first method fixes the observer and the fluid moves relatively to him in geometric grids that can be fixed or adaptive (e.g., AMR - Adaptive Mesh Refinement) where the fluid parameters are evaluated over grid cells. The second method deals with the fluid equations where the observer moves with the flow. A good example of such method is the SPH (Lucy 1977) and Gingold and Monaghan (1977) where discrete particles are carried in the flow and the hydrodynamic properties are evaluated at particle positions and calculated from weighted average values on other particles. In this way the particles are smoothed over a volume of fixed mass, which turns this method implicitly adaptive in terms of the density (Price 2012a). While Eulerian codes can be adapted to flow parameters, these present higher resolution in a certain number of grid cells than an SPH code for the same number of particles, which is essentially density adaptive (Monaghan 1997). On the other hand SPH codes deal better with vacuum boundary conditions while Eulerian codes need large grids so the flow escape from the limits of the computational domain can be prevented (Monaghan 2005). The advection of flow properties is implicit in the Lagrangian method of SPH in such a way that mass, momentum and energy are inherently conserved, as well as for entropy, unless it is explicitly added in shocks (Cossins 2010).

3.2 Fluid equations

The basic idea of the SPH is to replace the equations of fluid dynamics by equations of particles. The SPH formalism will be used to approximate the continuous field onto a set of equations for particles that can be smoothed to represent the field through its derivatives, with the errors that such approximations involves. The simplest set of the Euler equations for an ideal gas are the equations of motion in the conservative form, which are the equations for the conservation of mass, momentum and energy. The equation for the conservation of mass is given by (Cossins 2010)

$$\frac{\partial \rho}{\partial t} + \nabla \cdot (\rho \mathbf{v}) = 0 \tag{3.1}$$

where ρ is the density, t is the time and $\mathbf{v}$ is the velocity. Considering the case of an inviscid fluid[1], the Euler equation gives the equation of motion, where the conservation of momentum is implied and in the absence of external forces the momentum equation can be written as (Cossins 2010)

$$\frac{\partial \rho \mathbf{v}}{\partial t} + \nabla \cdot (\rho \mathbf{v} \otimes \mathbf{v}) + \nabla P = 0 \tag{3.2}$$

with P denoting the fluid pressure and $\otimes$ is the tensor product[2]. The energy equation embodies the conservation of energy in the equation (Cossins 2010)

$$\frac{\partial u}{\partial t} + \nabla \cdot [(u + P)\mathbf{v}] = 0 \tag{3.3}$$

where u represents the specific internal energy and $v = |\mathbf{v}|$ is the velocity vector. As the above equations have five unknowns, i.e., v_x, v_y and v_z which are the components of the velocity, P and u, in order to close the system an equation of state is needed, in fact it is the equation of state for an ideal gas, which is (Cossins 2010; Price 2005)

$$P = (\gamma - 1)u\rho \tag{3.4}$$

where $\gamma = 5/3$ is the adiabatic index. Henceforth it will be considered that the mass of the particles is constant ($m_i = const.$) and that all the particles have equal mass. The following approximations will be related to specific particle positions.

3.2.1 Conservation of mass

The SPH approximation for the density ρ_j of particle j is (Cossins 2010)

$$\rho_j = \sum_i m_i W(\mathbf{r}_j - \mathbf{r}_i, h) \tag{3.5}$$

$$= \sum_i m_i W_{ji} \tag{3.6}$$

with $W_{ji} = (\mathbf{r}_j - \mathbf{r}_i, h)$. The time derivative for the density is

$$\frac{d\rho_j}{dt} = \sum_i m_i (\mathbf{v}_j \cdot \nabla_j W_{ji} + \mathbf{v}_i \cdot \nabla_i W_{ji}) \tag{3.7}$$

$$= \sum_i m_i \mathbf{v}_{ji} \cdot \nabla_j W_{ji} \tag{3.8}$$

---

[1] A fluid for which all surface forces applied on the boundaries of each element of the fluid act normal to those boundaries.

[2] $A \otimes B = AB^T = A_i B_j$

noting that the gradient of the kernel is antisymmetric with

$$\nabla_i W_{ji} = -\nabla_j W_{ji} \tag{3.9}$$

and $\mathbf{v}_{ji} = \mathbf{v}_j - \mathbf{v}_i$. As in (3.8) the right hand side represents an estimator of $-\rho_j \nabla_j \cdot \mathbf{v}_j$, then this equation can be written as

$$\frac{d\rho_j}{dt} = -\rho_j \nabla_j \cdot \mathbf{v}_j \tag{3.10}$$

where it can be noted that is a different form to write the equation of continuity from (3.1), with the Lagrangian time derivative being

$$\frac{d}{dt} = \frac{\partial}{\partial t} + (\mathbf{v} \cdot \nabla) \tag{3.11}$$

where the advection of flow properties is taken in the 2^{nd} term. In (3.6) the SPH approximation for the density is taken as conservative of mass (Cossins 2010).

3.2.2 Conservation of momentum

The equation of motion can be written in the SPH formalism in a particular form using the Lagrangian formalism. If the discrete Lagrangian functional holds for the fundamental symmetries of the continuous one, the SPH equations of motion will inherently oblige the conservation laws.

The Lagrangian functional $\mathcal{L}$, for the case of hydrodynamical flows, can be defined as the difference between the total kinetic energy and the total internal energy and is (Cossins 2010)

$$\mathcal{L}(\mathbf{r}, \mathbf{v}) = \int_V \left(\frac{1}{2} \rho \mathbf{v} \cdot \mathbf{v} - \rho u \right) d\mathbf{r} \tag{3.12}$$

where the specific internal energy is defined by u. As the specific internal energy is a function of density and pressure $(u = (\rho, P))$, these in turn are a function of position $(u = u(\mathbf{r}))$. If i is related to all particles then the approximation for the Lagrangian is (Cossins 2010)

$$\mathcal{L}(\mathbf{r}, \mathbf{v}) = \sum_i m_i \left(\frac{1}{2} \mathbf{v}_i \cdot \mathbf{v}_i - u_i(\mathbf{r}_i) \right) \tag{3.13}$$

with the specific internal energy defined by u. After some adequate substitutions (which are beyond of the scope of this work) the SPH equations of motion for the linear momentum are then (Cossins 2010)

$$\frac{d\mathbf{v}_j}{dt} = -\sum_i m_i \left(\frac{P_j}{\rho_j^2} + \frac{P_i}{\rho_i^2} \right) \nabla_j W_{ji}. \tag{3.14}$$

The conservation of angular momentum $L = \mathbf{r} \times m\mathbf{v}$ is taken by its derivative in order of time equals to zero. The total time derivative for the angular momentum for all particles j through (Cossins 2010)

$$\begin{aligned}\frac{dL}{dt} &= -\sum_j \sum_i m_j m_i \left(\frac{P_j}{\rho_j^2} + \frac{P_i}{\rho_i^2} \right) \mathbf{r}_j \times \nabla_i W_{ij} &(3.15)\\ &= \sum_i \sum_j m_i m_j \left(\frac{P_i}{\rho_i^2} + \frac{P_j}{\rho_j^2} \right) \mathbf{r}_i \times \nabla_j W_{ji}. &(3.16)\end{aligned}$$

Antisymmetry can be observed in the above equations related to j and i as long as the sum is equal to zero. The angular momentum is conserved as it is constant through time (Monaghan 1992; Cossins 2010; Price 2005).

3.2.3 Conservation of energy

Considering the total energy for a fluid

$$E = \rho u + \frac{\rho v^2}{2}. \tag{3.17}$$

which is the sum of the kinetic energy and internal energy, the SPH approximation is given by

$$E = \sum_i m_i \left(\frac{1}{2} \mathbf{v}_i \cdot \mathbf{v}_i + u_i \right). \tag{3.18}$$

If the time derivative of the total energy is zero it implies that the energy is conserved, taking the time derivative it becomes

$$\frac{dE}{dt} = \sum_i m_i \left(\mathbf{v}_i \cdot \frac{d\mathbf{v}_i}{dt} + \frac{P_i}{\rho_i^2} \frac{d\rho_i}{dt} \right) \tag{3.19}$$

and $P = P(\rho)$. From (3.8) and taking $d\rho/dt$ from (3.14) the time derivative for the energy equation is

$$\frac{dE}{dt} = \sum_i \sum_j m_i m_j \left(\frac{P_j}{\rho_j^2} \mathbf{v}_i + \frac{P_i}{\rho_i^2} \mathbf{v}_j \right) \cdot \nabla_j W_{ji}. \tag{3.20}$$

Noting that if the same strategy is used as for the angular momentum, then is possible to observe that the above equation is antisymmetric of j and i which should equal to zero. Then

$$\frac{dE}{dt} = 0 \tag{3.21}$$

and that the total energy is explicitly conserved. Finally, the SPH approximation for the internal energy is given by (Price 2005; Cossins 2010)

$$\frac{du_j}{dt} = \frac{P_j}{\rho_j^2} \sum_i m_i (\mathbf{v}_j - \mathbf{v}_i) \cdot \nabla_i W_{ji}. \tag{3.22}$$

3.3 Integral interpolant and approximation to a continuous field

Assuming that the following expression

$$f(r) = \int_V f(\mathbf{r}')\delta(\mathbf{r} - \mathbf{r}')dr' \tag{3.23}$$

represents an identity where $f(\mathbf{r})$ is a scalar function on a three dimensional coordinate system **r** over the volume **V** and the Dirac delta function $\delta(\mathbf{r})$[3] which is a function with **r'** being a variable ranging over **r**. The function $\delta(\mathbf{r})$ can be generalized to a smoothing kernel W with a smoothing length h, such

$$\lim_{h \to 0} W(\mathbf{r}, h) = \delta(\mathbf{r}) \tag{3.24}$$

with the normalization condition

$$\int_V W(\mathbf{r}, h) d\mathbf{r}' = 1. \tag{3.25}$$

---

[3] Dirac delta function is generally used to normalize wave functions which cannot be normalized to unity (Belloni and Robinett 2014).

If $W(\mathbf{r}-\mathbf{r}', h)$ can be expressed by a Taylor series, then for symmetric kernels $W(\mathbf{r}-\mathbf{r})' = W(\mathbf{r}´ - \mathbf{r})$ (3.23) can be written as (Cossins 2010)

$$f(\mathbf{r}) = \int_V f(\mathbf{r}')W(\mathbf{r}-\mathbf{r}', h)d\mathbf{r}' + \mathcal{O}(h^2) \tag{3.26}$$

where the 2^{nd} order accuracy rises from the disappearance of the kernel gradient $\mathbf{r}' = \mathbf{r}$ (Price 2005; Monaghan 1992). For a symmetric kernel of density $\rho(\mathbf{r})$ over a volume V, (3.26) can be written as

$$f(\mathbf{r}) = \int_V \frac{f(\mathbf{r}')}{\rho(\mathbf{r}')} W(\mathbf{r}-\mathbf{r}', h)\rho(\mathbf{r}')d\mathbf{r}' + \mathcal{O}(h^2), \tag{3.27}$$

which can be discretized to a series of particles of mass $m = \rho(\mathbf{r}')d\mathbf{r}'$. Thus (3.23) becomes

$$f(\mathbf{r}) \approx \sum_i \frac{m_i}{\rho_i} f(\mathbf{r}_i)W(\mathbf{r}-\mathbf{r}_i, h) \tag{3.28}$$

with the ith particle of mass m_i and density ρ_i having the scalar value of $f(\mathbf{r}_i)$ and i spreads over all the particles in the range of the smoothing kernel. Equation (3.28) represents the basis of all SPH formalism (Price 2005), in fact, a discrete approximation to a continuous field f at a position $\mathbf{r}$ in the computational domain V.

3.3.1 Derivatives

As a method of fluids flow solver, the SPH method has to account for a convenient approximation for the derivatives (of any quantity), which are presented as follows. Applying the smoothing kernel by taking the spatial derivative of (3.23), with $\nabla \equiv \partial/\partial\mathbf{r}$, then

$$\nabla f(\mathbf{r}) = \frac{\partial}{\partial_{\mathbf{r}}} \int_V f(\mathbf{r}')\delta(f-\mathbf{r}')d\mathbf{r}' \tag{3.29}$$

$$= \frac{\partial}{\partial\mathbf{r}} \int_V f(\mathbf{r}')W(\mathbf{r}-\mathbf{r}', h)d\mathbf{r}' + \mathcal{O}(h^2). \tag{3.30}$$

As the smoothing length W depends on $\mathbf{r}$ the density can be introduced in the equation to give

$$\nabla f(\mathbf{r}) = \int_V \frac{f(\mathbf{r}')}{\rho(\mathbf{r}')} \frac{\partial}{\partial\mathbf{r}} W(\mathbf{r}-\mathbf{r}', h)\rho(\mathbf{r}')d\mathbf{r}' + \mathcal{O}(h^2), \tag{3.31}$$

whose discretization is

$$\nabla f(\mathbf{r}) \approx \sum_i \frac{m_i}{\rho_i} f(\mathbf{r}_i)\nabla W(\mathbf{r}-\mathbf{r}', h), \tag{3.32}$$

which represents the approximation of the gradient of a field $f(\mathbf{r})$ (Price 2005; Monaghan 1992). Giving (3.23) an equivalent form for a vector field $F(\vec{r})$, then

$$F(\mathbf{r}) = \int_V F(\mathbf{r}')\delta(\mathbf{r}-\mathbf{r}')d\mathbf{r}'. \tag{3.33}$$

Once again, only the smoothing kernel W depends on $\mathbf{r}$, the divergence in terms of $\mathbf{r}$ is

$$\nabla \cdot f(\mathbf{r}) = \int_V F(\mathbf{r}') \cdot \nabla W(\mathbf{r}-\mathbf{r}', h)d\mathbf{r}' + \mathcal{O}(h^2), \tag{3.34}$$

which after discretization becomes (Price 2005)

$$\nabla \cdot F(\mathbf{r}) \approx \nabla W(\mathbf{r} - \mathbf{r}', h) d\mathbf{r}' + \mathcal{O}(h^2). \tag{3.35}$$

Finally, using the same arguments as before, the curl of the vector ($\nabla \times F$) can be expressed (Price 2005) by

$$\nabla \times F(\mathbf{r}) \approx \sum_i \frac{m_i}{\rho_i} F(\mathbf{r}_i) \times \nabla W(\mathbf{r} - \mathbf{r}_i, h) \tag{3.36}$$

which is the approximation to the continuous field, though in this case its use is essentally to account for MHD effects.

3.4 Errors

The errors that occur from considering only the integral term and those committed in the discretizations are encompassed from the approximations in (3.28), (3.32), (3.35) and (3.36). In the first case the $\mathcal{O}(h^2)$ errors can be decreased if the smoothing kernel is reduced and in the second case the discretization errors can be can be reduced if the number of particles increase within the smoothing kernel.

The errors are described in terms of the approximations of the function $f(\mathbf{r}) \equiv 1$ and zero function, where the definition of f implies $\nabla f(\mathbf{r}) = 0$. Then, the one and zero SPH approximations are Price (2005)

$$1 \approx \sum_i \frac{m_i}{\rho_i} W(\mathbf{r} - \mathbf{r}', h), \;\; 0 \approx \sum_i \frac{m_i}{\rho_i} \nabla W(\mathbf{r} - \mathbf{r}', h). \tag{3.37}$$

These errors can be maintained in an acceptable level, if a suited choice for the number of particles over the smoothing kernel and the smoothing length is done.

The choice of an adequate kernel must be done from the criteria set from (3.24) and (3.25) such that the kernel must tend to a δ function when $h \to 0$ and it also has to be normalized so that the area under the curve is of order unity. The kernel must have the first derivative well defined to calculate the gradient and has to be spherically symmetric, so this way it only have to depend on $r = |\mathbf{r} - \mathbf{r}'|$ and h. The Gaussian function defined by

$$W(r, h) = \frac{1}{k^3 \pi^{3/2}} e^{-x^2} \tag{3.38}$$

was one of the first choices for the smoothing kernel, where $x = r/h$. This kernel presents a disadvantage, because all particles in the computational domain contribute, due to $W > 0$ for all r. The use of this kernel makes the computational cost to scale up to $\mathcal{O}^2$ with N being the particles present in the simulation. For this reason and since long range forces are negligible, the kernel should be constrained to the one with compact support, that is to say that it must be under the condition $W(r, h) = 0$, with $r/h > k$ (where k is a constant).

This condition scales the computational cost to $\mathcal{O}(N N_{neigh})$ with N_{neigh} being the average number of particles on a sphere of radius $r = kh$ (Price 2005). In order to avoid such computational cost the use of cubic splines is better suited (Monaghan and Lattanzio 1985) and the kernel based on this cubic splines is defined by

$$W(r, h) = \frac{1}{\pi h^3} \begin{cases} 1 - \frac{3}{2}x^2 + \frac{3}{4}x^3 & 0 \leq x \leq 1; \\ \frac{1}{4}(2 - x)^3 & 1 \leq x \leq 2; \\ 0 & x \geq 2 \end{cases} \tag{3.39}$$

and x is the same as in (3.38) (Monaghan 1992; Price 2005).

As most of the codes tabulate the values of the kernel and its gradient rather then compute them directly, the form of the kernel makes little difference for the speed of the computation of the code. In the present work the kernel used in Phantom is the M_4 cubic kernel.

3.5 Shocks

When transonic and supersonic flow regimes are to be modelled, the conversion of the mechanical (kinetic) energy into thermal (internal) energy can represent a challenge, as this conversion may not be correctly captured, i.e., for small scales, which in SPH corresponds to the smoothing length, the discontinuities are not well resolved by the numerical method. In order to solve this problem a small amount of viscosity is introduced in the simulations, spreading the shocks (shock fronts) in order to be well resolved or at least *sufficiently* resolved (Richtmyer and Dill 1959).

3.6 Artificial viscosity

The most used artificial viscosity form is derived from the momentum equation as (Monaghan 1992)

$$\frac{d\mathbf{v}_j}{dt} = -\sum_i m_i \left(\frac{P_i}{\rho_i^2} + \frac{P_j}{\rho_j^2} + \Pi_{ji} \right) \nabla_j W_{ji}, \tag{3.40}$$

with Π_{ji} given by

$$\Pi_{ji} = \begin{cases} \frac{-\alpha\bar{c}_{ji}\mu_{ji}+\beta\mu_{ji}^2}{\bar{\rho}_{ji}}, & \mathbf{v}_{ji}\cdot\mathbf{r}_{ji} < 0 \\ 0 \qquad , & \mathbf{v}_{ji}\cdot\mathbf{r}_{ji} > 0 \end{cases}, \tag{3.41}$$

where the term μ_{ji} is given by

$$\mu_{ji} = \frac{h\mathbf{v}_{ji}\cdot\mathbf{r}_{ji}}{\mathbf{r}_{ji}^2 + \eta^2}. \tag{3.42}$$

When $\mathbf{v}_{ji}\cdot\mathbf{r}_{ji} > 0$ the viscosity is swept away.

The artificial viscosity expression Π_{ji} has a linear term in the velocities that allows for shear and bulk viscosity to occur (Monaghan and Lattanzio 1985). High mach number shocks must be treated with the quadratic term which is the equivalent for the Von Neumann-Richtmeyer viscosity finite-difference methods, with some clear advantages such:

i) is Galilean invariant;

ii) for rigid body rotation problems it disappears;

iii) linear and angular momentum are conserved.

General astrophysical applications where shock fronts have a spreading of $\approx 3h$, can have good accuracy when $\alpha = 1$ and $\beta = 2$. The smoothing of the viscous term, which can be dramatic in dense regions, will be prevented with η^2 term, in μ_{ji}, preventing singularities to occur having $\eta^2 = 0.01h^2$ (Monaghan 1992; Price 2005).

3.7 Thermal conductivity

The approximation to the thermal conductivity term (Monaghan 1992)

$$\frac{1}{\rho}\nabla\cdot(k\nabla u) \tag{3.43}$$

where k is the coefficient of thermal conductivity and is based on the SPH integral form, such

$$-\sum_i m_i \frac{(q_j+q_i)(u_j-u_i)(\mathbf{r}_{ji}\cdot\nabla_j W_{ji})}{\bar{\rho}_{ji}(\mathbf{r}_{ji}+\eta^2)}, \tag{3.44}$$

with the term $q = k/\rho$ having the length × velocity dimension. In the conditions where the kernel is a Gaussian and the density is constant, then the particle i contributes to the heat conduction of particle j by

$$\frac{-2m_i k(u_j-u_i)W_{ji}}{\rho h^2}. \tag{3.45}$$

The exchange of heat between pairs of particles leads to the thermal conduction. The conduction term in SPH conserves total energy and with the increase of the thermal energy with temperature, the total entropy also increases, as expected (Monaghan and Lattanzio 1985; Monaghan 1992).

The thermal energy equation can include the diffuse radiation transport (if occurs). As the total energy is conserved with the transport no heat loss will occur, otherwise a surface term will be needed, that can be obtained by derivation of the physical arguments. Nevertheless, simulating radiation processes in astrophysical phenomena is still complex, though the thermal energy equation can add heating and cooling sources but it will have to be integrated implicitly due to the large differences between the short cooling time and the dynamical timescale (Monaghan 1992).

3.8 The magnetic field

The magnetic fields are obtained through the magnetic force and current. In SPH the current must be estimated accurately because is where the matter is present. The magnetic force per unit mass is given by (Monaghan 1992)

$$\frac{\mathbf{J}\times\mathbf{B}}{\rho} \tag{3.32}$$

with the current $\mathbf{J}$ given by

$$\mathbf{J} = \varepsilon c^2 \nabla\times\mathbf{B}. \tag{3.33}$$

The estimation for the current is

$$\rho\nabla\times\mathbf{B} = \nabla\times(\rho\mathbf{B}) - (\nabla\rho)\times\mathbf{B}, \tag{3.34}$$

where

$$\rho_j(\nabla\times\mathbf{B})_j = \sum_i m_i(\mathbf{B}_j-\mathbf{B}_i)\times\nabla_j W_{ji}, \tag{3.35}$$

which in the case of constant $\mathbf{B}$ it will be supressed (Gingold and Monaghan 1977). Assuming that the kernel is a Gaussian, particle i contributes for the current in particle j through (Monaghan 1992)

$$-\left(\frac{2\varepsilon_0 c^2 m_i W_{ji}}{h^2\rho_j}\right)(\mathbf{B}_j-\mathbf{B}_i)\times(\mathbf{r}_j-\mathbf{r}_i). \tag{3.36}$$

A consequence of (3.36) is that there is only information of the current on particle i on the direction $\perp$ to $(\mathbf{r}_j - \mathbf{r}_i)$. The time variation of the **B** assumes the form

$$\frac{d\mathbf{B}}{dt} = -\mathbf{B}(\nabla \cdot \mathbf{v}) + (\mathbf{B} + \nabla)\mathbf{v} \tag{3.37}$$

which has the SPH equivalent in the form

$$\frac{d\mathbf{B_{jj}}}{dt} = \frac{1}{\rho_j} \sum_i m_i(\mathbf{B}_{\mathbf{jj}}\mathbf{v}_{ji} - v_{ji,\mathbf{j}}\mathbf{B}_j) \cdot \nabla_j W_{ji} \tag{3.38}$$

and the term $v_{ji,\mathbf{j}}$ is the j^{th} component of $\mathbf{v}_{ji}$. The compression of the field lines by the first term increases **B** and the 2^{nd} term shears the j component of **B** (Gingold and Monaghan 1977).

3.9 The Phantom code

The Phantom code is based on the method of Smoothed Particle Hydrodynamics. Its a parallel and low memory code which was developed in 3D by Price et al. (2017), for astrophysical purposes, where stellar, galactic, planetary and high energy astrophysics have the main focus. A brief description of the code is presented downwards.

In the Phantom code the equations describing the compressible hydrodynamics are set through the equations of velocity, energy and the equation of state as (Price et al. 2017)

$$\frac{dv}{dp} = -\frac{\nabla P}{\rho} + \Pi_{shock} + a_{ext}(r,t) + a_{sink-gas} + a_{selfgrav}, \tag{3.46}$$

$$\frac{du}{dt} = -\frac{P}{\rho}(\nabla \cdot v) + \Lambda_{shock} - \Lambda_{cool}, \tag{3.47}$$

where P is the pressure, u represents the specific internal energy and the accelerations from external forces (body forces), self particles and self-gravity are represented by a_{ext}, $a_{sink-gas}$ and $a_{selfgrav}$. The entropy increase of the shocks is set by the dissipation terms Π_{shock} and Λ_{shock} and Λ_{cool} represents the cooling term. Assuming that shocks radiate away the heat that is generated at the shock front, the cooling term is set to zero ($\Lambda_{shock} = 0$) and there is no cooling ($\Lambda_{cool} = 0$). The equation of state closes the set of equations relating the pressure with the density and internal energy. This equation of state for an ideal gas is given from equation 3.4 with the adiabatic index being represented by γ and the sound speed (c_s) is (Price et al. 2017)

$$c_s = \sqrt{\frac{\gamma P}{\rho}}. \tag{3.48}$$

The pressure of the gas can be expressed also by

$$P = \frac{\rho k_B T}{\mu m_H}, \tag{3.49}$$

where m_H is the mass of an hidrogen atom and the internal energy u is related to the gas temperature by

$$T = \frac{\mu m_H}{k_B}(\gamma - 1)u. \tag{3.50}$$

nstantIn this expression k_B is the mean molecular weight μ and m_H is an hidrogen atom (atomic mass unit; *amu*). The default equation of state used in Phantom is $P = (1-\gamma)\rho\mu$ with $\gamma = 5/3$.

3.9.1 Timestepping

A generalized leapfrog integrator[4] is used for the equations of motion. The leapfrog method is the *velocity Verlet* from Verlet (1967). This method updates the positions and velocities of the particles from t^n to t^{n+1}, admitting

$$v^{n+1/2} = v^n + \frac{1}{2}\Delta t a^n, \tag{3.51}$$

$$r^{n+1} = r^n + \Delta t v^{n+1/2}, \tag{3.52}$$

$$a^{n+1} = a(r^{n+1}), \tag{3.53}$$

$$v^{n+1} = v^{n+1/2} + \frac{1}{2}\Delta t a^{n+1}, \tag{3.54}$$

with $\Delta t \equiv t^{n+1} - t^n$. The Verlet method allows the Hamiltonian nature of the SPH algorithm to be preserved (see Price (2012b) and references therein), mainly linear and angular momentum are conserved. The first order prediction of velocity is given by (Price et al. 2017)

$$v^{n+1/2} = v^n + \frac{1}{2}\Delta t a^n, \tag{3.55}$$

$$r^{n+1} = r^n + \Delta t v^{n+1/2}, \tag{3.56}$$

$$v^* = v^{n+1/2} + \frac{1}{2}\Delta t a^n, \tag{3.57}$$

$$a^{n+1} = a(r^{n+1}, v^*), \tag{3.58}$$

$$v^{n+1} = v^* + \frac{1}{2}\Delta t[a^{n+1} - a^n]. \tag{3.59}$$

The error of the first order prediction must be smaller than a tolerance ε as

$$e = \frac{|v^{n+1} - v^*|}{v^{mag}} < \varepsilon, \tag{3.60}$$

and v^{mag} represents the mean velocity of all SPH particles. If $|v^{mag} = 0|$ then the error is $e = 0$ and the default value of the tolerance in the code is set to $\varepsilon = 10^{-2}$. A characteristic feature in SPH codes is to allow the timestepping in simulations to vary, under some constraints. This way the velocities and accelerations of particles are calculated in small increments, decreasing the computational cost (Price et al. 2017). From several criteria that rule a particle timstep in Phantom, the primary constraint is the *Courant* condition

$$\Delta t_C = C_{cour}\frac{h}{v_{sig}}, \tag{3.61}$$

where $C_{cour} = 0.3$ and is the default value for the Courant factor and v_{sig} represents the maximum signal speed over all the neighbouring particles assuming that $\alpha^{AV} = max(\alpha^{AV}, 1$; with AV denoting the artificial viscosity).

This way the Courant condition guarantees that the compressional waves and similar features have three timesteps for minimum to move through a particle, implying that these features can be well resolved in time. If an additional constraint, mainly the *force* condition, is applied based upon forces on the particles, then

$$\Delta t_f^j = C_{force}\sqrt{\frac{h_j}{|\mathbf{a}_j|}} \quad \text{and} \quad \Delta t_{sink-gas}^j = C_{force}\sqrt{\frac{h_j}{|\mathbf{a}_{sink-gas}|}}, \tag{3.62}$$

---

[4] Leapfrog integration is a particular approach to write two coupled first-order ordinary differential equations with finite differences

with $C_{force} = 0.25$, being the default value, h_j represents the smoothing length of the particle j and $|\mathbf{a}_j|$ is the magnitude of the acceleration on the particle j. The previous conditions are known as the *"force condition"* and the *"sink-gas force condition"*, respectively. The timestep for a specific particle is given by the minimum of these conditions, such (Price et al. 2017)

$$\Delta t_j = min(\Delta t_C, \Delta t_f^j, \Delta t_{sink-gas}^j), \tag{3.63}$$

where the minimum value of Δt_j for all particles j in the simulation will generally be set as the timestep of the simulation.

3.9.2 Sink particles

Sink particles are a feature in the Phantom code that can be used to approximate stars to compact objects, i.e., the cores of stars to compact objects like black holes (the case in the present work). These particles are used to accrete gas around them under determined conditions and so these are different of other particles (point mass; e.g., dust and dark matter) in some characteristics like:

i) sink particles gravitational interaction is computed with a collisional direct N^2 summation;

ii) sink particles can accrete gas;

iii) sink particles can store the accreted angular momentum and the accreted mass.

In this section the particle labels will be denoted by a, b and c while the labels i, j will refer to vector indices (Price et al. 2017). The motion of sink particles can be expressed with

$$\frac{\mathrm{d}v_i}{\mathrm{d}t} = -\sum_{j=1}^{N_{sink}} GM_j\phi'_{ij}(\varepsilon)\hat{r}_{ij} - \sum_{b=1}^{Npart} Gm_b\phi'_{ib}(\varepsilon_{ib})\hat{r}_{ib}, \tag{3.64}$$

where the softening length of the sink-gas is represented by ε_{ib} which is set to be the maximum of the softening length of the sink particles and the softening length of the gas particle as $\varepsilon_{ib} \equiv max(\varepsilon, \varepsilon_b)$.

The equivalent of such motion in acceleration of SPH particles is

$$\mathbf{a}^a_{sink-gas} = -\sum_{j=1}^{N_{sink}} GM_j\phi'_{aj}(\varepsilon_{aj})\hat{r}_{aj}, \tag{3.65}$$

in both equations ϕ'_{ab} represents the softening length kernel. If the sink has a softening length of zero there is no softening length applied on sink-gas interactions and in such cases the accelerations of sink-gas becomes (Price et al. 2017)

$$\mathbf{a}^a_{sink-gas} = -\sum_{j=1}^{N_{sink}} \frac{GM_j}{|r_a - r_j|^3} r_{aj}. \tag{3.66}$$

3.9.3 Self-gravity

Self-gravity in Phantom is calculated using direct summation of the kernel softened gravitational interaction between a target particle and its neighbour particles. For long range interactions, these are introduced by adding acceleration between the centre of two nodes, accounting for the quadropole moment of the node, which means that long range interactions are computed by hierarchical grouping of the particles. A solution to Poisson's equation

$$\nabla^2\Phi = 4\pi G\rho(r) \tag{3.67}$$

$$\mathbf{a}_{selfgrav} = -\nabla\Phi \tag{3.68}$$

is implied by selg-gravity, where Φ represents the potential, ρ is the continuous fluid density and the acceleration term $\mathbf{a}_{selfgrav}$ in the equation of motion is given by (3.68) (Price et al. 2017).

3.9.4 External forces

In terms of potentials the code uses a simple external force, which can be described by

$$\Phi_a = -\frac{GM}{r_a}; a_{ext} = -\nabla\Phi_a = -\frac{GM}{|r_a|^3}\hat{r}_a \tag{3.69}$$

that represent a point mass at the origin and $r_a \equiv \sqrt{r_a \cdot r_a}$, so with this potential the particles that are found in a certain distance of the origin can be accreted (Price et al. 2017). To better reproduce some important features of the Schwarzschild (Schwarzschild 1916) spacetime (e.g., orbital frequencies) the code incorporates a module with a Newtonian potential implemented by Tejeda and Rosswog (2013), given by

$$a_{ext} = -\frac{GM_r}{r^3}f^2 + \frac{2R_g v(v\cdot r)}{r^3 f} - \frac{3R_g r(v\times r)^2}{r^5} \tag{3.70}$$

where the acceleration term is a_{ext}, $R_g \equiv GM/c^3$ and $f \equiv (1-2R_g/r)$. A semi-implicit solution is needed for the velocity terms, so iterations for the corrector step with a fix point will bring the velocity to a certain tolerance of the previous value from the previous iteration (Price et al. 2017).

3.9.5 Stretch mapping

Non-uniform density profiles can be set up with *stretch mapping*. Spherical distributions (Herant 1994) can be implemented for any density profile through one direction (Price and Monaghan 2004) where the particles are initially setup in a uniform distribution, i.e., the particles should keep their relative position in the mass distribution. In order to solve the coordinate system for each particle, the equation

$$f(x) = \frac{M(x)}{M(x_{max})} - \frac{x_0 - x_{min}}{(x_{max}) - x_{min}} = 0 \tag{3.71}$$

where x_0 is the initial coordinate for the particle and $M(x)$ represents the density profile that is integrated over the coordinate direction, such

$$M(x) \equiv \int_{x_{min}}^{x} \rho(x')dxS(x')dx' \tag{3.72}$$

with the element area represented by $dS(x')$ being geommetrically dependent, which direction is

$$dS(x) = \begin{cases} 1 & \text{cartesian, cylindrical or spherical along } \phi, \theta \text{ or } z \\ 2\pi x & \text{cylindrical along } r \\ 4\pi x^2 & \text{spherical along } r \end{cases} \tag{3.73}$$

For each particle (3.71) is resolved iteratively with Newton-Raphson (Cirnu and Badralexi 1995) method as

$$x = x - \frac{f(x)}{f'(x)} \tag{3.74}$$

with $f'(x)$ given by

$$f'x = \frac{\rho(x)dS(x)}{M(x_{max})} \tag{3.75}$$

until the iterations reach $|f(x)| < 10^{-9}$. The stretch mapping is achieved by changing optional arguments where the density function is chosen as needed.

3.9.6 Damping

The damping parameter fd is used to relax the particle distribution into equilibrium (Gingold and Monaghan 1977) in a way that an amount of the kinetic energy is removed every timestep and an external acceleration is added, such

$$a^{a}_{ext,damp} = -fdv \tag{3.76}$$

where in the case of small values of fd, a fraction of the kinetic energy of the particles is taken in every timestep.

3.10 Tests

The test algorithms in Phantom pretend to demonstrate the correct implementation of the code and the results obtained from such tests are the same as those achieved by other codes. In the numerical tests the quintic spline kernel M_6 is used with the softening length $h_{fac} = 1.0$ gives a mean neighbour number of 113 for the 3D cases. If the cubic spline kernel $h_{fac} = 1.2$ is used, the majority of the tests results are approximatly the same with a mean number of neighbour particles of $\approx$ 58.

3.10.1 The Sod shock tube

The Sod shock tube test from Sod (1978) is a benchmark in the shock tube problems. The test executed in Phantom is in 3D and the initial conditions in the tube are set to $[\rho, P] = [1, 1]$ for the left side of the tube ($x \leq 0$) and $[\rho, P] = [0.125, 0.1]$ for the right side of the tube ($x > 0$), having an initial discontinuity at $x = 0$ and the initial velocities and magnetic field are zero. An adiabatic equation of state with the adiabatic index $\gamma = 5/3$ is used, with periodic boundaries for y and z. The set up of the density contrast can be challenging in 3D SPH and this problem is set up in Phantom with the particles being initially on a close packed lattice, fixed in number on the $y(z)$ direction to ensure the continuity across the periodic boundaries, where the spacing in the x direction is arranged to give the correct density over the subdomains.

The density profile contrast is initialized with equal mass for all the particles with resolution of $256 \times 24 \times 24$ at $x \epsilon [-0.5, 0]$ initially and $128 \times 12 \times 12$ particles for $x \epsilon [0, 0.5]$. Boundary conditions along the x direction is achieved by choosing the first and last rows of particles along that direction to be boundary particles (particle properties are set constant).

The results of the test implemented in Phantom are shown in Figure 3.1 which represents the test for $256 \times 24 \times 24$ at $x \in [-0.5, 0]$ initially and $128 \times 12 \times 12$ particles for $x \in [0, 0.5]$, where the artificial viscosity $\alpha^{AV} = 1, \beta^{AV} = 2$ and the artificial conductivity $\alpha_u = 1$ are code defaults. The exact solution given by the solid red line shows the shock wave at the right side which is followed by a contact discontinuity and a rarefaction fan on the left side. The distribution of the particles given by the numerical solution represented by the black dots trace with accuracy the features of the exact solution which gives the global results very similar to those from Sod (1978).

3.10.2 The Brio & Wu shock tube

The MagnetoHydrodynamics (MHD) Shocktube problem from Brio and Wu (1988) has been extensively discussed (Wu 1988; Dai and Woodward 1994) over the years, but has become a benchmark for the

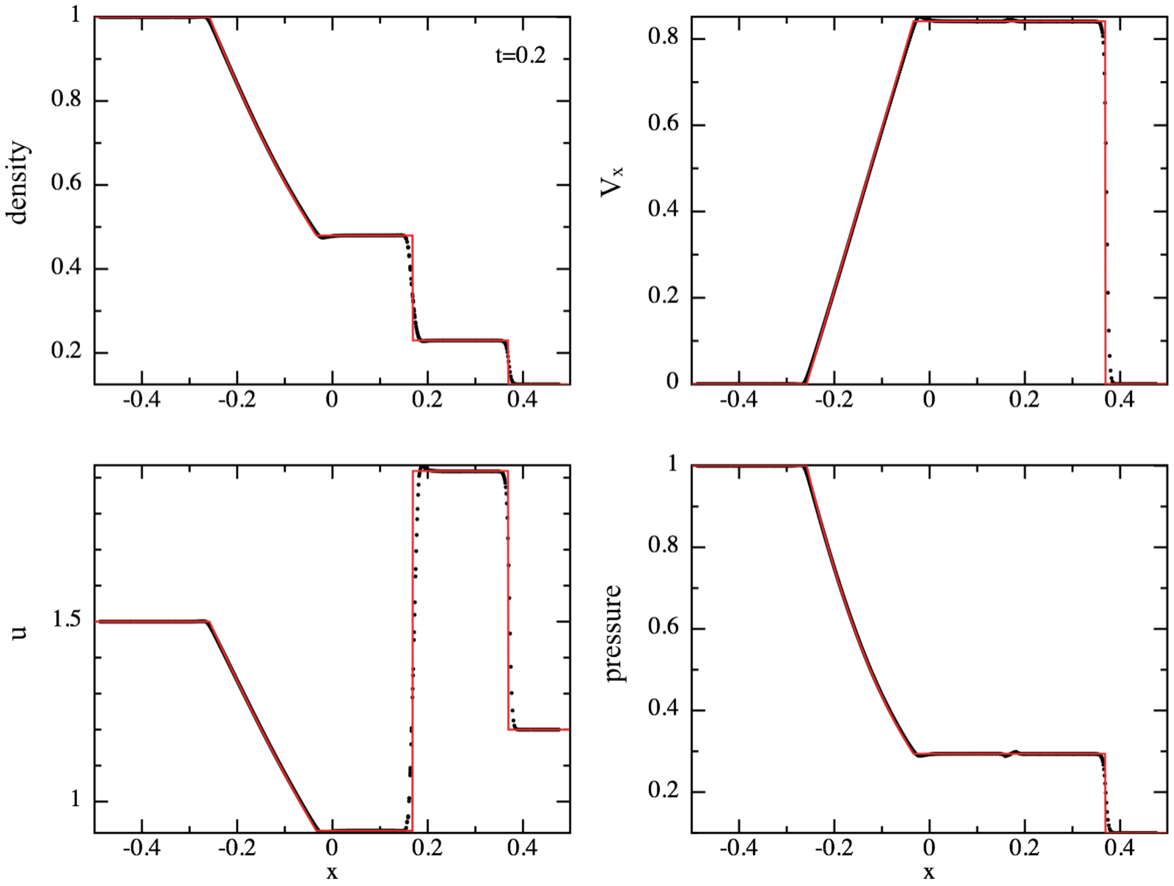

Figure 3.1: The Sod shock tube test with the particles (black dots) against the exact solution (red lines).

numerical tests of MHD. The Brio and Wu (1988) test problem is implemented with the same initial conditions of the latter paper, with a resolution of $256 \times 24 \times 24$ at $t = 0.1$ in 3D, set initially with $x \in [-0.5, 0.5]$ in a close packed lattice (Figure 3.2). All particles are projected against the x-axis represented by the black dots and the numerical solution (in this case from Balsara (1998)) is represented by the solid red lines and the artificial viscosity was set to $\alpha^{AV} = 1$. The test represents the propagation of several waves that grow at the same speed.

This test was set up with $\rho = 1, P = 1, B_y = 1$ and $B_z = 0$ for $x \leq 0$ and for $x > 0$ was set with $\rho = 0.125, P = 0.1, B_y = -1$ and $B_z = 0$ where the initial velocities are zero, $B_x = 0.75$ and $\gamma = 2$. Equal mass particles were used for the initial density contrast in a close packed lattice with resolution of $256 \times 24 \times 24$ particles for $x \: \epsilon \: [-0.5, 0.5]$.

The MHD shock tube test involves composed structures that present shocks and rarefactions that propagate at the same time and so belong to the same wave family (Brio and Wu 1988). The solution for this test shows the complex structures of the shocks that can be formed via the different waves in MHD and consists in the components given by a set of waves moving to the left which are a fast rarefaction fan and a slow compound wave that is composed by a slow rarefaction coupled to a slow shock and the waves that move to the right are given by a contact discontinuity, a fast rarefaction fan and a slow shock. The results obtained with Phantom capture with accuracy the set of waves generated and exhibit good agreement with those given by Brio and Wu (1988) and Stone and Norman (1992).

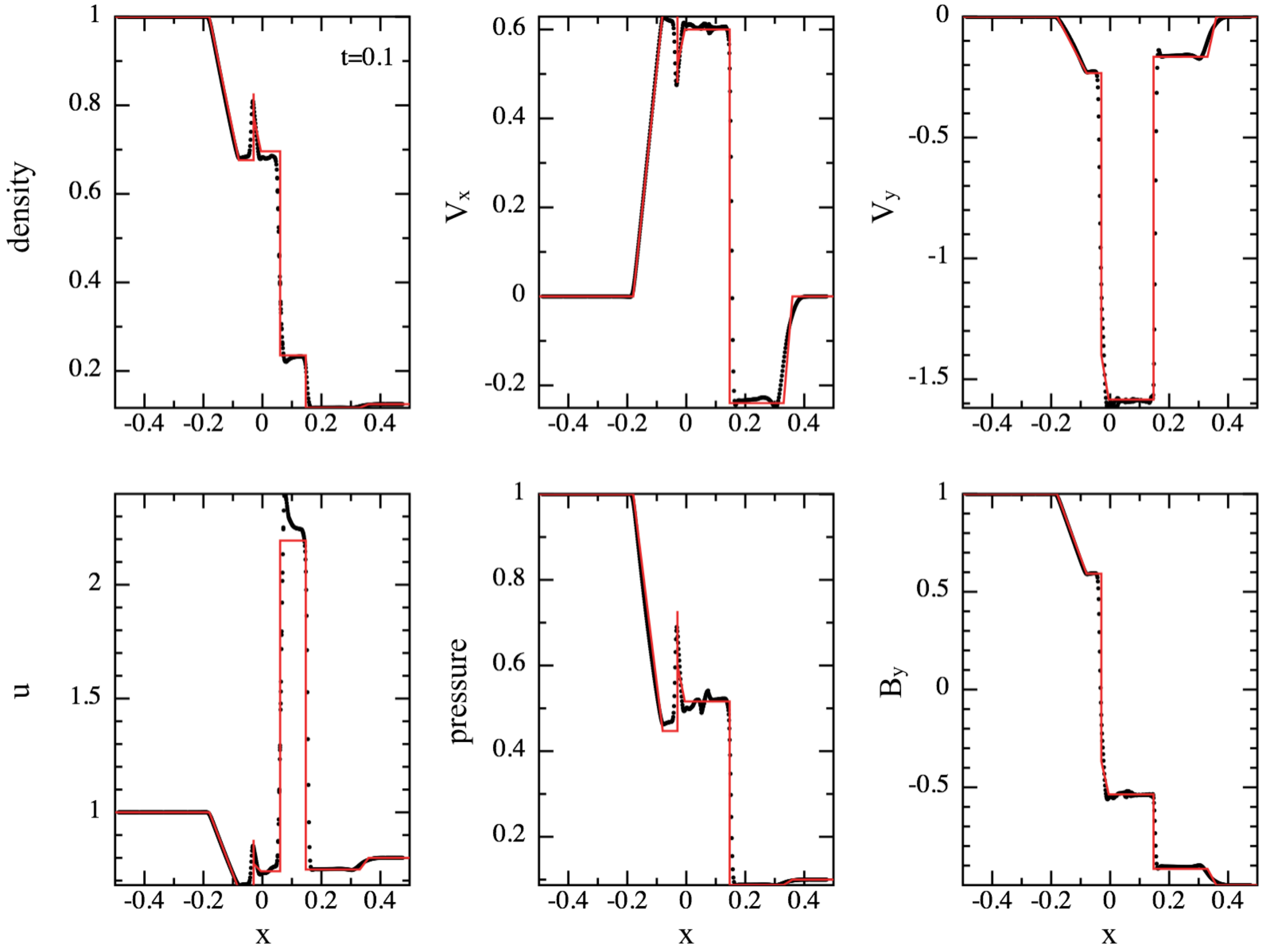

Figure 3.2: The MHD shock tube test with particles (black dots) against numerical solution (red lines) with $256 \times 24 \times 24$ particles placed in a close packed lattice at $t = 0.1$.

3.10.3 The Sedov-Taylor blast wave

The blast wave test from Taylor (1950); Sedov (1959) has a spherical geometry and is well suited for the individual timestepping algorithm. The test consists in the propagation of a blast wave into a populated medium of inactive particles with the consequence of loss of energy conservation (Saitoh and Makino 2009). The set up of the problem consists in a uniform periodic box with $x, y, z \ \epsilon \ [-0.5, 0.5]$ with the thermal energy $\neq 0$ in a sphere around the origin. The equation of state is adiabatic with $\gamma = 5/3$.

The total thermal energy in the blast is $E_0 = \sum_a m_a u_a = 1$, which is distributed over the particles that have $r < R_{kern} h_0$ (with the smoothing length kernel) such

$$u_a = \begin{cases} E_0 W(r, h_0), & r/h_0 \leq R_{kern} \\ 0, & r/h_0 > R_{kern} \end{cases} \tag{3.78}$$

with $r = \sqrt{x^2 + y^2 + z^2}$, which is the radius of the particle and h_0 is twice the smoothing length of the particles.

The results obtained with Phantom for this test are shown in Figure 3.3, where the simulation of the Sedov blast wave for 32^3, 64^3 and 128^3 particles, respectively, are projected in terms of the density as a function of the radius. The numeric solution is represented by the black dots and the exact solution is represented by the solid red line. This test resolves the shock position more accurately with increasing number of particles as the thermal energy is better conserved.

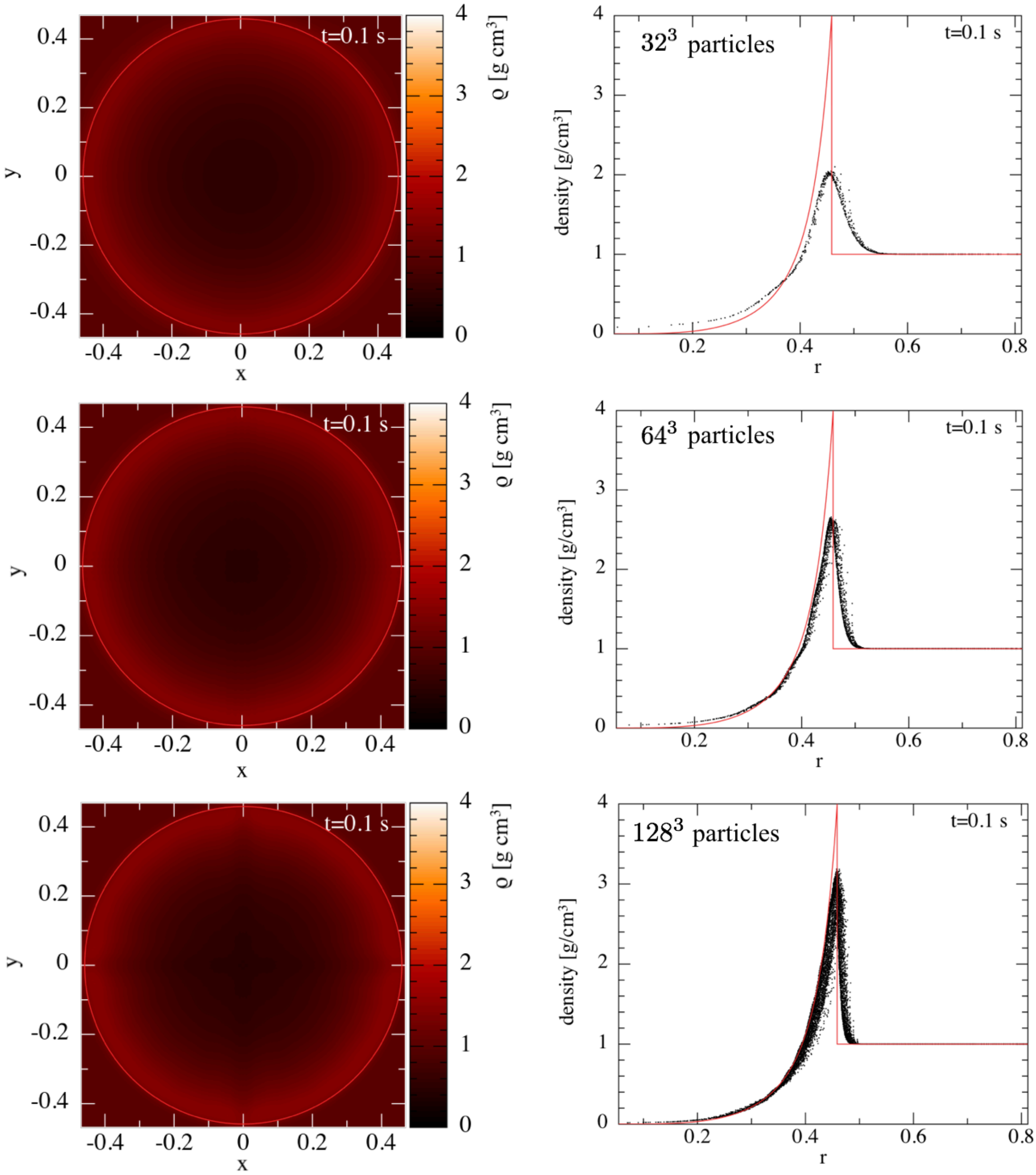

Figure 3.3: The Sedov blast wave solutions for smoothed explosion energy test with $32^3, 64^3$ and 128^3 particles (black dots) compared with the exact solution (solid red line) placed on a uniform cubic lattice.

3.10.4 The Orszag-Tang vortex

This MagnetoHydrodynamics (MHD) problem was developed by Orszag and Tang (1979) and has been extensively used to test MHD codes in astrophysics.

The Orszag-Tang vortex test was set up in a uniform density periodic box with $x, y \epsilon [-0.5, 0.5]$. To set up the 2D problem in 3D the boundary in the z direction was set to $\pm 2\sqrt{6}/n_x$, where n_x represents the initial number of particles along xx.

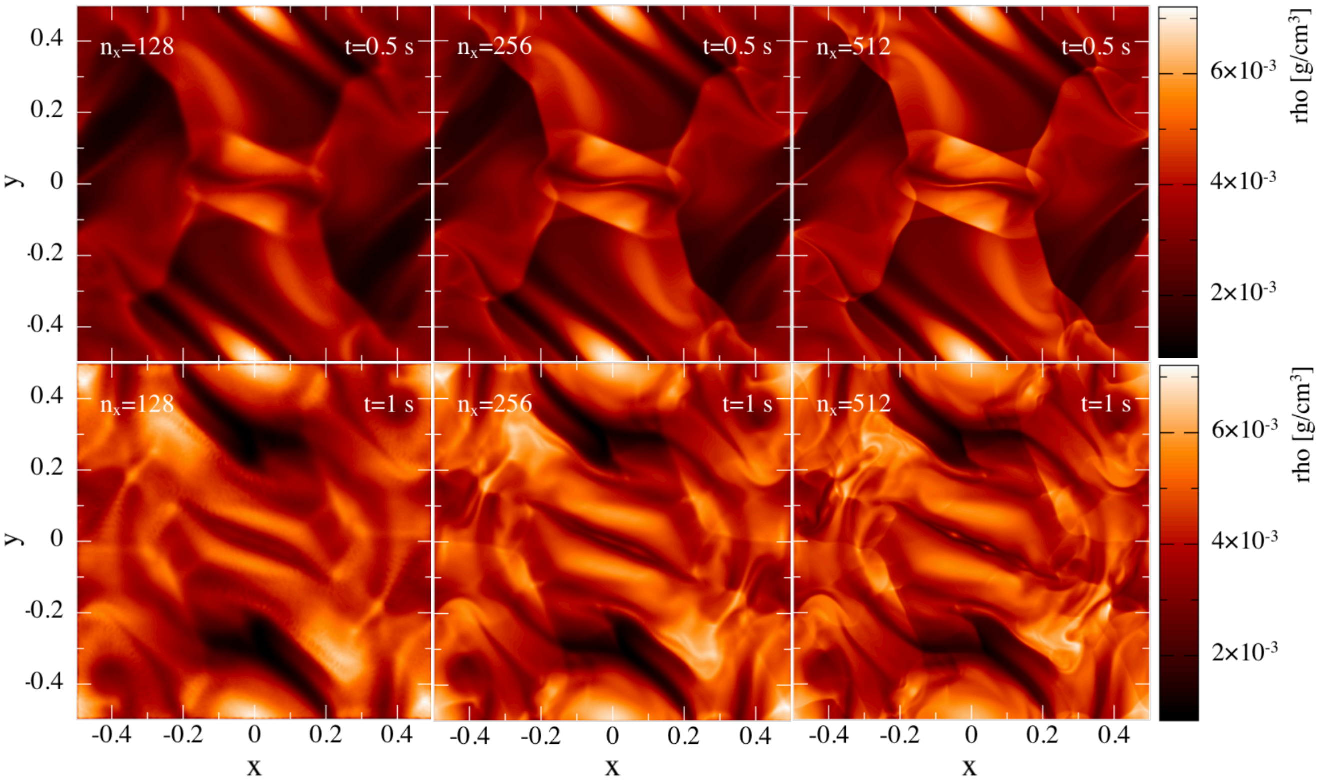

Figure 3.4: The Orszag-Tang vortex test with increasing resolutions (from left to right) of $128 \times 128 \times 128$, $256 \times 256 \times 256$ and $512 \times 512 \times 512$ for equal mass of the SPH particles.

The initial values were set with $\beta_0 = 10/3$ for the plasma, $\mathcal{M}_0 = v_0/c_{s,0} = 1$ for the Mach number, $[v_x, v_y, v_z] = [-v_0\, sin(2\pi y'), v_0\, cos(2\pi x'), 0.01 v_0]$ for the velocity field and for the magnetic field $[B_x, B_y, B_z]$=$[-B_0 sin(2\pi y')]$, with $v_0 = 1, B_0 = 1/\sqrt{4\pi}, x' \equiv x - x_{min}, y' \equiv y - y_{min}$, which gives $P_0 = 1/2B_0^2/\beta_0 \approx 0.133$ and $\rho_0 = \gamma_0\ P_0\ \mathcal{M}_0 \simeq 0.211$ and $\gamma = 5/3$ is the adiabatic index for the equation of state. In Figure 3.4 the results for three different resolutions are shown, at $t = 0.5$ s (top panel) and $t = 1$ s, for $n_x = 128$, $n_x = 256$ and $n_x = 512$ (bottom panel), respectively. At $t = 0.5$ s it is observed that the shocks are well defined as also the reconnecting layer of magnetic field where it can be observed the dense filament of captured material which can be compared to Fig. 6 of Dai and Woodward (1998) and Fig. 22 of Stone et al. (2008). By $t = 1$ s the current sheet may achieve the instability mode, where some magnetic islands will be developed and can only be observed at the higher resolution in bottom panel for $n_x = 512$) of Figure 3.4 due to the small numerical dissipation, which can be seen in Figure 32 of Price et al. (2017).

3.10.5 The Kelvin-Helmoltz Instability

The Hydrodynamics (HD) Kelvin-Helmoltz Instability[5] (K-H) test in Phantom is implemented through the adopted set up by Robertson et al. (2010). The density and shear velocity along the y direction are given by

$$\rho(y) = \rho_1 + R(y)[\rho_{12} - \rho_{11}] \tag{3.77}$$

$$v_x(y) = v_1 + R(y)[v_2 - v_1] \tag{3.78}$$

with $\rho_1 = 1, \rho_2 = 2, v_1 = -0.5$ and $v_2 = 0.5$, the pressure is constant with $P = 2.5$ and $\gamma = 5/3$.

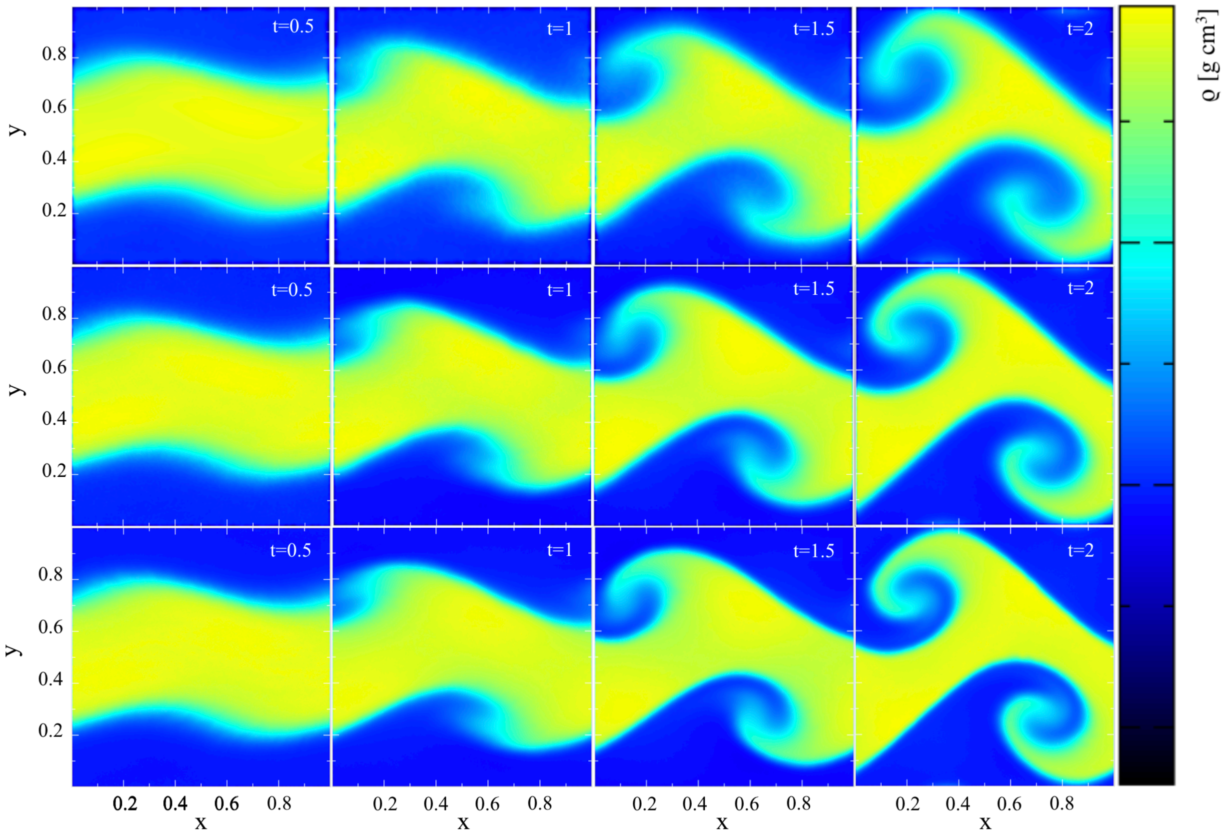

Figure 3.5: The K-H test with resolutions from top to bottom $64 \times 74 \times 12$, $128 \times 148 \times 12$, $256 \times 296 \times 12$. Resolutions for this test are from top to bottom: for equal mass of the SPH particles.

The ramp function used to smoothen the initial density constrast is given by

$$R(y) \equiv [1 - f(y)][1 - g(y)] \tag{3.79}$$

where f is represented by

$$f \equiv \frac{1}{1 + exp[2(y - 0.25)/\Delta]} \tag{3.80}$$

$$g \equiv \frac{1}{1 + exp[2(0.75 - y)/\Delta]} \tag{3.81}$$

with $\Delta = 0.25$. The velocity is perturbed along the y direction by

---

[5] This instability can occur when there is a difference in velocities along the interface between two fluids (Frank et al. 1996).

$$v_y = 0.1sin(2\pi x) \tag{3.82}$$

The Kelvin-Helmoltz Instability is set up in a 3D dimensional box.

A uniform close packed lattice is set up in a periodic box of $1 \times 1 \times \sqrt{24}/n_x$, with n_x representing the initial resolution along the x direction with its thickness being set with spacings of 12 particles along the z and the box dimensions are set between $[0, 1]$ for x and y. The initial density profile is set up by the stretch mapping along the y direction with a 2:1 density treshold smoothed transition.

The results obtained for this test problem are consistent to those obtained by (Robertson et al. 2010) and a cross-section of the density at $z = 0$ for three resolutions, $n_x = 64$, $n_x = 128$ and $n_x = 256$ respectively, is represented in Figure 3.5.

3.10.6 The MHD rotor

The MHD rotor test problem was developed for the study and test of the propagation of rotational discontinuities. The setup of this test is implemented in 3D in Phantom in the same way as in Monaghan and Price (2005) and following Tóth (2000).

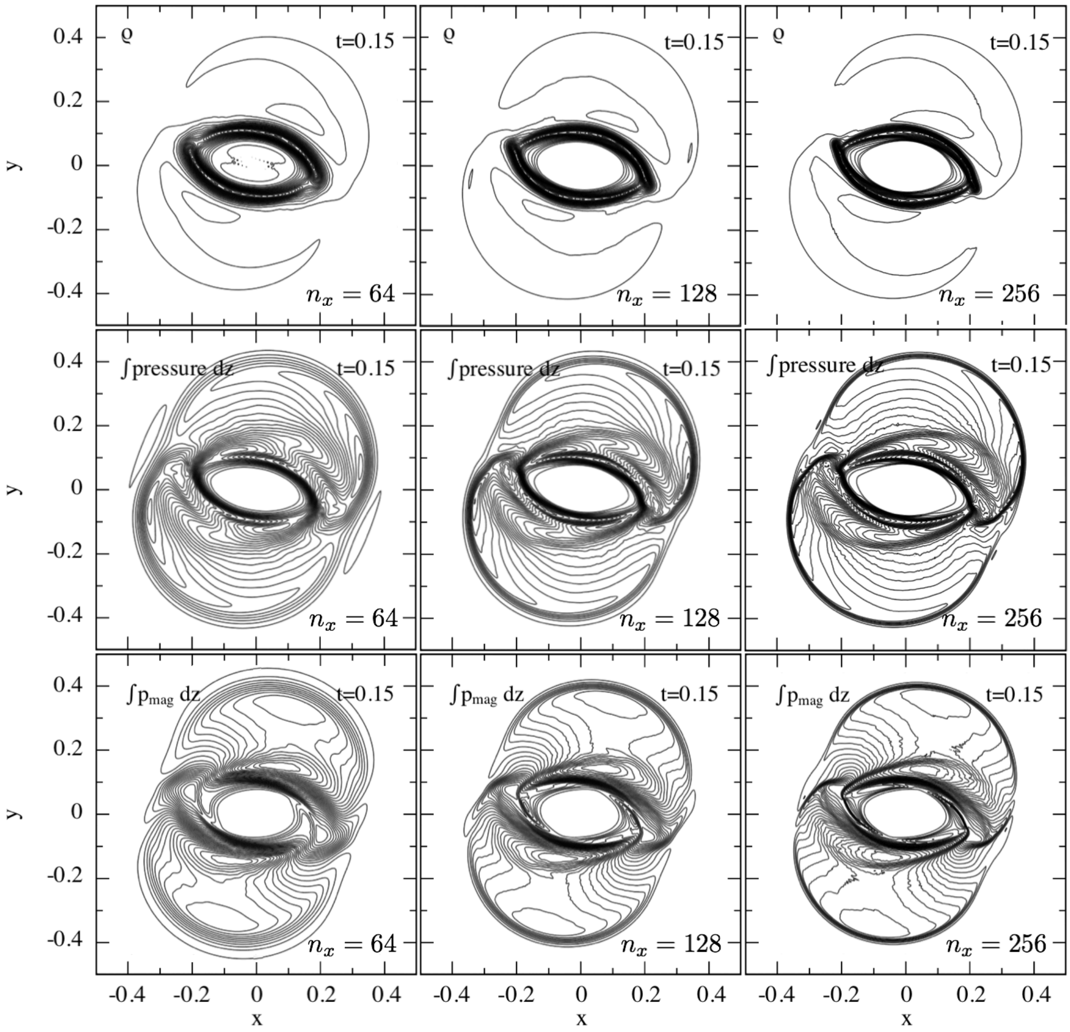

Figure 3.6: Plots of the MHD rotor problem for density (top panel), pressure (middle panel) and magnetic pressure (bottom panel) are shown with 30 contours equally spaced. Resolutions increase from left to right, respectively, $n_x = 64, n_x = 128$ and $n_x = 256$.

The test consists in a dense rotating disc with density $\rho = 10$ which is set up with a cylindrical radius $R = 0.1$ on a periodic box with $[x, y] \in [-0.5, 0.5]$ and the boundary in z is $-\sqrt{6}/2nx, \sqrt{6}/2nx$ on a closed packed lattice. The setup has an initial density contrast unsmoothed placing two uniform lattices of particles which are spaced inside the cylinder by the inverse cube root of the density contrast.

The initial velocities are set to $v_{x,0} = -v_0(y - y_0)/r$ and $v_{y,0} = v_0(x - x_0)/r$, where $v_0 = 2$ and $r = x_2 + y_2$, for $r < R$. The density is $\rho = 1$ and initial pressure is uniform with $P = 1$ and the magnetic field is $[B_x, B_y, B_y, B_z] = [5/\sqrt{4\pi}, 0, 0]$ and $\gamma = 1.4$. In the highest resolution of $n_x = 256$ the number of particles is 1145392.

The results for the density, pressure and magnetic pressure at resolutions of $n_x = 64, n_x = 128$ and $n_x = 256$ are shown in Figure 3.6, where thirty contours of equal space between the minimum and the maximum are applied in each plot. The sharp discontinuities and the symmetry of the solution (which is preserved by the numerical scheme) can be compared for $n_x = 256$ in Phantom against the grid of 400×400 cells in Stone et al. (2008).

3.10.7 The Galaxy merger

The SPH implementation of the galaxy merger test requires gravity for the interaction of multiple particles (e.g., stars, gas, dark matter) where the particles interact hydrodynamically between them and the gas interacts with itself Price et al. (2017).

The evolution of the galaxy merger implemented in Phantom can be compared with the results obtained with the Hydra N-body/SPH code (Couchman et al. 1995; Thacker and Couchman 2006). In the Phantom code the galaxy merger test was implemented with GalacTics (Kuijken and Dubinski 1995; Widrow and Dubinski 2005; Widrow et al. 2008) in order to obtain a Milky Way-type galaxy with a stellar disc, a stellar bulge and a dark matter halo Price et al. (2017). The stellar disc was duplicated in the $x = y$ plane so this way there are no coincidences with star particles and the gas disc can be created taking 10% of the total stellar mass. The gas halo was encapsulated within the dark matter halo with a temperatuyre profile from Kaufmann et al. (2007) and a β-profile[6] (Cavaliere and Fusco-Femiano 1976; Ettori 2000), where the mass from the hot gas halo was taken from the dark matter particles to keep a total halo mass (Price et al. 2017).

The merger of the galaxies (after duplication of the galaxy to obtain two similar structures) was set with a distance of 70 kpc between them and approaching each other on a parabolic trajectory (Wurster and Thacker 2013). In Table 3.1

Component	$M/M_\odot(10^{10})$	$m/M_\odot(10^5)$	N
Dark matter halo	89.92	89.92	100 000
Hot gas halo	0.60	2.77	21 619
Stellar bulge	1.34	18.10	7 407
Stellar disc	3.56	18.10	19 662
Gas disc	0.54	2.77	19 662

Table 3.1: Components of each galaxy in the galaxy merger test in Phantom. The total mass is M, the particle mass is m and the total number of particles is N for each component, respectively.

The evolution between $t = 100$ Myr to $t = 1.4$ Gyr of the column gas density obtained for the galaxy merger test with Phantom is shown in Figure 3.7 and the insets on the bottom right corner represent the galaxy merger obtained from the Hydra code. The distance that separates the two galaxies at $t = 450$ Myr is $\approx$ 61 kpc in Phantom and $\approx$ 59 kpc in Hydra. At $t = 905$ Myr and $t = 875$ Myr for Phantom and Hydra, respectively, the second encounter at the pericentre of their trajectories represents a difference of $\sim 3.4\%$ since the initial moment (beginning of simulation) and the density in Phantom is $\sim$ 10 times

---

[6] Observed surface brightness that constrains the gas density distribution

lower, possibly due to a more diffuse core Price et al. (2017).

Some significant differences in the algorithms from both codes are indicated by Price et al. (2017), as follows.

1) Gravity solver - In Phantom a main optimization of the treecode is to compute the long-range gravitational interaction per leaf-node instead of computing it per particle, while in Hydra an adaptive particle-mesh algorithm is used.

2) Smoothing length - The smoothing length (h_i) is calculated self-consistently and no lower limit is fixed while in Hydra the smoothing length is limited as $h_i = max(h_i, h_{min})$.

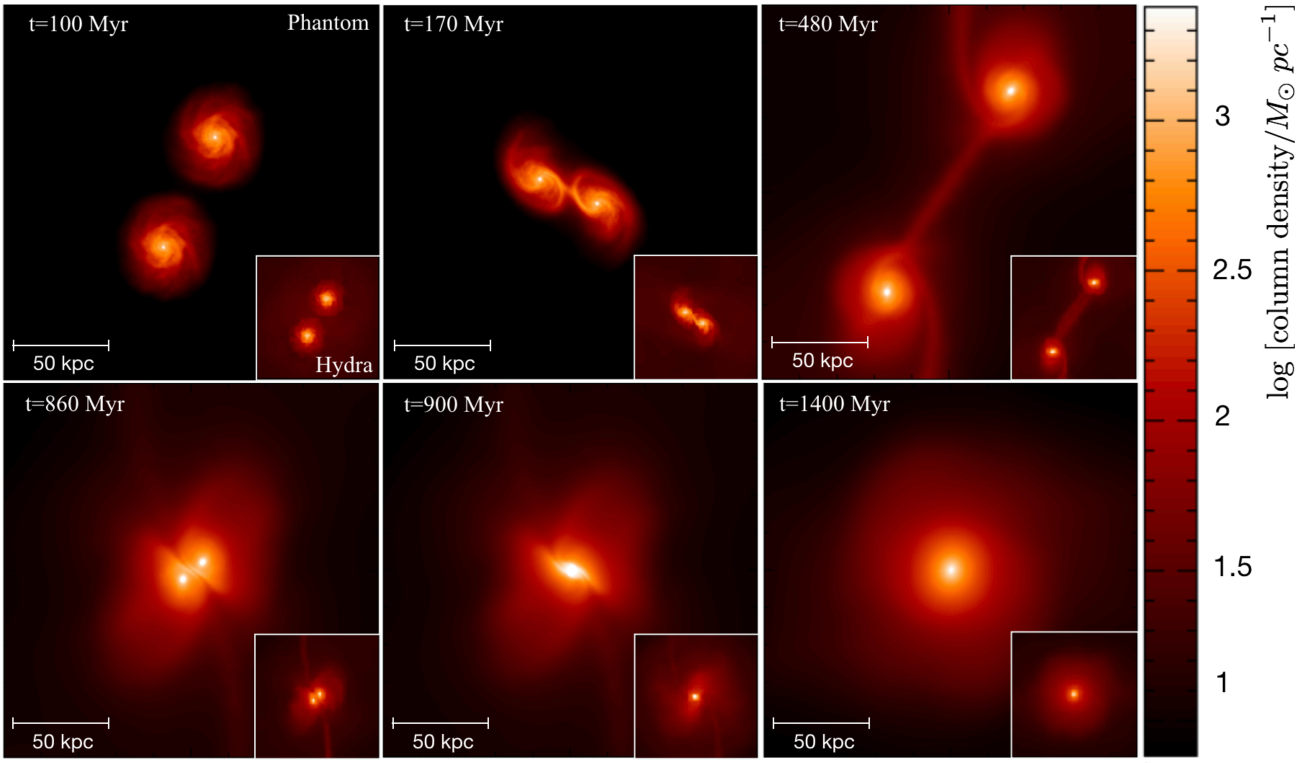

Figure 3.7: The galaxy merger test from Phantom with the evolution of the gas density of two Milky Way-type galaxies. In the bottom right corner of each frame the inset of the same test with the Hydra code is shown.

The more recent code Phantom presents some differences from the Hydra code which may be attributed to the improved SPH algorithms incorporated in the first. This comparison between the two codes was simplified as no star formation recipe is considered as well as no black holes and no feedback from Active Galactic Nuclei (AGN), thus only the SPH and gravity algorithms were taken into account.

3.10.8 Summary

The Smoothed Particle Hydrodynamics (SPH) method is based on the Lagrangian method that deals with the fluid equations where discrete particles are used with hydrodynamic properties evaluated at particle positions from the calculated weighted average values on other particles. This method is implicitly adaptive due to the smoothing of the particles over a volume of fixed mass and is also suited to deal with vacuum boundary conditions.

In SPH mass, momentum and energy are inherently conserved.Though magnetic fields were not considered for the present work, the SPH approximation equations for the magnetic fileds are presented.

The Phantom code was developed by Price et al. (2017) over the last decade for astrophysical applications in 3D. Presented as a fast, parallel and low-memory SPH code it is specially suited for high energy astrophysics (stellar, galactic and planetary) and studies of accretion phenomena such as accretion discs or black hole accretion. Some of the algorithms of the code were outlined as these were extensively used in this work (e.g., self-gravity, external forces).

In terms of the accuracy and performance the Phantom code is supported with several standard and well studied tests extensively used in astrophysics with known solutions or analytic solutions which were compared to the results obtained with the code. The results obtained with some of these tests can be compared to those obtained with the most extensively used Eulerian codes such as Zeus-MP (Hayes et al. 2006), as for example, the MHD vortex and the MHD rotor tests.

4

Parabolic and Elliptic TDEs - Results from numerical simulations

4.1 Introduction

The tidal disruption of a star by a $\sim 4 \times 10^6 M_\odot$ Schwarschild SMBH is investigated. For this configuration the black hole is modelled by an external potential in the Keplerian regime with a tidal radius of $R_T = (M_{BH}/M_*)^{1/3} R_*$. Two sets of Parabolic and Elliptic TDEs involving a star describing different orbits, with different penetration parameters and consequently different pericentre distances R_P were implemented. TDEs are a complex process that can be analitically described to a reasonable precision (Rees 1988) though are also a non-linear interaction between gravity, gas dynamics and radiation, to name a few, which for a realistic approach to study such disruptive processes, numerical simulations represent a reliable tool (Kochanek 1994; Evans and Kochanek 1989; Bonnerot et al. 2016).

The study of TDEs in this work is based on the type of star and its mass, its polytropic index, the characteristic black hole (for this work a Schwarschild black hole was chosen, with a mass that is approximately the mass of the central SMBH of the Milky Way), the eccentricity of the star for parabolic and elliptic orbits, and the penetration parameter b. For a fixed penetration parameter, R_P scales with $(M_{BH})^{1/2}$ and the R_P crossing time does not depend on the M_{BH}. As $R_P \ll R_T$, the asymmetry of the tidal field becomes less significant and the tidal field strength at R_P, for encounters of the order $10^6 : 1$ is $\approx 3\%$ (Guillochon et al. 2011) and even more for $4 \times 10^6 : 1$. In TDEs, stars that fall into the gravitational field of a black hole are scattered due to the sphere of influence of the black hole (Magorrian and Tremaine 1999; Wang and Merritt 2004) and for the same penetration parameter the orbits, the asymmetry of the tides and the star's dynamical time $t_{dyn} = \sqrt{R_*^3/GM_*}$ are somewhat very similar, the tidal forces that the star suffers as a function of time are independent of the parameters M_{BH}, ecc, M_* and R_* and so TDEs that have origin in SMBHs can be described by the penetration parameter.

The physical units used in this work are shown in Table 4.1

Quantity	Unit
Mass	1.989×10^{33} g
Length	6.965×10^{8} cm
Time	1.594×10^{3} s
Energy	3.793×10^{48} erg
En/m	1.907×10^{15} erg g^{-1}
Velocity	4.367×10^{7} cm s^{-1}
G	6.670×10^{-11} m^3 kg^{-1} s^{-2}

Table 4.1: Physical units (cgs) used in the simulations of the parabolic and elliptic TDEs.

4.2 Parabolic TDEs

A set of eight TDEs involving a star on a parabolic orbit passing the SMBH at the GCr were performed. A non-rotating Schwarschild black hole with a mass of $M_{BH} \sim 4 \times 10^6 M_\odot$ has a tidal radius of $159R_\odot$ defined by $R_T = (M_{BH}/M_*)^{1/3} R_*$ ($\sim 3.5844556 \times 10^{-6}$ pc). The star considered for these simulations is of solar type with a mass $M_* = 1M_\odot$ and radius $R_* = 1R_\odot$. It was evolved hydrodynamically as a polytropic star with an adiabatic index of $\gamma = 5/3$ and an SPH resolution of 5×10^5 particles, which was relaxed for 1.593×10^5 s with a $\gamma = 5/3$ equation of state was used.

4.2.1 Setup and initial conditions

The simulations begin with the star at r_0 as the starting point. The star begins its trajectory on an orbit that is a function of the eccentricity ($ecc = 1$ for parabolic orbits) and the penetration parameter b. The parameters for the simulations with the initial conditions are shown in Table 4.2.

Model	b	$r_0[R_\odot]$	$R_P[R_\odot]$	$R_T[R_\odot]$
1	0.5	4.49×10^2	3.175×10^2	159
2	1	2.24×10^2	1.587×10^2	159
3	2	1.12×10^2	7.937×10^1	159
4	3	7.48×10^1	5.291×10^1	159
5	5	4.49×10^1	3.175×10^1	159
6	6	3.74×10^1	2.646×10^1	159
7	7	3.21×10^1	2.268×10^1	159
8	8	2.81×10^1	1.984×10^1	159

Table 4.2: Simulation parameters for each model of the parabolic TDEs.

The geometric complexity of a parabolic TDE is illustrated in Figure 4.1 where a $1M_\odot$ star describes an orbit inbound onto the SMBH, where it will experience the effects of the tidal forces from the black hole. After the pericentre passage at R_P the star, describing a trajectory indicated by the dashed black line, is stretched into an elongated shape with lobes forming in the extremities, with the stellar core in the centre. The SMBH is located at the origin (0,0) and the tidal radius R_T is represented by the dotted gray circle.

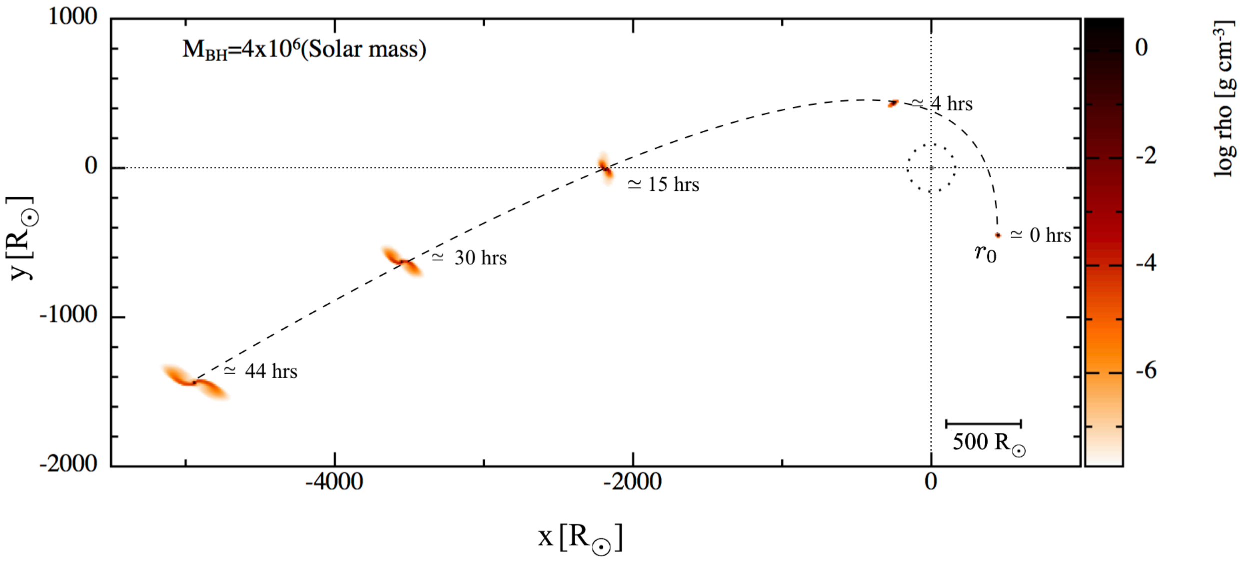

Figure 4.1: Time evolution of a star and its debris in a parabolic orbit around the SMBH.

Though the physical processes regarding TDEs are complex, the numerical simulations have to account for the geometry of the debris that evolves in large length and time scales.
Considering a star approaching the SMBH (see Figure 4.1), if it crosses the R_P inside the R_T it is expected that the star will be tidally disrupted, i.e., if its $R_P < R_T$ defined in (2.17). The initial gas distribution of the star should correspond to a spherically symmetric stellar equilibrium that should occupy only a small fraction of the computational volume as

$$\frac{R_*^3}{R_0^3} \simeq 10^{-8}\left(\frac{M_*}{M_\odot}\right)\left(\frac{10^6 M_\odot}{M}\right) \tag{4.1}$$

where R_0 is the initial position of the star (Guillochon et al. 2009). To such consideration, the numerical simulations should be implemented in the reference frame of the star's centre of mass, where the black hole represents an external force varying in time (Guillochon and Ramirez-Ruiz 2013).

Figure 4.2 represents the initial setup model for the simulations. The computational domain is defined in physical units of solar radius $1R_\odot = 6.957 \times 10^{10}$ cm and time in hours (top right corner). The scale of the computational domain and the mass of the black hole are shown in the bottom right and top left corners, respectively. The TDEs are simulated over five days (120 hours) after disruption and the subsequent evolution of the stellar debris that forms after the impact with the black hole.

The tidal disruption process is simulated by setting the star in motion through the gravitational field of influence of the black hole, modelled as an external potential $\Phi = -GM/R$ (see 3.9.3) with an accretion radius given by the Schwarschild radius (R_S)

$$R_S = 2\frac{GM_{BH}}{C^2} \tag{4.2}$$

where c[1] represents the speed of light and $R_S \approx 17R_\odot$.

---

[1] c $\approx 3 \times 10^8$ m s^{-1}

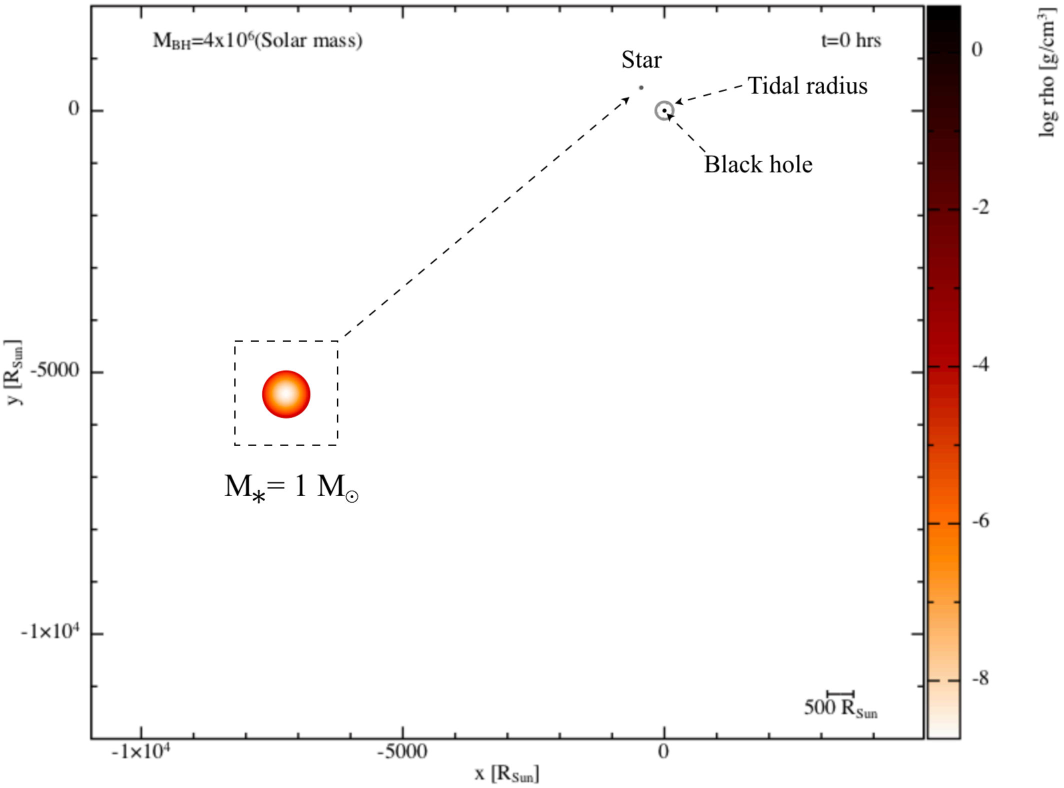

Figure 4.2: Initial configuration of the parabolic simulations with the star and black hole locations.

4.2.2 Results

4.2.2.1 Spatial distribution of debris after R_P

The passage of the star at R_P is essentially defined by the penetration parameter. The scattering of stars to the black hole is achieved when the sphere of influence of the black hole brings the star to typical orbits inbound to the compact object (Guillochon and Ramirez-Ruiz 2013). In these trajectories when the star passes at R_P it suffers the effects of tidal forces from the black hole, even if it is not disrupted, but still affecting the stellar surface. The stellar envelope material is sheared as the gravitational torque applied by the tidal forces distort the star. Depending on the deepness of the encounter a portion of the stellar envelope material becomes unbound from the star being ejected and forming two tidal tails (the near tail will be face on to the black hole side; Tejeda et al. (2017)).

The spatial distribution of the most bound stellar debris increases with time and is due to the geodesic motion of the stellar bound debris. As each event have different periapsis trajectories due to the different penetration parameters, the fluid shifts experienced by each of the events assume different shapes with time and (as long as the self-gravity forces along the stream are small enough) these still increase in thickness (Figure 4.3 for 5 hrs and 30 hrs of evolution of the debris and figures 4.4 and 4.5, for the last 120 hrs). Because the star describes a parabolic orbit, the distance to the black hole as a function of time varies rapidly which causes the Hill radius[2] of the star to be also time-dependent.

In figures 4.4 and 4.5 each model simulation is represented after 120 hrs of evolution of the stream debris after the first passage at R_P. From left to right and from top to bottom the first four panels represent the events of models 1, 2, 3 and 4 whose penetration parameters are respectively $b = 0.5$, $b = 1$, $b = 2$ and

---

[2] The region around the compact object where the object's gravity dominates that of the star that orbits around it (Raymond 2014).

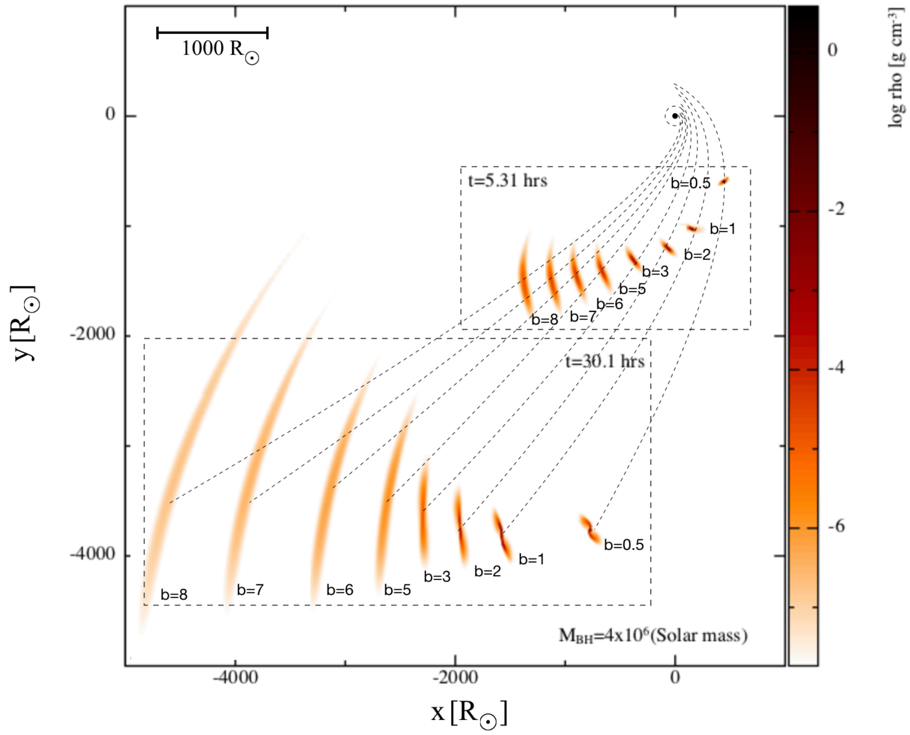

Figure 4.3: Spatial distribution of the debris for all the models at $t \approx 5$ hrs and $t \approx 30$ hrs. The direction of the trajectory is indicated by the black dashed arrow.

$b = 3$. In model 1 the penetration parameter gives the closest approach to pericenter that is $R_P = 2R_T$ the distance of tidal radius to the black hole and the star suffers small deformation from tidal forces. It presents still, the formation of two tidal tails that are the result of the tidal torque applied on the star b y the black hole. In model 2, the passage at pericentre equals that of tidal radius $R_P = R_T$ and reaches the pericenter where it suffers a more pronounced distortion from tidal forces. It can be observed that thought the stellar core is deformed after 120 hrs, the star is able to keep its basic structure. The tidal tails are more distorted, meaning that the tidal forces that act on the star produce bigger deformation. These two models represent the situations of self-gravitating cores that survive to the effects of tidal forces by the passage at R_P. These scenarios are confirmed by numerical simulations (Guillochon and Ramirez-Ruiz 2013) and Mainetti et al. (2017). Model 3 with $b = 2$ represents the limit above which the star suffers effective disruption as the stellar core is more and more stretched and the less bound stellar material (mass envelope of the star) starts to be accreted onto the black hole. This phase is associated to the *pancake* phase (Coughlin 2016). The deeper encounters from model 4 with $b = 3$ and above are less likely than the grazing ones but nevertheless represent a significant portion of TDEs, where for $b \geq 3$ these events are about $1/b = 1/3 \approx 33\%$ (Luminet and Barbuy 1990).

4.2.2.2 Mass removal

When the star enters in the sphere of influence of the SMBH, it becomes scattered from its previous trajectory and starts to describe a typical orbit from apocenter distances that leads to the encounter at R_P producing partial or complete disruption of the star.

The tidal forces at R_P produce distortions on the stellar surface that can reach an amplitude of order unity (Guillochon and Ramirez-Ruiz 2013). As the tidal forces induce a gravitational torque on the stellar envelope material, a portion of it becomes unbound from the star and is ejected to form two tidal tails.

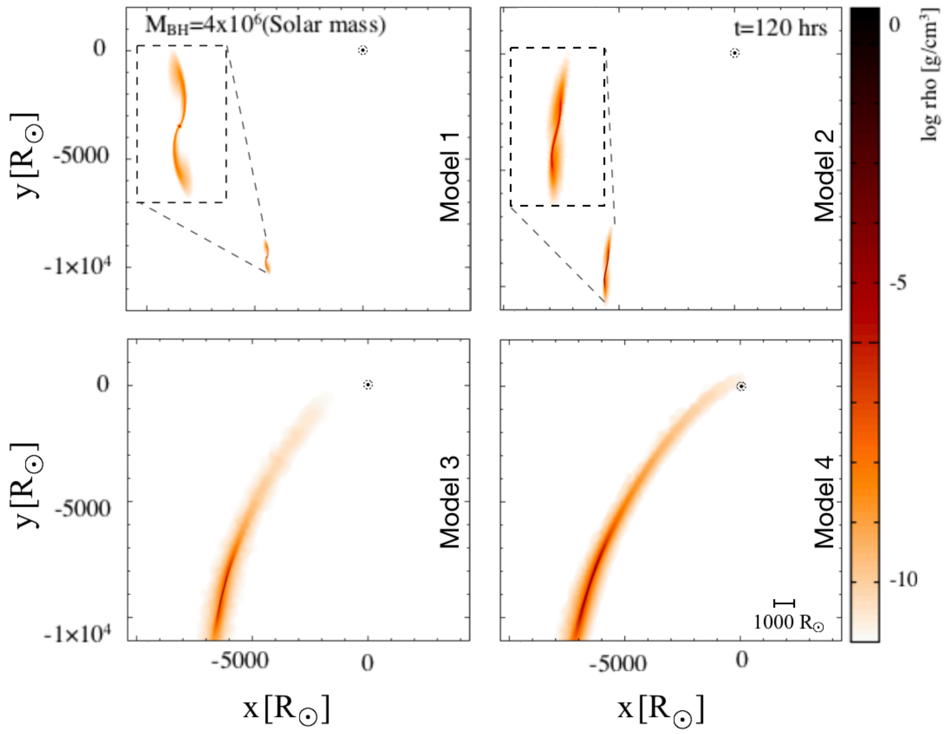

Figure 4.4: Snapshots of the evolution of the spatial distribution of the debris at $t = 120$ hrs.

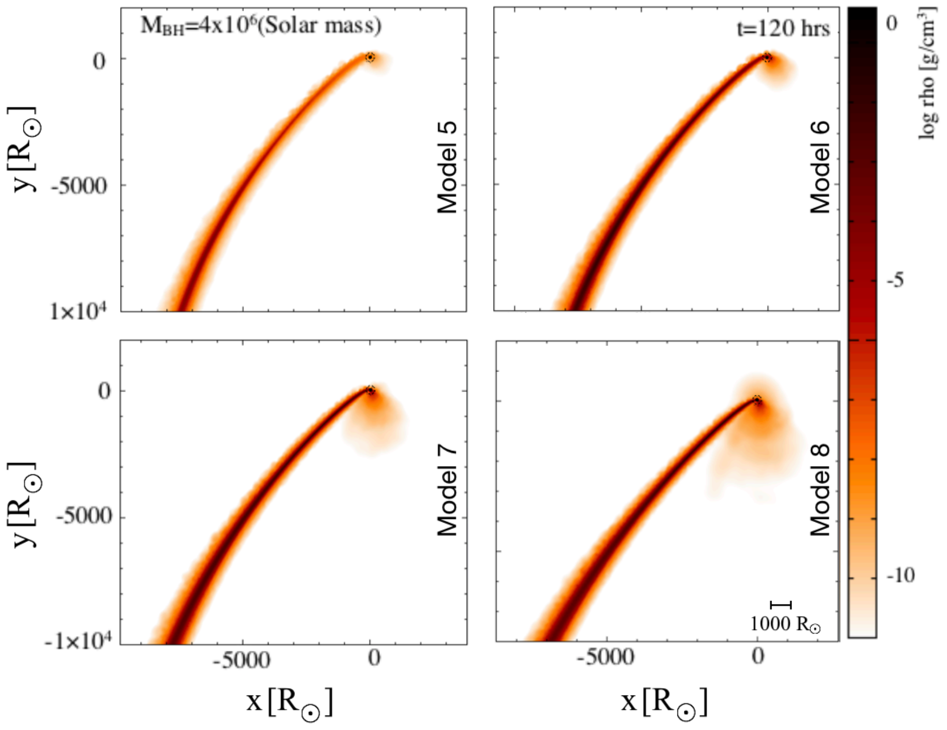

Figure 4.5: Snapshots of the evolution of the spatial distribution of the debris at $t = 120$ hrs.

The star's centre of mass still follows parabolic trajectories with the material on the far tail (the one on the opposite side of the black hole) being unbound and ejected as the material on the near tail (the one closer to the black hole) will be gravitationally pulled onto the compact object.

The tidal field of a 10^6 M$_\odot$ black hole is $\approx 3\%$ asymmetric on the scale of the star at R_T, as asymmetry scales with b (Eastwood and Khochfar 2018). The formation of two similar tidal tails is the reflex of the symmetry (as in Figure 4.4, top panels), which is consistent with those resulting from disruptions of main sequence (MS) stars (Guillochon and Ramirez-Ruiz 2013). MS stars (and so solar type stars) posess cores that are denser than their envelopes and the ratio of the central to average density is $\rho_{core}/\bar{\rho}_* \approx 100$ as the $\rho_{core} \simeq 150$ g cm^{-3} and the $\bar{\rho}_* = 1.6$ g cm^{-3}.

The material of the core is perturbed much later than that of the envelope because the dynamical time of the core is much smaller compared to the envelope dynamical time. For low b encounters the material of the core is not perturbed or is perturbed a few but the gravitational influence on it changes the arrangement of the surrounding envelope material as the encounter evolves. For polytropes like the ones used in this simulations, the adiabatic response is the contraction as mass is removed (Hjellming and Webbink 1987). The tidal force at R_P increases with b and removes a significant fraction of the stellar envelope mass.

The rate of mass loss is halted when the total envelope mass that remains on the stellar structure is similar to the mass of the core. As the core represents a significant amount of mass of the total mass of the star, the stellar structure responds to the loss of mass by contracting (Rees 1988; Guillochon et al. 2014a). During the encounters, the mass loss asymptotes values less then the mass envelope M_{env} (Figure 4.6), where $-\Delta M$ represents the mass loss as a function of b. With an increasing b the tidal mass removal makes the mass envelope to contract more and as a consequence the steepening of the penetration parameter leads to the asymptotic behaviour of the mass loss $-\Delta M$ (Figure 4.6).

The contraction of the mass envelope develops regarding the expansion of the fluid trajectories on the frame of the black hole potential and the resisting core due to the enclosed mass that holds after R_P. This enclosed mass shows that the envelope is contracting and so its mass increases (Figure 4.7). The enclosed mass in terms of the Hill radius can be obtained by the Hill radius of the stellar core as a function of time by (Guillochon and Ramirez-Ruiz 2015; Guillochon et al. 2016)

$$R_{h,core}(t) = \left(\frac{M_*}{M_{BH}}\right)^{1/3} r(t) \tag{4.3}$$

with $r(t)$ being the distance between the stellar core and the black hole . The enclosed mass M_{enc} reaches its minimum value at R_P where $R_{h,core} = b^{-1}(M_*/M_{BH})^{1/3}R_*$ (Guillochon and Ramirez-Ruiz 2015) and increase after the passage at R_P due to the contraction of the envelope material in terms of the expanding frame of the stellar disruption (Figure 4.6).

The debris resultant from disruption, which corresponds to the mass loss from the star to the black hole, will return to R_P in a fallback rate that represents the peak fallback rate of the material. Thus as the peak fall back rate $\dot{M}$ needs many dynamical times and the simulations performed have a time scale of hours regarding the disruption moment, the amount of accreted mass is quantified by the mass accretion rate (Figure 4.8) that follows the $t^{-5/3}$ predicted for the peak fallback rate (Guillochon and Ramirez-Ruiz 2013). In Table 4.3 the amount of material stripped from the star as a function of b is presented.

The net mass loss $-\Delta M$ as a fraction of the envelope mass M_{env} for the $b = 0.5$ encounter is only $\approx$ 6% of the total mass of the envelope. For the $b = 1$ encounter the mass loss increases by a factor of ≈ 3 compared to the previous encounter, stripping about 16% of the stellar mass of the envelope.

For the deeper encounters of $b \geq 2$ the net mass loss can increase to more then half of the envelope mass, as for the encounters with $b = 5$, $b = 6$, $b = 7$ and $b = 8$ as in the last case the stripped material can go up to more than 60% of the mass of the stellar envelope. The amount of mass loss with b is expected to increase with time, as more mass will be depletted from the stellar surface onto the black hole.

The fallback mass rate is shown in Figure 4.8. After the pericentre passage the bound debris that contributes to the fallback mass will move on ballistic trajectories that will send it far from the black hole

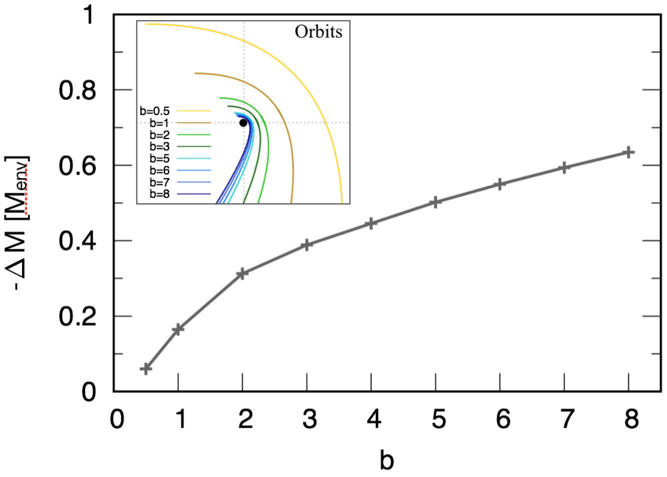

Figure 4.6: The net mass loss ($-\Delta M$) as a fraction of the mass envelope (M_{env}) with increasing b after the first passage at pericentre, for the parabolic TDEs. The respective orbits of b are shown on the inset on the top left corner of the figure.

Model	b	$-\Delta M[M_{env}]$
1	0.5	$5.987401321 \times 10^{-2}$
2	1	$1.644928701 \times 10^{-1}$
3	2	$3.124796697 \times 10^{-1}$
4	3	$3.888414118 \times 10^{-1}$
5	5	$5.020154706 \times 10^{-1}$
6	6	$5.499332193 \times 10^{-1}$
7	7	$5.939326339 \times 10^{-1}$
8	8	$6.348241402 \times 10^{-1}$

Table 4.3: Quantified stripped material as a function of the penetration parameter after the first periapsis passage for the parabolic TDEs.

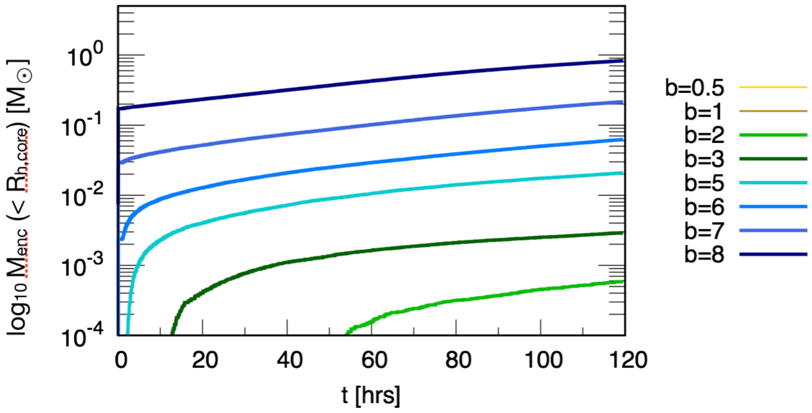

Figure 4.7: The adiabatic response of the stellar envelope to the loss mass is to contract becoming more dense and shielding it self from more loss of mass.

until it no longer resists to the gravitational pull and starts to fallback. After the passage at R_P the stream debris produced in all models converge to a similar regime of accretion onto the black hole, as can be observed by the evolution of accretion of the debris in time. In both panels of Figure 4.8 it can be observed the evolution of the fallback rate of the material that is accreted onto the black hole, which are related to the passage of the star at R_P. To each increasing b the distance of R_P to R_S decreases and all the effects related to this proximity are amplified which causes the accretion regime of the fallback material to vary for each case. In the left panel, the cases for the shorter penetration parameters are shown.

The trajectories of the star in these cases have a wider range as the respective b's are less penetrating which causes the bound material to be spreaded in a larger area. In the right panel, the same regime of the fallback rate can be observed. In these cases the penetration parameters are higher which sets the star's trajectories to shorter distances to R_S and by consequence the accretion of the material increases. Approximately after 12 hours the fallback rate increases, meaning that there is a faster return of the material to the black hole.

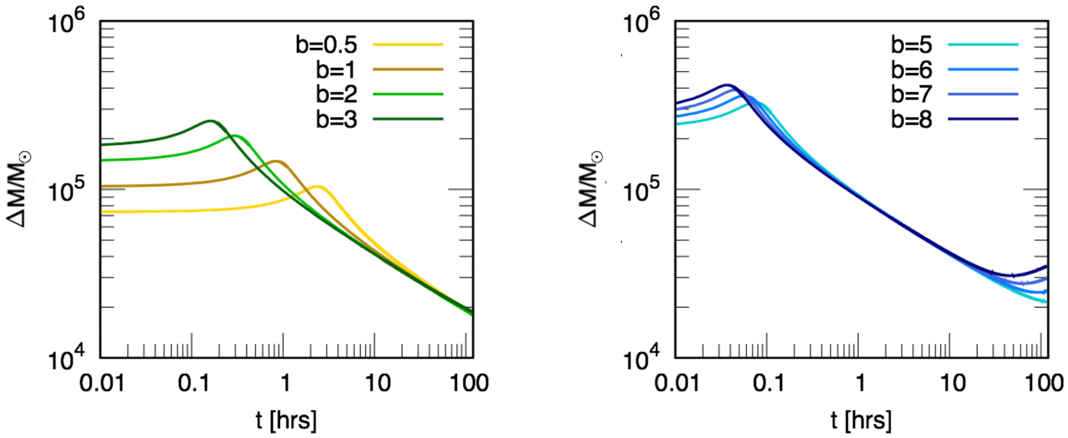

Figure 4.8: The mass accretion rate for the models 1, 2, 3 and 4 on the left panel and for models 5, 6, 7, and 8 on the right panel.

The peak of the fallback rate $\dot{M}_{fb}$ occurs when the stellar mass reaches $\sim M_*/2$ which will occur in the fallback time interval, as $t \geq P_*$. In parabolic TDEs the P_* is related to the fraction of the most bound stellar debris, as the rest of the material is ejected in hyperbolic orbits and will not return to R_P. The evolution of the stellar debris at the dynamic balance of the star and the black hole reflect the passage at pericenter which evolve through a short timescale, as the star continuous to be depleted of mass that plunges the short potential barrier between the star and the black hole.

The spread in energy can be traced to a return to R_P for the bound material to the black hole through (2.25) which implies that the fallback rate decay law is dependent of the energy distribution dM/dE (Rees 1988). If the energy distribution is flat then dM/dE is independent of E and the mass fallback rate will decay as $\dot{M} \propto t^{-5/3}$ as shown in Figure 4.9.

The evolution of the specific binding energy of the stellar fluid elements relative to the black hole can trace the bound debris of the star, which gives the spread of mass per unit energy dM/dE where E is the specific orbital energy relative to the black hole. The bound debris is shown in Figure 4.9, where the specific binding energy is plotted in the x axis. The return of the debris to the black hole will be characterized by the peak of the mass fallback rate that can be obtained from (2.24) and (2.26). The fallback time given by (2.24) is related to a $M_{BH} = 10^6 M_\odot$.

The Milky Way's SMBH is $\approx 4 \times 10^6 M_\odot$ which gives a fallback time of $t_{fb} = 7.077 \times 10^6$ s $\approx$ 82 days. From (2.26) the estimated peak of the fallback mass rate is $\dot{M} \simeq 3 M_\odot$ yr^{-1}, which is in close agreement with the $\dot{M} \simeq 3.3 M_\odot$ yr^{-1} from Evans and Kochanek (1989).

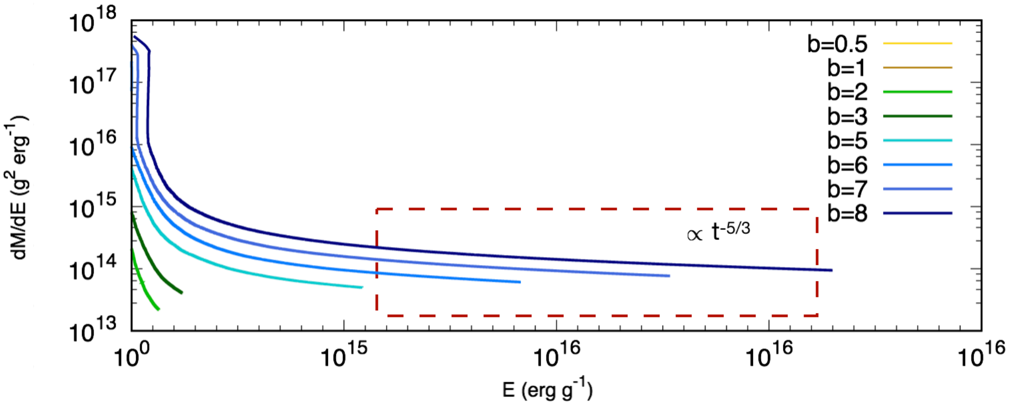

Figure 4.9: Spread of the bound debris per unit mass of the star as a function of the specific orbital energy relative to the black hole.

4.3 Elliptic TDEs

As for the parabolic TDEs, a set of nine elliptic TDEs were performed, involving a solar type star with the same characteristics of mass and size (i.e. $M_* = 1M_\odot; R_* = 1R_\odot$) which is inbound onto the SMBH Sgr A* (with $M_{BH} = 4 \times 10^6 M_\odot$ and tidal radius $R_T = 159R_\odot$) in elliptical orbit, at the center of the Milky Way.

4.3.1 Setup and initial conditions

In this set of simulations the star is placed at r_0 defining an elliptical orbit which passes by the apocenter of the trajectory. In order to simplify the initial moment of the simulations, r_0 was set to equal the semi-major axis (a_*; 2.21) of the stellar orbit which defines the starting point. As these simulations have elliptical orbits, the trajectory of the star is also defined by its eccentricity (ecc), which was fixed for all the penetration parameters as $ecc = 0.3$. The setup parameters for this set of simulations consider also the orbital period P_* (2.22) of the star and are shown in Table 4.4.

Model	b	$a_*[R_\odot]$	P_* [hrs]	$R_P[R_\odot]$
9	0.5	4.535×10^2	13.43	3.175×10^2
10	1	2.268×10^2	4.75	1.587×10^2
11	2	1.134×10^2	1.68	7.937×10^1
12	3	7.559×10^1	0.914	5.291×10^1
13	4	5.669×10^1	0.593	3.969×10^1
14	5	4.535×10^1	0.425	3.175×10^1
14	6	3.780×10^1	0.323	2.646×10^1
15	7	3.240×10^1	0.256	2.268×10^1
16	8	2.835×10^1	0.209	1.984×10^1

Table 4.4: Simulation parameters for each model of the elliptic TDEs.

In Figure 4.10 a schematic of the complexity of an elliptical TDE is shown. The passage of a $1M_\odot$ type star whose orbit has an eccentricity of 0.3 by the SMBH shows the evolution of the deformation that the star suffers due to tidal forces from the central black hole. The trajectory of the star is represented by the dashed black line and its direction is given by the dashed black arrow. The SMBH is located at (0,0) represented by the black circle and the tidal radius R_T is represented by the grey dotted circle around the black hole. The stretching of the star is clear after two hours and increases as the star completes its orbital trajectory.

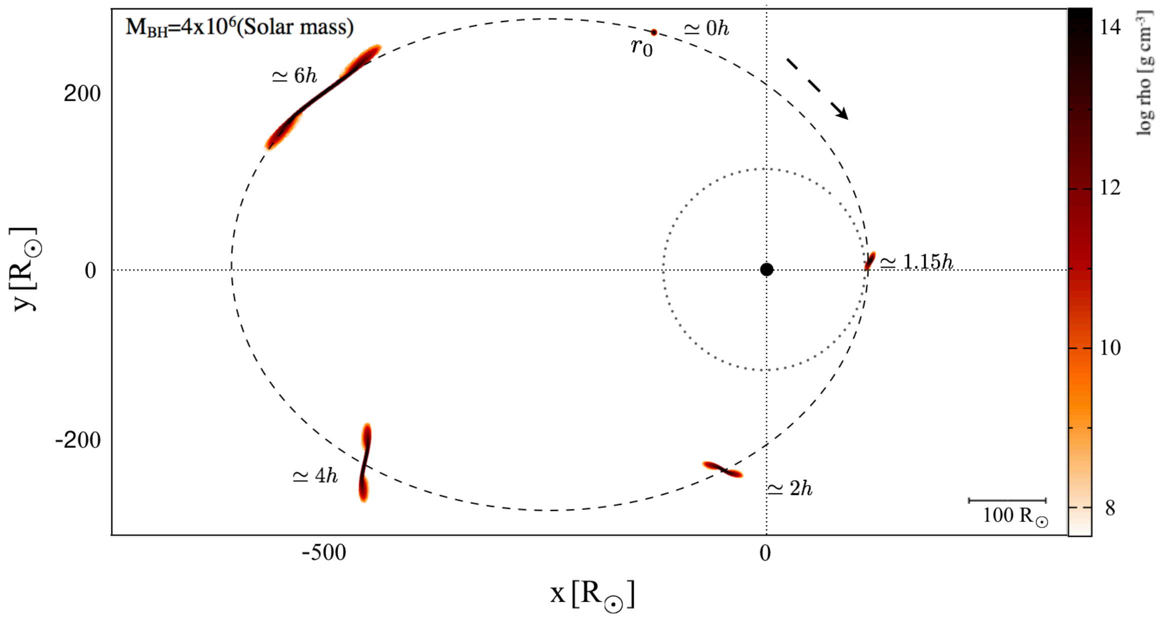

Figure 4.10: Time evolution of a star and its debris with an elliptical orbit around the SMBH.

Figure 4.11 represents the initial setup model for the simulations. The computational domain is defined in physical units of solar radius $1R_\odot = 6.957 \times 10^{10}$ cm and time comes in hours (top right corner). The scale of the computational domain and the mass of the black hole are shown in the bottom right and top left corners, respectively.

Analogously for the parabolic TDEs the tidal disruption process is simulated by placing the star in orbit by the gravitational field of influence of the black hole, which is modeled by an external potential Φ (defined previously in 4.2.1) with an accretion radius given by R_S (also defined in 4.2.1).

4.3.2 Results

In this section the results obtained from the simulations of elliptic TDEs are presented. The simulations are presented in terms of the orbital periods, due to their elliptical nature and are evolved through $t = 20P_*$, though the major effects on the stellar structure occur immediately after the passage at R_P and a few orbital periods next. The thermal energy release is plotted for $t = 5P_*$.

4.3.2.1 Spatial distribution of the debris after R_P

The spatial distribution of the debris for the elliptic TDEs can also be described in terms of the stellar envelope material that is sheared from the stellar surface due to the gravitational torque applied by the tidal forces of the black hole. There is also in the elliptical tidal disruption a portion of the stellar material that becomes unbound from the star and is ejected forming two tidal tails (Tejeda et al. 2017). The different penetration parameters imply different pericenter distances, which causes the fluid to shift to different configurations for each event .

In Figure 4.12 the simulations for each model show the deformation that the star suffers after the first orbital period $P_* = 1$. The more grazing penetration parameters of models 9 and 10, respectively $b = 0.5$ and $b = 1$ have a less deformation in respect to the rest of the models (with $b \geq 2$). The deformation of the star in model 9 shows clearly the formation of two tidal tails, where the less bound material is forcefully

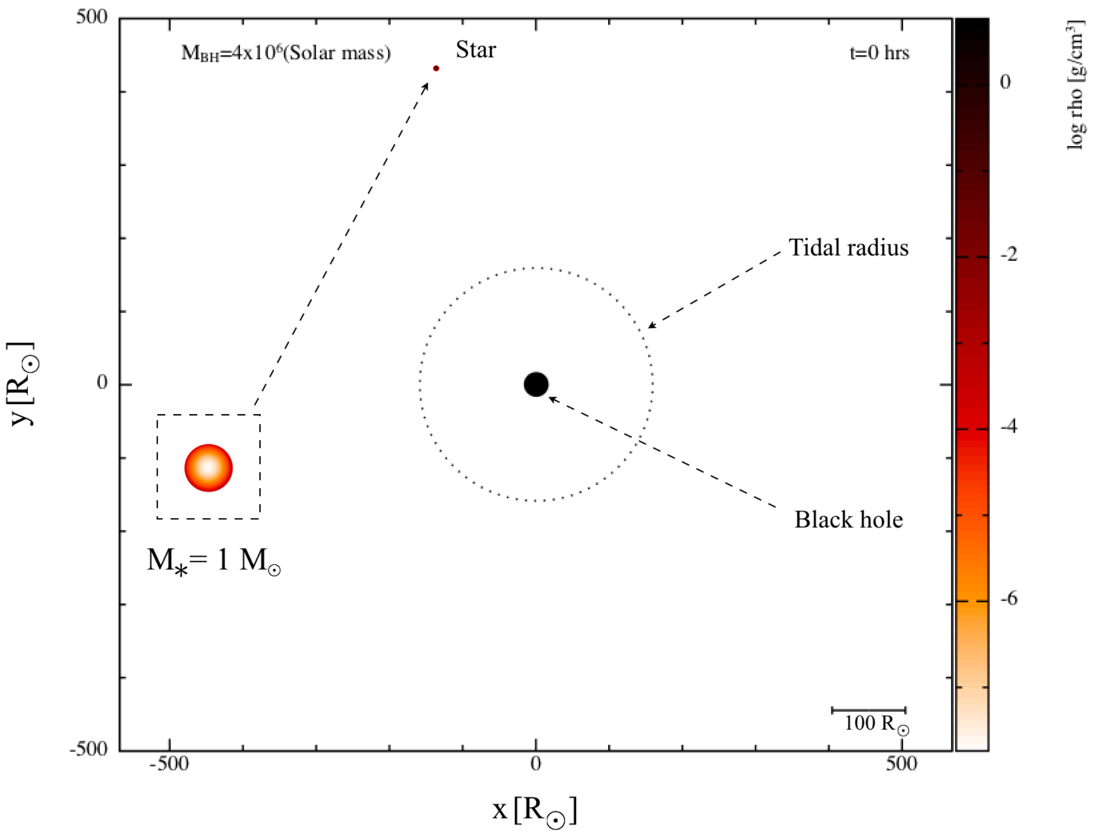

Figure 4.11: Initial configuration of the elliptic simulations with the star and black hole locations.

ejected from the stellar surface. In model 10 it is still possible to observe the stretch due to the tidal forces of the SMBH. The rest of the models which have penetration parameters of $b \geq 2$ (models 11 to 17) produce more pronounced deformations.

As the penetration parameter increases, it can be observed that the debris resultant from the disruption process describes near circular orbits (with an eccentricity of $ecc = 0.3$). Also the elliptic TDEs are characterized by the pancake phase, which is the limit that separates the star from suffering deformation when its penetration parameter is $b > 2$.

Higher values of b imply an effective disruption of the stellar core that is progressively stretched and the less bound material of the star (the stellar envelope) starts to suffer accretion onto the black hole. The TDEs with $b \geq 3$ are less frequent to occur than the grazing ones, though still represent an important amount of TDEs, which are accounted to be $\approx 33\%$ (Luminet and Barbuy 1990).

When the star crosses R_P deep inside the R_T its material is ballistically accelerated and the star is compressed into two orbital planes that intersect each other at R_P and the star is deformed into the pancake shape. The star experiences a strong vertical collapse at R_P and acquires a collapse velocity v_c defined by (4.10). Again, the strong vertical compression suffered by the star results in shocks and the kinetic energy is converted into thermal energy due to the shocks that increase the temperature of the stellar core (Luminet and Barbuy 1990). The generalized equation (4.10) for the collapse velocity is applied to both cases, parabolic and elliptic orbits, which generically have the same velocity of collapse for the star.

The elliptic TDEs have specific circularization energy ε_{circ}, which is given by (Bonnerot et al. 2016)

$$E_{circ} = -\frac{GM_{BH}}{2R_{circ}} \tag{4.4}$$

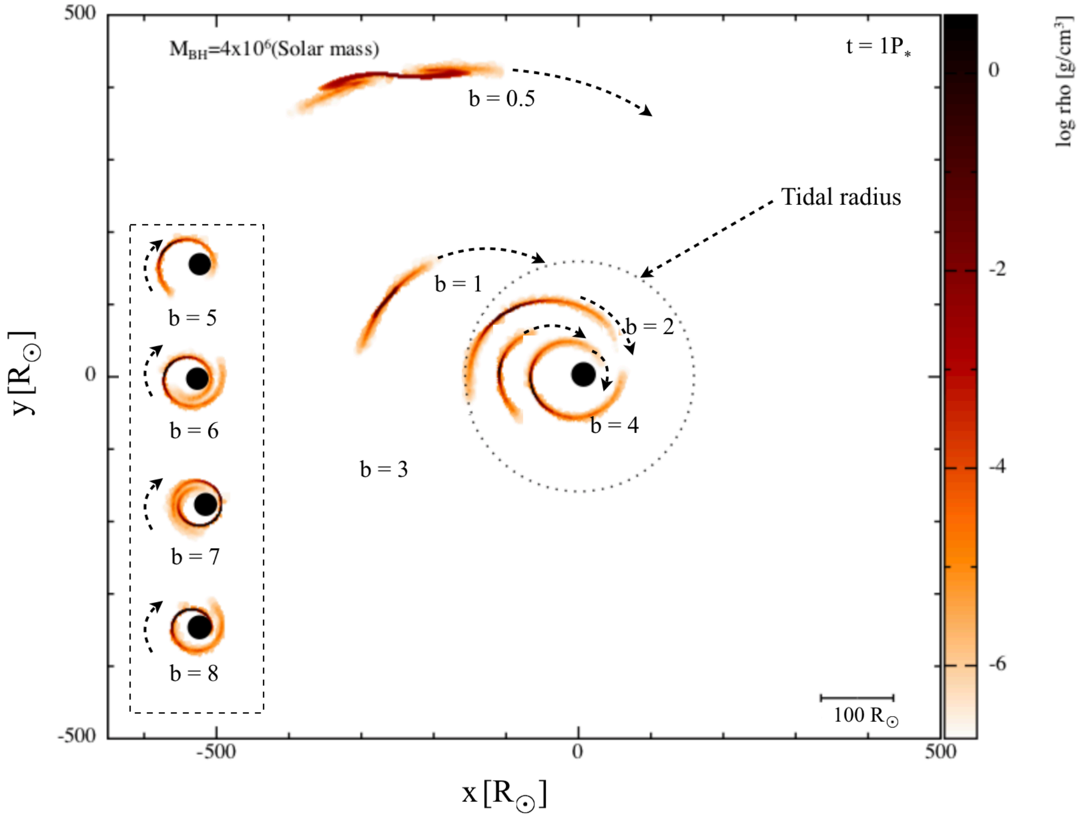

Figure 4.12: Spatial distribution of the debris for the models of the elliptic TDEs at the first orbital period t=1 P_*, as a function of the penetration parameter b.

and results in a ring of debris that forms outside the circularization radius (R_{circ}) (Bonnerot et al. 2016)

$$R_{circ} = (1 + ecc)R_P. \tag{4.5}$$

The kinetic energy (E_{kin}) of the star is therefore converted into thermal energy (E_{th}) during its passage at R_P. The net effect of the several passages of the debris at R_P is the reduction of the kinetic energy and its conversion into thermal energy. In Figure 4.13 the circularization radius (left panel) as a function of the penetration parameter is shown.

The debris resultant from the disruption process stays bound to the black hole at the distance where the loss of angular momentum is not enough for the debris to be accreted. This debris acquires an excess of angular momentum which allows it to settle in a near circular orbit, where the minimum distance is defined by the circularization radius (Bonnerot et al. 2016). The specific circularization energy (in the right panel) results from the redistribution of the angular momentum of the debris that settles around the SMBH as described above.

4.3.2.2 Mass removal

As the tidal force at R_P grows with increasing b, the adiabatic response of the star to those forces is to contract, while a considerable amount of mass is removed from the stellar envelope. When the remainder mass of the stellar envelope that wasn't removed equals the mass of the core, there is a *cut-off* in the rate of the mass loss. The stellar structure response to such mass loss is to contract (Rees 1988; Guillochon et al. 2014a), as described previously. The mass loss $-\Delta M$ was obtained as a function of the penetration parameter b (see Figure 4.14 and its quantified values in Table 4.5).

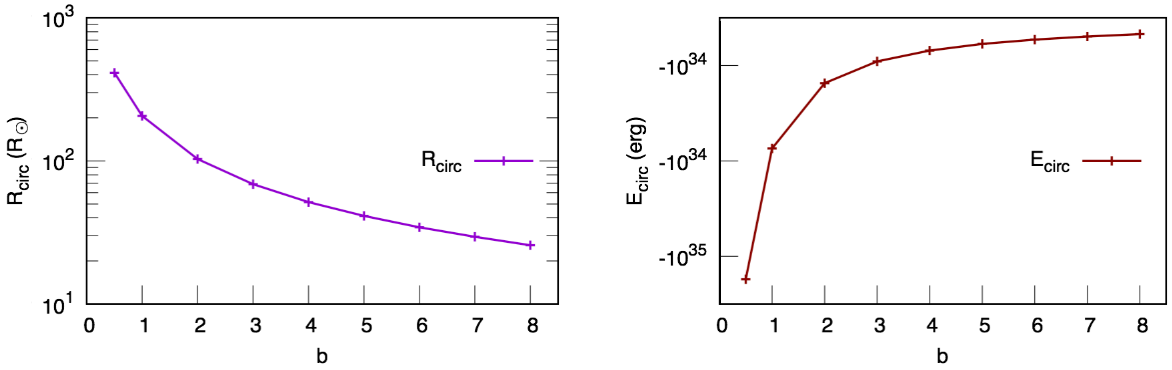

Figure 4.13: The circularization radius (R_{circ}; left panel) and the circularization energy (E_{circ}; right panel) as a function of the penetration parameter b.

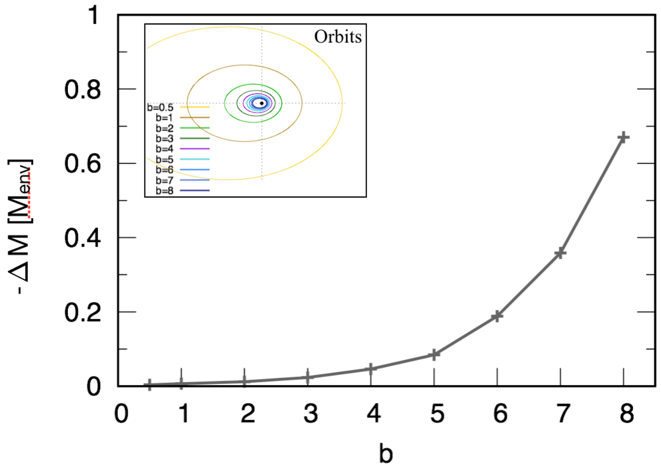

Figure 4.14: The net mass loss ($-\Delta M$) as a fraction of the mass envelope (M_{env}) with increasing b after the first passage at pericentre, for the elliptic TDEs. The respective orbits of b are shown on the inset on the top left corner of the figure. The blue line represents the linear fit to the relation $-\Delta M = f(b)$.

The enclosed mass (M_{enc}) that remains after R_P results from the contraction of the mass envelope regarding the resisting core. By the passage of the star at pericenter, the M_{enc} reaches its minimum with a Hill radius of the stellar core ($R_{h,core} = b^{-1}(M_*/M_{BH})^{1/3}R_*$; (Guillochon and Ramirez-Ruiz 2015; Guillochon et al. 2016)) which will increase after pericenter because the envelope material contracts (Figure 4.15). The net mass loss in the grazing encounters of model 9 ($b = 0.5$) and model 10 ($b = 1$) is respectively $\sim 3.6\%$ and $\sim 6\%$, which is about twice the amount of mass loss of model 10 in relation to model 9 (and also their respective distances to R_P). The deeper encounters have mass losses of $\sim 10\%$, $\sim 13\%$ and $\sim 18\%$ for the models 11 ($b = 2$), 12 ($b = 3$) and 13 ($b = 4$). The models 14 ($b = 5$) and 15 ($b = 6$) have $\sim 23\%$ and $\sim 28\%$ of mass loss and finally the deepest encounters of models 16 ($b = 7$) and 17 ($b = 8$) have mass losses of $\sim 40\%$ and $\sim 58\%$.

4.4 Tidal energy transfer

The energy required to tidally deform or disrupt a star, i.e., the energy needed to overwhelm the stellar binding energy, reduces the energy of its orbit such that the star's kinetic energy will decrease. When the star is crossing at R_T its orbital kinetic energy is of the order of $(M_{BH}/M_*)^{2/3}$ (Rees 1988). If a star

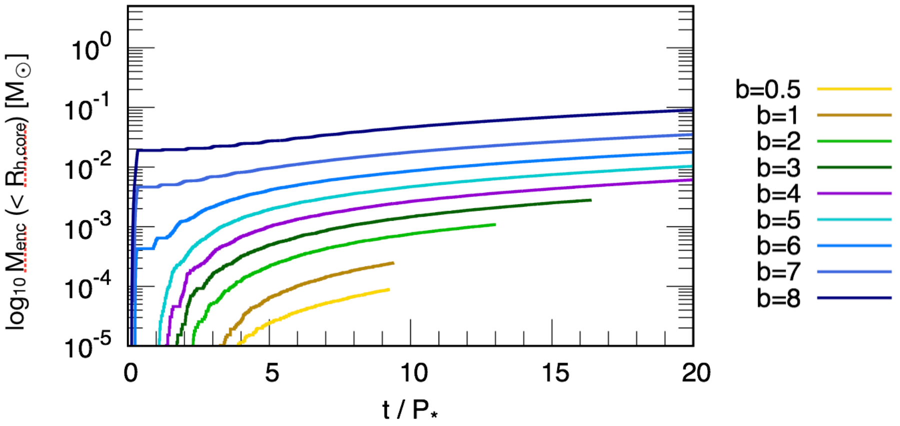

Figure 4.15: The stellar envelope reacts adiabatically to the loss mass by contracting becoming more dense and shielding it self from more loss of mass.

Model	b	$-\Delta M[M_{env}]$
9	0.5	$3.650597278 \times 10^{-3}$
10	1	$6.489950717 \times 10^{-3}$
11	2	$1.176303567 \times 10^{-2}$
12	3	$2.312044943 \times 10^{-2}$
13	4	$4.603808790 \times 10^{-2}$
14	5	$8.416654836 \times 10^{-2}$
15	6	$1.882085708 \times 10^{-1}$
16	7	$3.587725881 \times 10^{-1}$
17	8	$6.702636540 \times 10^{-1}$

Table 4.5: Quantified stripped material as a function of the penetration parameter after the first periapsis passage for the elliptic TDEs.

approaches the black hole at a distance shorter than the lowest marginally bound orbit then it will inevitably fall onto the black hole (Kozlowski et al. 1978). The tidal disruption event of a star by the black hole should release a certain amount of energy resultant from its initial formation. The energy of a polytropic star can be estimated by the Chandrasekhar expression for polytropes Chandrasekhar (1967) which is of the order of $\approx 5.8 \times 10^{48}$ erg $(M_*/M_\odot)^2(R_*/R_\odot)$. The polytropic star used in these simulations has an energy of $\approx 2.042 \times 10^{48}$ erg.

The SMBH that resides at the center of the Milky Way with an estimated mass of $M_{BH} \sim 4 \times 10^6 M_\odot$ dominates the gravitational potential in the inner 0.1 pc of the GC (Ayal et al. 2000; Strubbe and Quataert 2009; Cheng et al. 2011). Considering a typical solar type star that approaches the SMBH, whose mass is $M_{BH} \gg M_*$, it will reach R_P with an estimated orbital velocity at pericentre defined by

$$V_p = \left(\frac{2GM_{BH}}{R_P}\right)^{1/2} = v_* \left(\frac{M_{BH}}{M_*}\right)^{1/2} \left(\frac{R_*}{R_P}\right)^{1/2} \tag{4.6}$$

and $v_* \equiv (2GM_*/R_*)^{1/2}$ represents the escape velocity at the stellar surface. The tidal force exerted by the SMBH on the star at R_P is

$$F \simeq \frac{GM_{BH}}{R_P^3} R_* = a_* \left(\frac{M_{BH}}{M_*}\right) \left(\frac{R_*}{R_P}\right)^3 \tag{4.7}$$

where the acceleration from the self-gravity of the star is given by $a_* = GM_*/R_*^2$ (Khokhlov and Melia 1996) . Assuming that the star's compression begins when the tidal force of the star is similar to its self-graviy acceleration, it means that it occurs at a distance to the black hole of $R \simeq R_*(M_{BH}/M_*)^{1/3} > R_P$. The star will reach R_P at the time $t \simeq a_*(M_{BH}/M_*)^{1/2} \simeq R_*/v_*$. The total velocity of the star is given by

$$v_{tot} = \sqrt{2}v_* \left(\frac{R_*}{R_P}\right)\left(\frac{M_{BH}}{M_*}\right)^{1/2}. \tag{4.8}$$

The velocity of the star and the tidal force per unit mass at R_P that the SMBH exerts on the star during its pericenter passage were determined. The escape velocity at the stellar surface is $v_* = 6.177 \times 10^7$ cm s^{-1}. In Table 4.6 the values for the velocity of the star and the tidal force were obtained by the equations (4.6) and (4.7).

The cases where the star passes at R_P deep inside the R_T ($R_P < R_T$), the stellar matter moves ballistically resulting in a compression of the star in two orbital planes which intersect near R_P and the star is continuously compressed until it acquires a pancake like shape. For the larger penetration parameters the angle α between the two planes can be defined by

$$\alpha \approx \frac{R_*}{R_T sin\theta_t} \tag{4.9}$$

where θ_t is the true anomaly suffered by the star at R_T and since the star is moving on a parabolic trajectory $cos\theta_t = 2R_P/R_T - 1$ giving $sin\theta_t \approx (R_P/R_T)^{1/2}$ and $\alpha \approx R_*/(R_P R_T)^{1/2}$. The strong vertical collapse that the star suffers at R_P is given by its velocity collapse v_c which is defined by the star's velocity at pericentre V_p and the angle α defined in respect with the orbital planes, which is roughly $v_c \approx v_p\alpha$. The velocity of collapse of the star is therefore

$$v_c \approx b\left(\frac{GM_*}{R_*}\right)^{1/2} \tag{4.10}$$

and the resulting strong vertical compression of the star results in shocks that can convert the kinetic energy into heat (thermal energy) which produces an increase in the temperature of the stellar core $T_c \approx b^2 T_*$ (Luminet and Barbuy 1990; Guillochon et al. 2014b). The collapse velocity for the star in each model is quantified in Table 4.6. From this table is possible to establish a relation between the orbital velocities at pericentre V_P and the penetration parameters b of the respective models.

The velocities increase as each encounter occurs more deeply inside R_T. The grazing encounters with $b = 0.5$ and $b = 1$ have an increase of the initial velocity of the star $v_* = 6.177 \times 10^7$ at its apoapsis to about two orders of magnitude $\sim 10^9$ cm s^{-1}. As for the encounters with $b \geq 2$ the star attains velocities up to three orders of magnitude $\sim 10^{10}$ cm s^{-1} higher than its initial velocity, due to the accelerations produced over the star by the passage inside R_T, with R_P distances shorter at each increasing b.

As the star reaches R_P the tidal forces from the black hole exert a growing effect of deformation on the stellar surface that can lead to partial or complete disruption of the star. In the encounters with $b = 0.5$ and $b = 1$ (the most grazing ones) the tidal forces applied on the star are of the order of $\sim 10^3 - 10^4$ N g^{-1}, respectively. For the enccounters that occur deep inside R_T, the tidal forces scale up to four orders of magnitude higher than the first encounter, due to the shorter distance of the star to the black hole. The deep encounters $b \geq 5$ will produce a complete disruption of the star (Guillochon et al. 2014a).

In Figure 4.16 are plotted the orbital velocities at pericenter and the velocities of collapse of the star for both cases (parabolic and elliptic). As both velocities are plotted as a function of the penetration parameter b, it can be observed that the increase of V_c can be due the strong vertical collapse that the star suffers at R_P.

The velocity at pericentre and the angle formed by the orbital planes result in a strong vertical compression of the star which is also a function of the tidal forces of the black hole. The orbital velocity at

Models	b	V_P [cm s^{-1}]	F_{tidal} [N g^{-1}]	V_c [cm s^{-1}]
1, 9	0.5	6.933×10^9	2.742×10^3	2.184×10^7
2, 10	1	9.805×10^9	3.428×10^4	4.368×10^7
3, 11	2	1.387×10^{10}	2.194×10^5	8.735×10^7
4, 12	3	1.698×10^{10}	7.404×10^5	1.310×10^8
13	4	1.961×10^{10}	1.754×10^6	1.747×10^8
5, 14	5	2.193×10^{10}	3.428×10^6	2.184×10^8
6, 15	6	2.402×10^{10}	5.923×10^6	2.621×10^8
7, 16	7	2.594×10^{10}	9.405×10^6	3.057×10^8
8, 17	8	2.773×10^{10}	1.404×10^7	3.494×10^8

Table 4.6: Quantified values for the orbital velocity of the star V_P and the tidal force F_{tidal} exerted on the star by the black hole at pericenter.

pericentre V_P is also a function of the tidal forces and in this case it has a more asymptotic increase as the tidal forces are higher. It can be due to the penetration of the star deep inside R_T (with higher b), where the effects of the tidal forces are highly amplified.

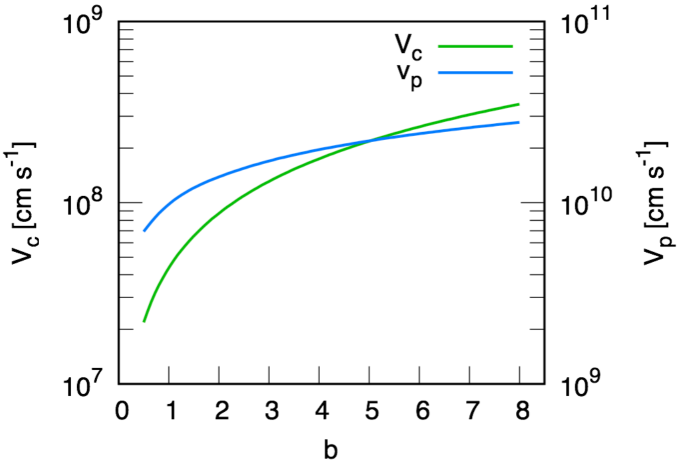

Figure 4.16: Evolution of the orbital velocity (green line) of the star and its velocity of collapse (blue line) as it passes at pericenter as a function of the penetration parameter b.

When the star approaches the SMBH with a certain kinetic energy it starts to experience the distortion and compression due to tidal forces. During the passage at pericentre it suffers maximum compression and deformation and there will be a release of thermal energy that is imparted to the resultant debris at the expense of the kinetic energy. On the other hand, the thermal energy will decrease after R_P due to the expansion of the stream. About 10% of the thermal energy due to the shock is radiated, while the majority is converted into expansion kinetic energy (Jiang et al. 2016).

The thermal energy release is shown in figures 4.17 and 4.19. The left panel of Figure 4.17 is related to models 1 and 2 which represent the lower penetration parameters. Model 1 ($b = 0.5$) does not release significant energy after the passage at pericentre. This is the consequence of the passage of the star at $2R_T$ which causes the star to suffer minor effects from the tidal forces of the black hole. The star, nevertheless, is perturbed and though disruption does not occur, the resulting effects on the star are the formation of two tidal tails that start to elongate as it gets further away from the black hole, though the stellar core is completely preserved. Model 2 has a penetration parameter of $b = 1$ and is still considered a grazing encounter as its trajectory brings the star at the same distance of the tidal radius R_T (with $b = 1$ it implies that $R_T = R_P$) and so $b \equiv 159 R_\odot \equiv 1 R_T$. In this case a certain amount of thermal energy is released about the same order of magnitude of that of the star $\sim 10^{48}$ erg.

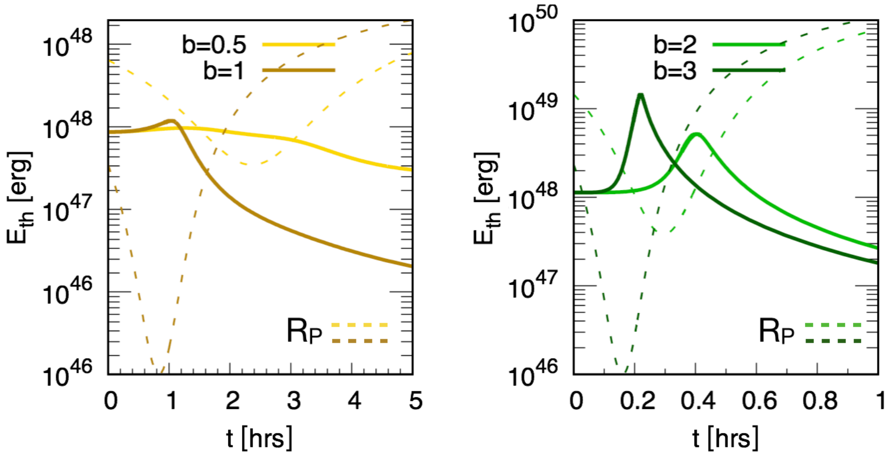

Figure 4.17: Thermal energy released by the star at the passage at R_P for models 1, 2, 3 and 4. The dashed lines represent the trajectory of the star whith R_P corresponding to the lower point of the trajectory.

The effects are more pronounced as the tidal tails that formed after R_P are more elongated and present a bigger deformation at $t = 120$ hrs, as can be seen from Figure 4.4. In the right panel of Figure 4.17 the models 3 and 4 ($b = 2$ and $b = 3$ respectively), have their pericentres inside the tidal radius and the effects from tidal forces of the black hole on the stellar structure results in the disruption of the star in both models. The release of energy due to this passage is higher in model 4 as it passes the black hole with shorter R_P and the amount of energy scales to one order of magnitude of that of the star.

The passage at pericentre is characterized also by the decrease in angular momentum of the star as it falls inwards to the black hole. It can be observed from Figure 4.18 that the lowest values of angular momentum in each case correspond to the respective R_P's. A comparison with the results of Figure 4.17 shows that the thermal energy release occurs after the passage of the star at R_P.

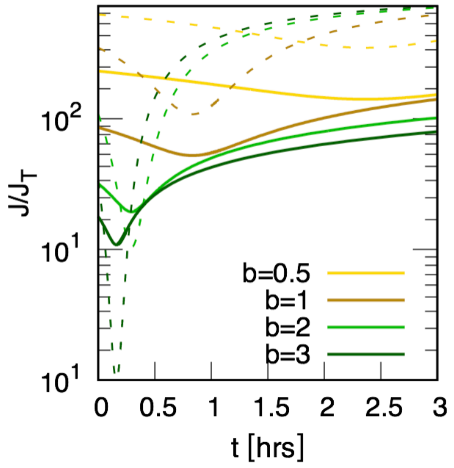

Figure 4.18: Specific angular momentum for models 1, 2, 3 and 4.

Models 5 and 6 are represented in the left panel of Figure 4.19. With increasing b the distance at which the star passes at R_P is much shorter then the previous cases, which means that the effects of the tidal forces exerted on the stellar structure are much more amplified and the result is the complete destruction of the star (Guillochon et al. 2014a). The distances at R_P for models 5 and 6, are of $\sim 31 R_\odot$ and

$\sim 26.5R_\odot$ respectively and the tidal forces are $\sim$ 2 to 3 orders of magnitude higher then in the previous cases. By $t = 120$ hrs a long stream of stellar debris has formed and the material is accreted in a steady state regime defined by the mass fallback rate. The same scenario occurs for the models 7 and 8 with $b = 7$ and $b = 8$, respectively. The extreme penetration parameters that define these two simulations have a pericentre distance much closer to the black hole than any other case. In fact, for model 8 the distance the distance to the black hole is very near of the Schwarschild radius which is $R_S = 17R_\odot$ (see Table 4.2).

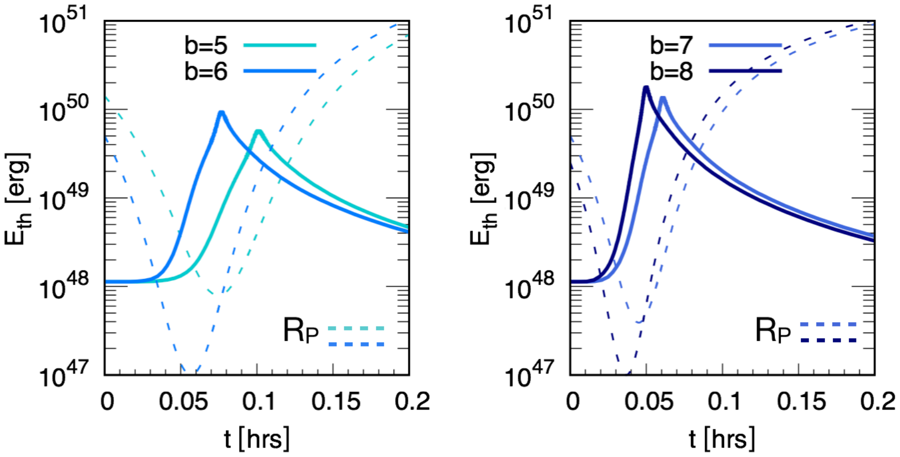

Figure 4.19: Thermal energy released by the star at the passage at R_P for models 5, 6, 7, and 8. The dashed lines represent the trajectory of the star whith R_P corresponding to the lower point of the trajectory.

At this close distance to R_S the tidal forces are high enough to strip away a considerable amount of the envelope mass of the star, in fact in this case more than 50% of the stellar mass envelope is removed by the passage of the star at R_P with a release of thermal energy after the R_P passage of the order of $\sim 10^{50}$ erg. At $t = 120$ hrs there is a considerable amount of gas around the black hole that will stay bound to it as it loses its angular momentum.

If tidal torque is exerted over the gas around the black hole it will gradually spiral inward on a dissipation timescale. This gas will have a gravitational binding energy onto the SMBH that will be converted into thermal energy until it reaches the last stable orbit around the black hole, that corresponds roughly to $3R_S$ considering the Schwarschild black hole Rees (1988); Alexander (2005). In Figure 4.20 the evolution of the

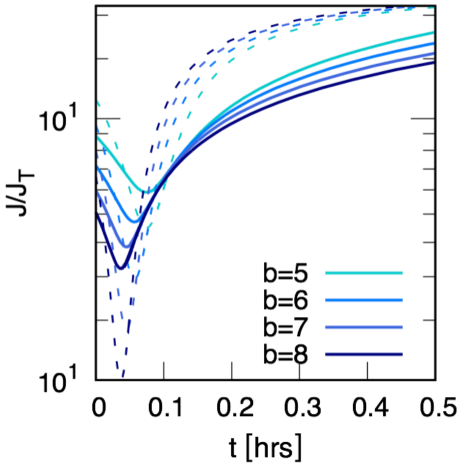

Figure 4.20: Specific angular momentum for models 5, 6, 7 and 8.

specific angular momentum of the star at each passage by R_P is shown. In Figures 4.17 and 4.19 the peaks of the thermal energy that are observed are related to the release of such energy after the passage of the star at R_P. In fact these figures show that the release of energy takes place immediately after the pericentre passage, as the R_P's are given by the lowest values of the potencial energy of the star (represented by the respective dashed lines) and the energy release occurs after the passage at R_P. During this phase the black hole's tidal forces exerted on the star produce deformations and strong vertical compression on the stellar structure that result in the energy release with the maximum values attained immediately after the R_P passage.

In the case of the elliptic TDEs, the release of the thermal energy that is imparted from the kinetic energy of the star is achieved by each passage of the star at R_P. The models of the elliptic TDEs have the same R_P distances as the parabolic ones. Therefore the behaviour is similar in terms of the energy release, i.e., the first passage of the star at R_P is characterized by the release of the highest amount of thermal energy. In the subsequent passages by R_P there is a consecutive decrease of the energy release.

In Figure 4.21 the models 9 and 10 are the grazing ones and are shown in the left panel in terms of the thermal energy release as a function of the orbital period P_* of the star. The star in these two models suffers the less deformation by the tidal forces of the black hole as it passes at $R_P \simeq 2R_T$ in model 9 (with $b = 0.5$) and passes at $R_P \simeq R_T$ in model 10 (with $b = 1$) with a release of thermal energy of the order of a few 10^{47} erg.

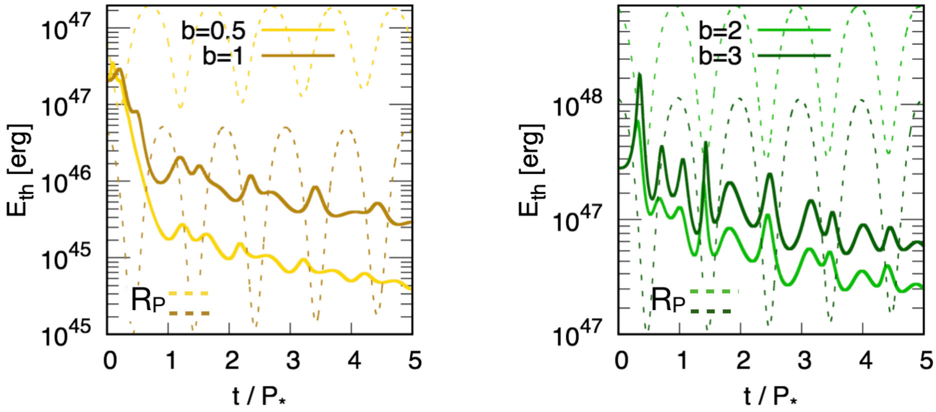

Figure 4.21: The thermal energy in models 9 and 10 (left panel) and models 11 and 12 (right panel), while the respective penetration parameters for each model appear at the top center of each panel. The pericenters are indicated in the bottom left corner.

Though it can be observed that the thermal energy release is achieved at each passage of the star at R_P. In the right panel of Figure 4.21 the models 11 and 12, which correspond to the penetration parameters of $b = 2$ and $b = 3$ respectively, have the larger amount of thermal energy release after the first passage at R_P and through each P_* after. The two spikes of the thermal energy that are observed at $t \simeq 1P_*$ can be attributed to the deformation of the star as it reaches R_P and begins to be stretched in two tidal tails. The energy release is of the order of $\sim 10^{47}$ for model 11 and of $\sim 10^{48}$ for model 12.

The evolution of the specific angular momentum of the star for each P_* by the passage at R_P is shown. The loss of angular momentum from the star finds a match with the lowest potential energy that gives the point of R_P where the release of thermal energy occurs.

In Figure 4.23 the release of the thermal energy is represented for the models 13 and 14 in the left panel and for the models 15, 16 and 17 in the right panel. Model 13 has a penetration parameter of $b = 4$ and presents a very similar behaviour in terms of the energy release than model 14, which has a penetration parameter of $b = 5$. With increasing b the distance between R_P and the black hole, with the R_S defining

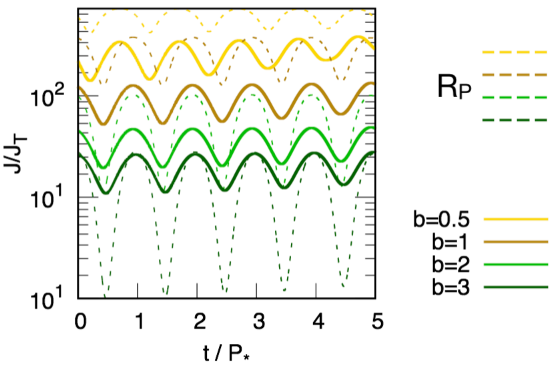

Figure 4.22: Evolution of the specific angular momentum J/J_T for the models 9, 10, 11 and 12.

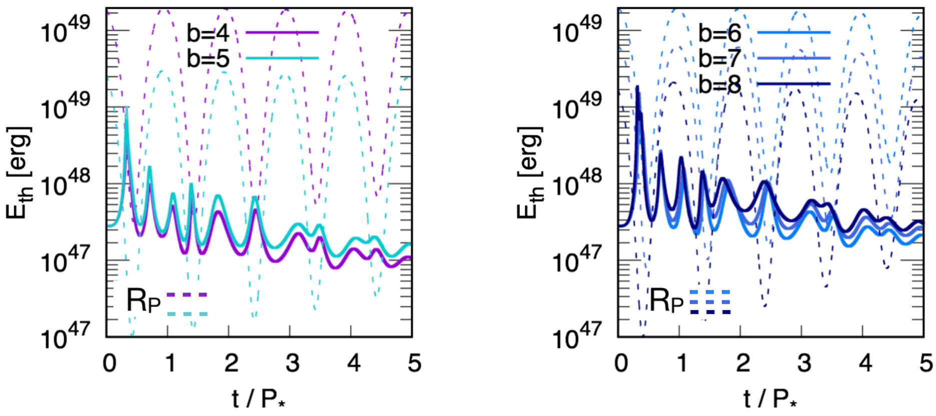

Figure 4.23: In the left panel are shown the models 13 and 14 and in the right panel the models 15, 16 and 17. The respective penetration parameters for each model appear at the top center of each panel. The pericenters are indicated in the bottom left corner.

its radius, decreases and the tidal forces destroy the star completely. In fact, at the first passage at R_P the star in model 13 loses $\sim 18\%$ of its initial mass and in model 14 $\sim 23\%$, with the respective decreasing distances of $\sim 39R_\odot$ and $\sim 31R_\odot$. The last three models 15, 16 and 17 represent those where the star has the shorter distances to the black hole. The energy release is of the order of $\sim 10^{49}$ erg.

The evolution of the specific angular momentum of the star for the models 13, 14, 15, 16 and 17 is

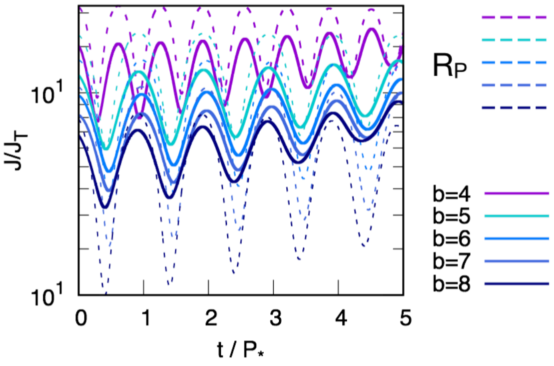

Figure 4.24: Evolution of the specific angular momentum J/J_T for the models 13, 14, 15, 16 and 17.

shown in Figure 4.24. As the star loses its angular momentum by the passage at R_P it releases the thermal energy that is imparted from the kinetic energy of the star as it approaches the black hole. The tidal energy transfer results from the passage of the star at R_P, where the tidal forces from the SMBH produce deformations on the stellar structure that will result in partial or complete destruction of the star. Such deformations are a function of the penetration parameter, meaning that with increasing b the tidal forces increase assimptotically, contributing to increasing amounts of thermal energy release that is imparted from the kinetic energy of the star at R_P. An interesting fact that results from the analysis of the thermal energy release in the parabolic and elliptic TDEs is that the most energetic events occur on the side of the parabolic TDEs, presenting in the most extreme situations ($b \geq 6$) ~ 1 order of magnitude higher in terms of thermal energy release (see Figure 4.25 and Table 4.7).

Models	b	Parabolic E_{th} [erg]	Elliptic E_{th} [erg]
1, 9	0.5	1.22×10^{48}	1.31×10^{47}
2, 10	1	1.42×10^{48}	2.26×10^{47}
3, 11	2	5.18×10^{48}	1.96×10^{48}
4, 12	3	1.44×10^{49}	3.79×10^{48}
13	4	$---$	7.11×10^{48}
5, 14	5	5.69×10^{49}	1.09×10^{49}
6, 15	6	9.29×10^{49}	1.37×10^{49}
7, 16	7	1.35×10^{50}	1.66×10^{49}
8, 17	8	1.78×10^{50}	1.92×10^{49}

Table 4.7: Quantified values for the thermal energy release for the parabolic and elliptic TDEs. Models 1 to 9 correspond to the parabolic case and models 10 to 17 to the elliptic case.

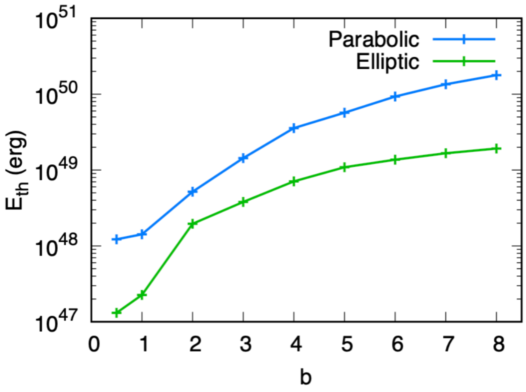

Figure 4.25: Thermal energy release for the parabolic (blue line) and elliptic (green line) TDEs as a function of the penetration parameter b. The parabolic $b = 4$ value was obtained by interpolation.

4.5 Stellar survival vs destruction

Stars in the presence of a point mass potential will follow keplerian orbits[3] if no external force acts upon them (Rees 1988). The position and velocity of a star can be recorded at its passage at R_P by the time when its gravity and pressure are no longer relevant. At R_T this conditions can be acomplished since the tidal force is greater than that of the stellar self-gravity. The limit for the survival or destruction of a star

---

[3] From the celestial mechanics, is the motion of one body in relation to another, describing ellpitic, parabolic or hiperbolic trajectories.

passing at R_P is not exclusively dependent on the tidal forces acting over the star to remove some mass but depends also on the potential of those forces to disrupt the stellar core (Guillochon and Ramirez-Ruiz 2013).

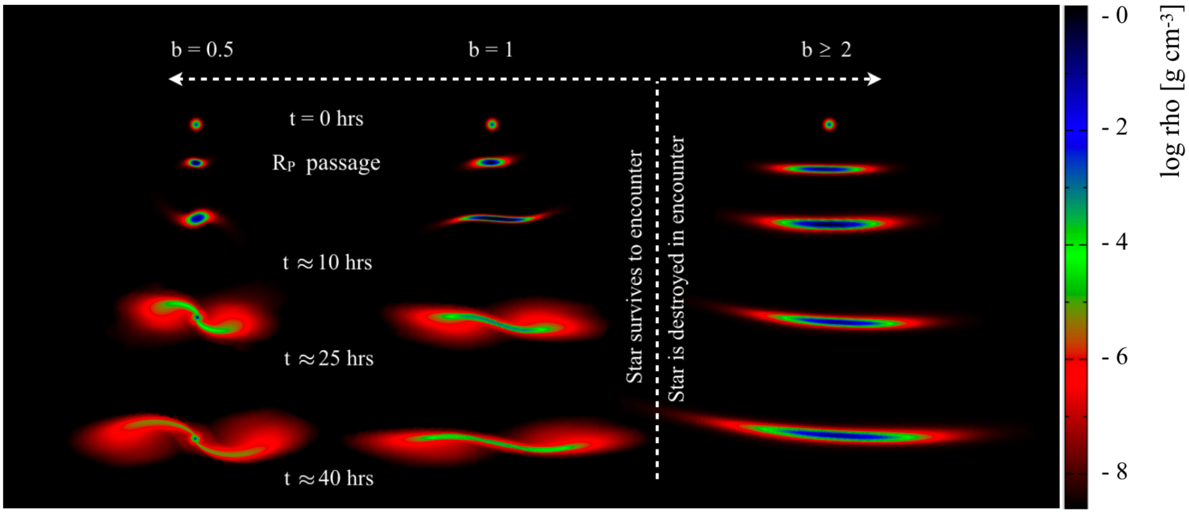

Figure 4.26: Snapshots of the density log ρ of the models 1, 2 and 3 of the parabolic TDEs. The limit between disruption and no disruption separates models 1 and 2 from the rest.

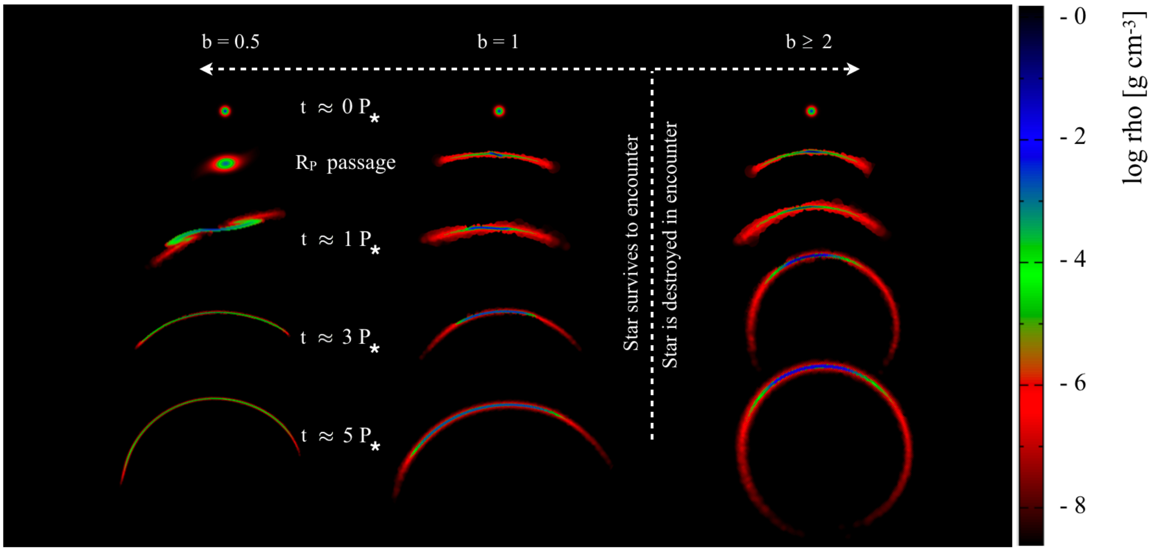

Figure 4.27: Snapshots of the density log ρ of the models 9, 10 and 11 of elliptic TDEs. The limit between disruption and no disruption separates models 1 and 2 from the rest.

As Main Sequence[4] (MS) stars have cores which are denser then their envelopes, their ratio to mass density is $\rho_{core}/\bar{\rho}_* \approx 100$. The stellar dynamical time of the core is lower than that of the envelope but during the encounter and depending on its strength, the gravitational influence of the core modifies

---

[4] Solar type stars can be classified as G-Type Main Sequence stars

the surrounding material of the envelope. Because of this rearrangement the adiabatic response of the condensed polytrope has the effect to contract during the mass loss, preventing the star from loosing more mass (Hjellming and Webbink 1987; Willson et al. 1987). In Figure 4.26 is shown the evolution of the stellar cores of the parabolic TDEs for the models 1 and 2 and generically the evolution of the cores from the models with penetration parameters of $b \geq 2$. While in models 1 and 2 the deformation of the star due to tidal forces is small and these are able to maintain their cores preserved, in all the other cases, by the same time, it can be observed (Figure 4.26) that the disruption of the star is effective with an associated loss of mass, where the stellar core suffers gradual deformation and is unable to avoid disruption due to the distortions from tidal forces.

Figure 4.27 shows the evolution of the stellar cores of the elliptic TDEs for the models 9 and 10, and in the same manner, a generic evolution for the models with $b \geq 2$. Also in the elliptic cases, the models 9 and 10 ($b = 0.5$ and $b = 1$, respectively) have less deformation then the other cases when $t = 1P_*$. Though the stellar cores can be preserved in the grazing encounters, the several passages at R_P implies that the tidal forces are able to continuously act on the stellar material, so deformation is more evident after some orbital periods, in this case after $t = 5P_*$.

For the cases where $b \geq 2$ the deformation of the stellar core occurs faster due to the steeper penetration parameters that imply deeper plunges of the star inside R_T. From the simulations, the models with the penetration parameter that lies between $[0.5 - 1]$ exhibit the capacity for the stellar core to maintain the envelope gas as shown in Figure 4.28 for the $b = 0.5$ parabolic case. The upper panel is a close view of the inner region of the star, where the core appears intact, though after the passage at R_P the star is excited but still its core is not disrupted.

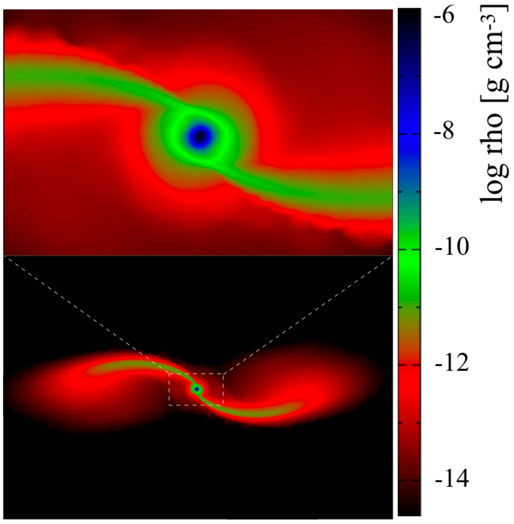

Figure 4.28: Close view of the stellar core of model 1. The inset shows that the core is unperturbed and the star maintain the envelope gas after the passage at R_P.

4.6 Summary

The SPH simulations implemented for this work concern the tidal disruption of a solar type star $M_* = 1M_\odot$ by a SMBH with mass $M_{BH} \sim 4 \times 10^6 M_\odot$, which is approximately the mass of the Milky Way's resident black hole Sgr A*. Two types of TDEs, parabolic and elliptic, were implemented in the keplerian regime, meaning that the relativistic effects are not taken into account (e.g., apsidal precession that leads to the self-intersection, collision and shocks of the debris).

A distinct feature of the simulated TDEs is the spatial distribution of the debris that forms after the passage of the star at R_P, which are quite different in the parabolic and elliptic cases.
In the parabolic TDEs the star describes an orbit with a parabolic trajectory that has an eccentricity of $ecc = 1$. The passage of the star at R_P causes deformation on the stellar structure due to the tidal forces of the black hole, which are a function of the penetration parameter b. As a result the star will develop two tidal tails produced by the debris that is depletted from its surface, which corresponds to the least bound material of the star. A portion of the debris, which can correspond up to $\sim 1/2$ of the debris that is removed from the star will be forcefully ejected, while the remainder will be bound to the black hole and will be accreted to it on a fallback rate of the bound debris.

The less penetrating encounters $b = 0.5$ and $b = 1$ are characterized by minor deformations due to the weaker effects of the tidal forces which allows for the star to maintain its self-gravitating core unperturbed or at least with small deformation. The encounters where $b \geq 2$ the star will suffer gradual deformation with the core being stretched with increasing b, until the self-binding energy of the star no longer resist to the tidal forces of the black hole. In such conditions the star is partially or completely disrupted foming an elongated shape known has the *pancake phase*. In elliptic TDEs the spatial distribution of the debris can be characterized by the circularization of the debris that results from the passage of the star at R_P. As the orbits have an eccentricity of $ecc = 0.3$, the resultant debris from the tidal disruption will settle in a near circular orbit.

The grazing encounters produce small deformation on the star at $t = 1P_*$ though for deeper encounters the star is quite deformed. After a few P_* the debris will settle around the black hole, though the star continuous to be depletted of its mass and the stellar core is progressively stretched until effective disruption occurs. The consecutive R_P crossing will produce a stream of the stellar debris that describes near circular orbits until it starts to be accreted, after several orbital periods. The debris that attains enough angular momentum and do not fall into the black hole will settle on a certain circularization radius which is defined by the specific circularization energy that results from the redistribution of the debris.

After the star crosses at R_P and suffers the effects of the tidal forces a fraction of its mass will be depletted from the stellar surface, which is quantified as a function of the penetration parameter. In the parabolic TDEs the net mass loss $(-\Delta M)$ at the first passage of the star at pericenter can be between $\sim 5\%$ for the $b = 0.5$ case up to $\sim 63\%$ for the deepest $b = 8$ case. In the elliptic TDEs the $-\Delta M$ for the first passage at pericenter the mass that is removed from the star can be of $\sim 3\%$ for the lower $b = 0.5$ and $\sim 58\%$ for the $b = 8$ encounter. The amount of mass loss with b is expected to increase with time, as more mass will be depleted from the stellar surface onto the black hole. The loss mass $(-\Delta M)$ asymptotes for the deeper encounters $(b \geq 5)$ while the encounters with lower b have more accretion time than the rest due to their longer crossing distances at pericentre.

The debris that returns to the SMBH is characterized by the peak of the mass fallback rate. The Milky Way's SMBH is $\approx 4 \times 10^6 M_\odot$ which gives a fallback time of $t_{fb} = 7.077 \times 10^6$ s $\approx$ 82 days. The return of the debris to the black hole is estimated by the peak of the fallback mass rate $\dot{M} \simeq 3M_\odot$ yr^{-1}.

The disruption of a star requires a certain amount of energy that must be greater than the binding energy of the star so its orbital energy will be reduced and consequently the kinetic energy of the star will decrease. With the crossing at R_P the star will have a kinetic energy of the order of $(M_{BH}/M_*)^{2/3}$ and will experience the distortion and compression due to tidal forces in such a way that the star suffers maximum compression and deformation and there will be a release of thermal energy that is imparted to the resultant debris at the expense of the kinetic energy. The gravitational binding energy of the gas to the SMBH will be converted in thermal energy until it reaches the last stable orbit around the black hole.

If the gas can dissipate the heat by the emission of radiation or acceleration of particles, then the thermal energy can be extracted by the time it reaches the last stable orbit. If on the other hand the dissipation of energy is inefficient, the heat can be advected onto the SMBH where it will be added to its rest mass (Rees 1988; Alexander 2005).

The tidal energy transfer results from the kinetic energy of the star by its passage at R_P. Due to the tidal forces of the black hole the kinetic energy is imparted into thermal energy, which is released for the surrounding medium. The amount of thermal energy release can be of the order of $\sim 10^{47}$ erg for the $b = 0.5$ encounter in both parabolic and elliptic TDEs and can go up to $\sim 10^{50}$ erg for the deepest encounter with $b = 8$ for the parabolic case and of the order of $\sim 10^{48}$ erg for the elliptic one.

The thermal energy release increases with b in both parabolic and elliptc TDEs. From the results obtained from the simulations it can be observed (Figure 4.25) that the parabolic TDEs release more thermal energy than the elliptic TDES by the first passage of the star at R_P.

The results described here match both the theory and those published by different authors. However, the new results described in this chapter stem from the high-resolution calculations and numerical methods adopted in the present simulations.

5

TDEs - a possible application to the Fermi Bubbles case

5.1 Introduction

The SMBH has observational properties that characterize it in terms of its mass and size as well as its spectrum, radio variability and even the regime of accretion (accretion rate). Some proposed models for the galactic black hole Sgr A* are briefly described, which relate some of the observed features (e.g., radio emission) to their possible origin. The TDEs signature that can be observed are shortly presented in terms of the unbound debris streams formed after the disruption of the star and also the CRs and γ rays production.

A possible contribution of the TDEs may be adressed to the Fermi Bubbles, whose origin and feeding mechanism is still not well understood. Results from the XMM-Newton satellite are refered to help unveiling the new evidences of the FB structures detected in these observations, especially those from 2016-2018 that detected the X-ray chimneys in the GC. The Fermi Bubbles were also targeted in hydrodynamical numerical simulations considering the relativistic jet scenario that can contribute to accelerate and transport the CRs, by advection, through the $\sim$ 10 kpc length of the bubbles suggesting that the CRs have the same age of the FB.

5.2 The SMBH in the GC - observational properties

The SMBH that resides in the center of the Milky Way was initially proposed as a compact radio source by Lynden-Bell and Rees (1971). Known as Sagittarius A* it is the most studied and well constrained black hole due to its proximity ($\sim$ 8 kpc). The initital evidences for the presence of the dark and compact object came from the Mid-Infrared (MIR) and X-rays (Lacy et al. 1979; Serabyn et al. 1988) and from the radio recombination line observations of gas streams around Sgr A* Roberts and Goss (1993); Zhao et al. (2010).

The improvement of the high spatial resolution and the capability in the detection of individual stars around Sgr A* gave the final breakthrough. Proper motion of stars can be detected Eckart and Genzel (1996); Ghez et al. (1998) and so the motions of individual stars have been traced over the last decades being used to map out the gravitational potential within stars describe their motion Ghez et al. (2000); Genzel et al. (2000). These stars move in general keplerian orbits with orbital speeds of 10^4 km s^{-1} and orbital periods of $\sim$ 15 years (Schödel et al. 2002; Gillessen et al. 2009). In fact these observations show that the gravitational potential in the central parsec of the Milky Way might be dominated by a point source which is comparable to the estimated black hole mass which is situated at a few hundreds of R_S from Sgr A* (Ghez et al. 2008) .

The exact location of Sgr A* represents the major limiting factor in the Near-Infrared (NIR) coordinate frame though it can be good within $\sim$ 2 mas (miliarcsecond), which corresponds to $\sim$ 200 R_S (Menten et al. 1997).

The proper motion of many stars combined with their radial velocities (determined from high resolution spectroscopy) yield the geometric distance of $d = 8.3\ (\pm 0.4)$ kpc (Eisenhauer et al. 2003; Ghez et al. 2008). The galactic SMBH can also provide the evidence for its own location, which associates the presence of a dark and compact object with its proper motion. The use of radio telescopes in the frame of Very Long Baseline Interferometry (VLBI) have tracked the position of the source for several years to a fraction of a mas per epoch (Reid et al. 1999; Reid and Brunthaler 2004). In Figure 5.1 is shown the radio position of Sgr A* and the measured locations and fitted orbit of the star S2, around Sgr A*.

As the motion on the sky of Sgr A* is very consistent with the motion of the solar system around the GC, i.e., the GC is the location of the radio source (not in the background or in the foreground), which implies that any motion perpendicular to the projected motion is less than $0.4\ (\pm 0.9)$ km s^{-1}. In this frame, more than 10% of the dark mass is associated with the radio source.

5.2.1 Spectrum of Sgr A*

To understand the SMBH Sgr A* as a source it is important to know how its size and emission spectrum are linked. The radio flux density S_ν (provided from the combination of all radio data on Sgr A*) presents a flat-to-inverted spectrum, which means that it rises in a slow rate with the frequency has the 10^{12} Hz peak in the submm band.

The radio spectrum of Sgr A* is represented in Figure 5.2. The broad-band spectrum of Sgr A* varies as $\nu \times L_\nu$, with $L_\nu = 4\pi D^2_{SgrA*} S_\nu$. In the GHz frequencies $S_\nu \propto \nu^\alpha$ ($\alpha \simeq 0.3 \pm 0.1$) and continues at the low frequency range ($\simeq 300 MHz$) not showing signs of absorption Roy and Pramesh Rao (2004); Nord et al. (2004).

The spectrum extends to the higher frequencies entering in the subTHz range (submm wavelength; Zylka and Mezger (1988); Mezger et al. (1989)). The spectrum has a peak in this range and shows a *cut-off* after, known as the *submm bump* and is due to the transition of the optically thick to thin of the synchrotron emission. Only the most compact regions can give rise to such emission, being these regions several R_S in diameter Falcke et al. (1998).

In Figure 5.2 the average spectrum is represented by the black points (Falcke et al. 1998; Zhao et al. 2003). The outer accretion flow dominates the black bowtie representative of the X-ray from Bondi radius scales (Baganoff et al. 2003) with a possible contribution of 10% of the flux from Sgr A* (Neilsen et al.

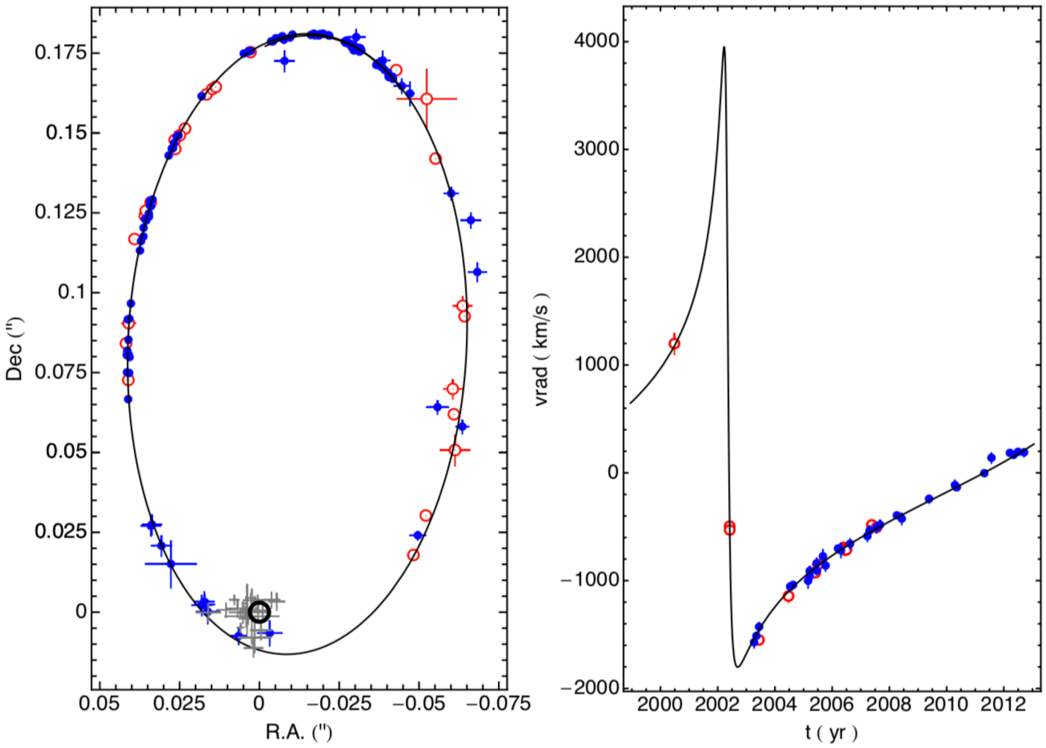

Figure 5.1: Radio position of Sgr A*
The radio position of Sgr A* from measured locations and fitted orbit of the star S2 around the SMBH (left panel), taken from Gillessen et al. (2009); Genzel et al. (2010).

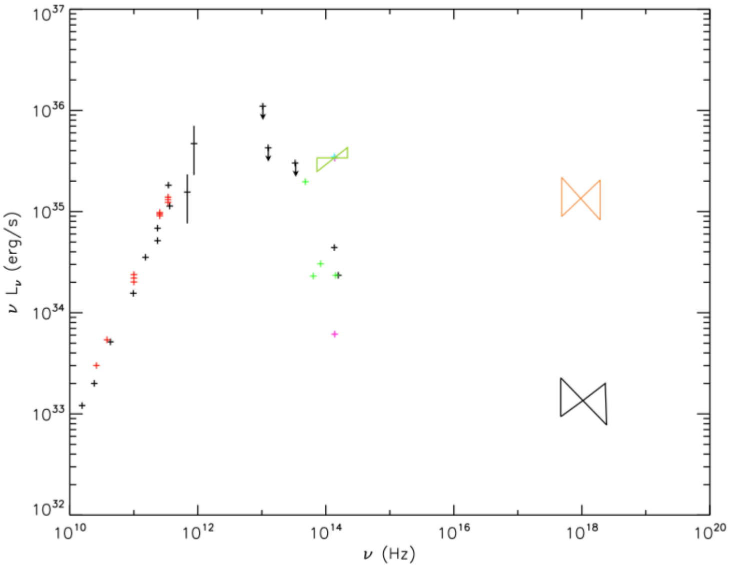

Figure 5.2: The broad-band spectrum of Sgr A*. The quiescent and flaring states are shown (Falcke and Markoff 2013).

2013). Radio data is represented by the red dots taken from ALMA, the InfraRed (IR) data are represented by the green dots from (Schödel et al. 2011) and the lower and upper limits of IR, respectively the pink and cyan dots are taken from (Ghez et al. 2004; Genzel et al. 2003). One of the few detected IR with a slope that is simultaneously a X-ray detection is represented by the green bowtie and is taken from (Bremer et al. 2011) and the orange bowtie is representative of the largest X-ray flare that was detected with Chandra (Nowak et al. 2012). Finally the blue dots are from two flares detected from NuSTAR, taken from Barrière et al. (2014).

5.2.2 Size and structure of Sgr A*

From interferometric data of Sgr A* it was found that the measured size and source did not correlate directly to the source itself. An ellipse of axial ratio 2:1 with east-west orientation produces a blur that covers the shape of Sgr A* and is caused by the scattering of radio waves of electrons in the ISM (more exactly between the solar system and the GC; Davies et al. (1976); Lo et al. (1985); Lo et al. (1998)). The dimensions of Sgr A* from observations follows a λ^2 law, where the scattered-broadened angular size (Falcke et al. 2009) can be given by

$$\phi_{scatt} = (1.36 \pm 0.02) mas \times (\lambda cm^{-1})^2. \tag{5.1}$$

The measured sizes have a small deviation from λ^2 at 22 and 43 GHz, obtained by a closure amplitude technique Bower et al. (2004).

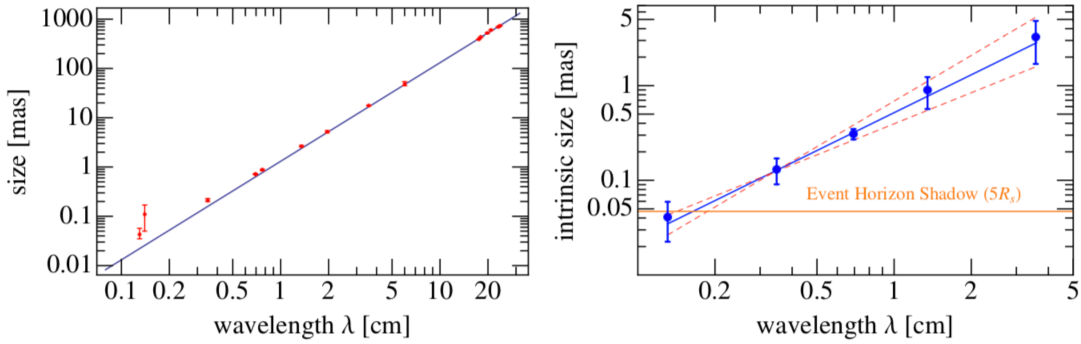

Figure 5.3: On the left panel the axis size of Sgr A* as a function of the measured wavelength. The scattering law λ^2 is indicated by the solid blue line. The intrinsic size of Sgr A* is derived, in the right panel. The event horizon is indicated by the solid orange line and the orange dashed lines are refered to the uncertainties of the scattering law. Pictures taken from Falcke et al. (2011)

Closure amplitudes form to combine complex amplitudes of the corelated data (known as the "visibilities") that are taken from different telescopes, which implies that telescope-based gain errors are cancelled. This way an accurate measure of the source size is provided by the closure amplitude. In fact, as the intrinsic size decreases with frequency it was revealed that for 230 GHz its size is only $\sim 4R_S$. Combining all data (Falcke et al. 2009) an intrinsic size for Sgr A* can be obtained

$$\phi_{SgrA*} = (0.52 \pm 0.03) mas \times (\lambda cm^{-1})^{1.3 \pm 0.1}. \tag{5.2}$$

The value of (0.52 ± 0.03) mas corresponds to $\sim (51 \pm 3) R_S$, as can be seen in Figure 5.3.

5.2.3 Radio transience of Sgr A*

The variability in radio emission of Sgr A* seems to increase in amplitude with frequency. For wavelengths of 13, 3.6, 2, 1.3 and 0.7 cm, the radio spectrum variation is of the order of $2.5, 6\%, 16\%$, 17% and 21%, respectively (Falcke et al. 2009), which reveals consistency with the adiabatic expansion of blobs of plasma that flows outwards in the form of a jet (Maitra et al. 2009). Different frequencies produce a time gap between flares, such that these occur at frequencies of 43 GHz and precede those that occur at frequencies of 22 GHz, by a time difference of $\sim$ 20 minutes. There is a difference of $\sim$ 30 light minutes between the two frequencies and to produce a flare that propagates from higher to lower frequencies it would be needed a relativistic outflow, if this represents density or energy enhancements in the radio-emitting plasma (Falcke et al. 2009).

5.2.4 Accretion onto the SMBH

The level of activity of the black hole can be determined by the accretion rate, which is the second most important parameter and can determine the level of activity (which varies by many levels of magnitude). The accretion rate of the SMBH can be estimated by the power that is radiated, unless the case is Radiative Inefficient Accretion Flow (RIAF).

Considering that Sgr A* may be accreting from winds of the surrounding stars, its accretion rate is estimated to be between $\sim 10^{-6} M_{\odot}$ yr^{-1} and $\sim 10^{-4} M_{\odot}$ yr^{-1} (Coker and Melia 1997; Genzel et al. 1994). The radial scale that determines the limit of accretion of the black hole (the Bondi Radius R_B) is mass and speed dependent of the surrounding gas, with $R_B = 2GM/v_w^2$, which represents the ideal Bondi-Hoyle accretion (Bondi and Hoyle 1944). In such case, stellar wind flows of $v_w = 600$ km s^{-1} have a Bondi radius of $\sim R_B \simeq 2.5 \times 10^5 R_S \simeq 0.1$ pc, which corresponds to the projected area in the sky of the GC (Melia 1992).

In terms of polarization Sgr A* is unpolarized in the range [5 GHz - 43 GHz] (Bower et al. 1999; Bower et al. 1999) as the accretion flow can produce a depolarization of the radiation due to a high Rotation Measure ($RM \simeq -6 \times 10^5$ rad m^2) that results in a very fast rotation of the polarization vector.

Linear polarization was detected at submm-waves with a RM $\simeq -6 \times 10^5$ rad m^{-2} (Bower et al. 2005; Marrone et al. 2006; Macquart et al. 2006), which is the highest RM being in any source. The accretion rate in the range of magnetic field profiles for the accretion flows can be limited in the interval between $\dot{M} \geq 10^{-9} M_{\odot}$ yr $^{-1}$ and $\dot{M} \geq 10^{-7} M_{\odot}$ yr $^{-1}$, where the scales can lie between $10^2 - 10^3 R_S$ Marrone et al. (2006); Sharma et al. (2007).

Thermal X-ray emission was associated to Sgr A* by the Chandra X-ray Observatory during the first polarization measurements (with a spatial resolution of 0.6×10^{12} km $\simeq 0.02$ pc). That emission from Sgr A* has a $k_B T = 1.9$ KeV with a slight extension for the bound accretion flow ($\sim R_B$; Baganoff et al. (2003)). The Bondi accretion rate ($\dot{M}_{Bondi}$) is given by

$$\dot{M}_{Bondi} = 4\pi n G^2 M_{BH}^2 c_s^{-3} \tag{5.3}$$

$$\simeq 10^{-4} M_{\odot} yr^{-1} \left(\frac{M_{BH}}{4.3 \times 10^6 M_{\odot}}\right)^2 \left(\frac{\eta}{160\ \mathrm{cm}^{-3}}\right) \left(\frac{k_B T}{1.9\ \mathrm{keV}}\right)^{-3}, \tag{5.4}$$

with the density normalization being inferred from X-ray measurements Baganoff et al. (2003) and the sound speed (c_s) is

$$c_s = \sqrt{\frac{5}{3} k_B T / m_p} = \left(\frac{k_B T}{1.9\ \mathrm{keV}}\right)^{1/2} 550\ \mathrm{km\ s}^{-1}. \tag{5.5}$$

Radio polarization increase the accretion scenarios with associated mass loss (Wang et al. 2013). At 0.1 pc, near Sgr A*, the detection of a radio pulsar showed a very high rotation measure of $RM \simeq 7 \times 10^4$ rad m^{-2} that requires magnetic fields of the order of a few mG. The Faraday screen associated to Sgr A* can be supported by this idea, implying that the accretion flow is developing (Eatough et al. 2013).

5.2.4.1 Accretion energy onto the SMBH from TDEs

The accretion energy onto the SMBH is the highest energy scale in TDEs (Alexander 2005). The stellar bound debris can circularize around the black hole after disruption and its stream can self intersect, collide and shock. If the gas is to fall gravitationally into the black hole, than it will have to lose its angular momentum and the black hole will exert tidal torque over the orbiting gas in order to induce a spiral inward of the gas through a viscous timescale.

The gas that is gravitationally inbound to the black hole can be converted into heat when it reaches the last stable orbit around the compact object. It will then fall into its event horizon on a dynamical timescale. If there is emission of radiation, it will dissipate the heat that was produced or the heat can also be dissipated by the acceleration of particles. If the gas does not fall into the black hole, it can escape as a wind by advection dominated inflow-outflow solutions - ADIOS (Narayan et al. 2000). For the radiative efficiency case the accretion energy onto the SMBH is given by Alexander (2005)

$$E_{acc} \sim \eta \left(\frac{M_*}{2}\right) c^2 \sim \eta b^2 \left(\frac{M_*}{M_{BH}}\right)^{1/3} \left(\frac{c}{V_e}\right)^2 E_{out}, \tag{5.6}$$

where E_{out} is the kinetic energy carried by the stellar debris ($E_{out} \sim W$). In case of radiative inefficiency, i.e., if the energy dissipation is inefficient, the heat produced can be transported (by advection) by the flow into the black hole where it will be added to its rest mass, in a process of Advection Dominated Accretion Flow (ADAF) solution (Van Den Bergh 1982; Narayan and Yi 1995).

For a typical TDE at the Galactic Center (GC) with a penetration parameter of $b \simeq 1$ the work done over the stellar debris is $W \gtrsim 100E_*$ which causes the debris to be released with specific energies of the order $(E_* \pm W)/M_*$.

The tidal force that exerts a specific amount of work (W) over the stellar debris is Alexander (2005)

$$W \sim M_* \phi_{BH}(R_P) \sim \frac{GM_{BH}M_*}{R_P^2} R_*, \tag{5.7}$$

where $M_*\phi_{BH}(R_P)$ is the the black hole's gravitational potential difference across the star at R_P.

5.2.4.2 Emission curve from the simulated TDEs

From the simulated TDEs of the present work an emission curve of the accretion energy and work done on the stellar surface was obtained with the quantified values shown in Table 5.1 and in Figure 5.4.

Model	b	E_{acc} [erg]	$Work$ [erg]
1, 9	0.5	1.012×10^{50}	1.505×10^{50}
2, 10	1	4.048×10^{50}	6.022×10^{50}
3, 11	2	1.620×10^{51}	2.409×10^{51}
4, 12	3	3.644×10^{51}	5.420×10^{51}
13	5	2.050×10^{51}	9.633×10^{51}
5, 14	5	1.012×10^{52}	1.505×10^{52}
6, 15	6	1.458×10^{52}	2.168×10^{52}
7, 16	7	1.984×10^{52}	2.951×10^{52}
8, 17	8	2.591×10^{52}	3.854×10^{52}

Table 5.1: Quantified values for the accretion energy (E_{acc}) and work done over the stellar debris (Work) from TDEs at R_P.

The disruption of the star implies that the tidal torquing spins the star up in the same direction of the stellar orbit which increases an excess of velocity that is higher than the orbital velocity of the star on the far side of the black hole, which contrasts with the opposing deficit in velocity in the near side. These discrepancies in the velocities will develop a spreading of the specific kinetic energies. Such energies are considered as the second highest energy scale related to TDEs. The highest energy scale regarding these events is the accretion energy E_{acc}. Both the work W and the energy accretion E_{acc} can be obtained by (5.6) and (5.7) Alexander (2005) . From Figure 5.4 it is shown that both E_{acc} and the W increase as a function of the penetration parameter b.

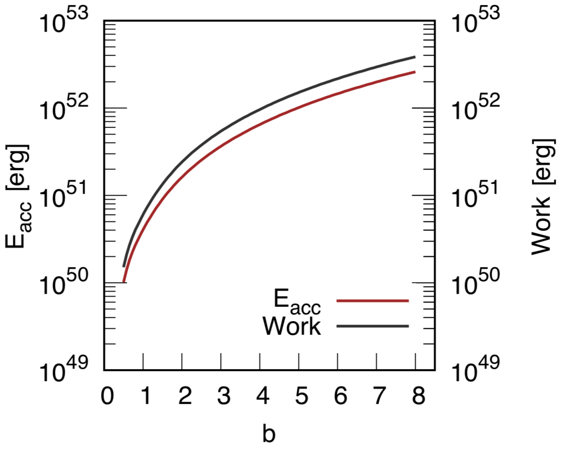

Figure 5.4: Work done on the stellar debris (black line) and the accretion energy onto the SMBH (brown line), as a function of the penetration parameter b.

5.3 Proposed models for the emission on Sgr A*

The closest SMBH to the solar system is Sgr A* and it represents a valuable source for the study of accretion (accretion theory), the emission processes and also its physical geometry. Different interpretations for the emission model can take to different interpretations of the data for the region near the black hole. Understanding the astrophysics of this region is fundamental to predict the gravitational scenarios.

5.3.1 Accretion models

There are a few puzzling facts about Sgr A* that are mentioned to be pointed out, such:

i) The SMBH Sgr A* presents today a very low level of activity. It's actual accretion rate seems to be below the accretion rate that is needed to develop a few $10^6 M_{\odot}$, about four orders of magnitude, in a Hubble time (Bower et al. 1999);

ii) The luminosity function for radio cores is above the radio luminosity of Sgr A* (Nagar et al. 2005);

iii) Sgr A* needs to be fueled by an amount of gas that is many orders of magnitude higher than what is actually observed (Clarke 1981; Haubois et al. 2012).

Sgr A* initial models needed vrey high accretion rates due to their inefficiency, though after the availability of the radio polarization results, these accretion rates were adapted. Models based on the Radiative Inefficiency Accretion Flows (RIAF) could explain the weak radio and X-ray emissions (L(2-10)KeV $\simeq$ 2.5 $\times 10^{33}$ erg s^{-1}) by the Advection Dominated Accretion Flow (ADAF; Narayan and Yi (1995); Narayan et al. (1998)). The RIAF models have a common characteristic involving the radiative efficiency which is the ability to mask the energy with less radiative protons and ions that can advect the energy beyond the SMBH event horizon and can also enable the mass loss from accretion flows through outflows.

From the accreted material, only a small portion of it can make it to the most inner regions of the SMBH, the rest of the material will be lost. The X-Ray Visionary Campaign Project (XVP) returned results that corroborate the evidence of an outflow. These results show that the diffuse emission is elongated consistently with the stellar disk that can be observed with the NIR (Wang et al. 2013). Also used for the first time in such campaigns, the High Energy Transmission Greetings Spectrometer (HETGS; Canizares et al. (2005)) provided high resolution spectroscopy and the highest spatial resolution in the X-ray band, providing also the resolution of the Fe and $K_\alpha$complex into distinct lines. The radial profiles of the gas temperature and density have been constrained due to the measured ratio of H-like to He-like Fe lines and in these conditions the frame of the *no–outflow* was put aside Shcherbakov and Baganoff (2010).

5.3.2 Possible jet in Sgr A*

The radio emission from Sgr A* was suggested (Reynolds and McKee 1980) to be from a jet or wind from stellar-sized objects. Larger scales have lesser dense regions and weaker magnetic fields, which imply a lower frequency emission (Blandford and Königl 1979). These facts contributed to explain the spectrum and frequency-dependent size of Sgr A* that were attributed to a down-graded quasar jet (a SMBH with a very low accretion rate; Falcke et al. (1993); Falcke and Markoff (2000)). Though jets have not been observed directly pouring from Sgr A*, there are models that have proposed the emission being produced in the accretion flow itself (Yuan et al. 2003). Also, the radio time lags may suggest a relativistic outflow with the non-thermal emission of the X-ray flares fitting on *fundamental plane of black hole activity*. The plane connects radio and X-ray emission of low accreting black hole mass (Falcke et al. 2004; Merloni et al. 2003). It looks like that Sgr A* is poorly fueled, radiatively inefficient though launching a jet (Liu et al. 2004).

5.3.3 Production of flares and particle heating

Some arguments such the flattening of the X-ray spectrum, the NIR variability and the flares fast timescale sustain a non-thermal process. The fast heating and particle acceleration resulting in direct synchrotron emission form the up-scattered submm bump photons can be the consequence from magnetic reconnection and stochastic processes (Markoff et al. 2001; Liu et al. 2004; Yuan et al. 2004). A consequence of this can be the resulting synchrotron emission of X-ray or the synchrotron-self Compton emission due to the photons that were up-scattered in the submm bump.

Accretion flows in Sgr A* can transport fragmented/vaporized asteroids that can trigger flares in the NIR/X-ray, which are consistent with observations (Zubovas et al. 2012). The synchrotron-self Compton emission seems to be favoured by some flares in the NIR/X-ray (Eckart et al. 2004) while direct synchrotron emission in the X-ray band seems to be favoured by others Dodds-Eden et al. (2009), though it may be an interplay between both processes. Flares produced in the NIR/X-ray seem to play an effect of particle acceleration which can represent an increase of the size of the jet photosphere, that depends on the radiating particle distribution , which allows a small size in the jet photosphere (Markoff et al. 2007). On the other hand, if the particle acceleration result in a bright flare, the plasma is then advected into the jet where the variability in the size can be associated to the NIR/X-ray flares.

The Very Long Baseline Array (VLBA) observations from the XVP-linked multi-wavelength campaign were deployed by the NIR flares, where an observation of what could be the variability in the radio photosphere was obtained (Bower et al. 2004).

5.3.4 Cosmic Rays production

The production of CRs occurs from strong shocks (like those produced in TDEs.) The Diffuse Shock Acceleration (DSA; Fermi (1949)) is the mechanism that is responsible for such production and it is well established due to the studies from SNRs (Hinton and Hofmann 2009). From these studies it is suggested that $\sim 10\%$ of the kinetic energy that is injected in the shock can be knocked to accelerate CRs. Also suggested is the fact that the CRs that escape from the shock region follow the universal power law of $\gamma \simeq 2$ (Treumann 2009). A collision between the unbound debris stream and MCs would produce an amount of kinetic energy of $\varepsilon_k \sim 10^{49}$ erg of CRs. Considering T_p the space of kinetic energy as the convenient frame for the neutral π^0 and γ ray production, the CRs spectrum (Cheng et al. 2011) would be

$$\frac{dN_p}{dT_p} \propto \frac{T_p + 1}{(T_p^2 + 2T_p)^{(\gamma_0+1)/2}}. \tag{5.8}$$

The CR spectrum will have a cut off at a maximum $T_{p,max}$, if $\gamma \leq 2$, so the total ε_k does not diverge. The particle acceleration mechanism, the strength of the magnetic field and the power of the shock are the factors from which the maximum energy depends of. The maximum energy $T_{p,max}$ can be Hinton and Hofmann (2009) obtained by

$$T_{p,max} \simeq 10^2 v_3^2 t_2 B_{mG}, \tag{5.9}$$

with $v_3 = v_s/(10^3)$km s^{-1} and $t_2 = t_s/(10^2$ yr$)$ which are the shock strength and the shock acceleration timescale (t_s with units of 100 yr) and the magnetic field strength B_{mG} with units of mG, with the above formula being considered under the Bohm diffusion[1], where the lower limit for $T_{p,max}$ can be obtained.

As the shock velocity decays with time as $(t/t_0)^{-1}$, where $t_0 \simeq D/v_0 \simeq 1.6 \times 10^2 m_6^{-1/6} m_*^{-1/3} r_*^{1/2} D_1$, with $D \sim 1$ pc $\gg R_T(M_{BH}/M_*)^{1/3}; v_s = (6000, 3800)$ ms^{-1} and $t_s = t - t_0 = (10, 100)$ yr, under the assumption of $m_6 = m_*, r_* = D_1 = 1$. From observations of the GC for the magnetic field (Yusef-Zadeh et al. 1996) it was showned that B_{mG} ranges from 2-4 mG at the edge of MCs and 0.2 mG between MCs (Crocker et al. 2005). Assuming that $B_{mG} = 1$ the maximum energy ranges between $T_{p,max} \simeq (0.36, 1.4)$ PeV for $t - t_0 = (10, 100)$ yr (Chen et al. 2016). From the interaction of the unbound debris streams and a smooth ISM, the maximum energy is also in the range of PeV and so the bound debris streams effectively accelerate the PeV Crs Cheng et al. (2011). The non-relativistic protons in the MC will be hit with the CRs that escape from the shock region and an important amount of proton-proton collisions (pp-collisions) will be inelastic so the CRs can loose their kinetic energy and cool down. The timescale of pp-collisions can be obtained through $(\sigma_{pp} n_H c)^{-1}$ where the cross section for the collisions $\sigma_{pp} \simeq 40$ mbarn[2] and the speed of light is c. The cooling timescale for pp-collisions (τ_{pp}) is given by

$$\tau_{pp} = (k\sigma_{pp} n_H c)^{-1} \simeq 5.9 \ \text{yr}, \tag{5.10}$$

with $k = 0.45$ representing the inleasticity of the collision Fatuzzo et al. (2006)

5.3.5 Gamma Rays production

The neutral π^0 for the γ rays production by pp-collisions and the γ ray luminosity is given by (Fatuzzo et al. 2006)

$$L_\gamma = \eta(\sigma_{pp} n_H c) E_{CR}(t). \tag{5.11}$$

The total energy of CRs that are inside a MC is $E_{CR}(t)$ and the background protons is $\sigma_{pp} n_H c$. The neutral pions π^0 production is given by η. The increase of γ_0 from 2 to 2.6 implies a decrease of η from 0.18 to 0.04 (Crocker et al. 2005). When the unbound debris stream collides with a mC from $t = t_0$ to $t_0 + \tau_{pp}$, the CRs that are produced don´t cool down immediatly so the total energy of CRs (E_{CR}) increases monotically. The luminosity increases as $L_\gamma = (\eta\varepsilon/k) E_k C(t)/\tau_{pp}$ when the time lies between

---

[1] When particles cross the shock front in the slowest diffusion process

[2] Unit of area: mbarn=10^{-27} cm^2, used to express the cross sections of scattering processes in high-energy physics

$t_0 < t < t_0 + \tau_{pp}$ and $C(t) = 1 - (t/t_0)^{-4}$. The evolution of the luminosity L_γ implies that the γ ray emission is only effective several hundreds of years after the TDE occur and has a timescale of tens of years. The peak luminosity of a TDE is $L_{peak} \sim 10^{39}$ erg s^{-1}, meaning that there is a higher π^0 production rate for a lower CR cooling time, if n_H is large enough (Chen et al. 2016).

5.4 The Fermi Bubbles case

The TDEs phenomena that occur in the GC due to the SMBH interaction with stars has been pointed as a possible contribution to explain the FB. These structures were discovered during the Fermi-LAT (Fermi-Large Area Telescope) survey that detected two very large bubbles in the γ ray spectrum, with an extension of $\sim$ 10 Kpc in diameter north and south of the GC. First discovered in the X-rays by the ROSAT X-ray it was later confirmed with the WMAP (Wilkinson Microwave Anisotropy Probe) that detected an excess of radio signals in the region of the FB.

The origin of the FB is still not clear and several scenarios have been proposed in an attemptive to explain its formation and how such structures are maintained. Proposed scenarios for the FB are the energy injection by accretion events onto the SMBH or a nuclear starburst in the past 10^7 yr (Cheng et al. 2011; Su et al. 2010). The accretion episodes can be due to sucessive star captures by the black hole producing TDEs. The SMBH Sgr A* has a capture rate of $\sim 3\times10^{-5}$ yr^{-1} and energy release that can go up top 10^{52} erg per capture. These processes can produce very hot plasma $\sim$ 10 KeV and winds with velocities of $\sim 10^8$ cm s^{-1}. When injected into the halo, the gas can be heated up to $\sim$ 1 KeV producing thermal X-rays. Periodic injection of such hot plasma can produce shocks in the halo where electrons will be accelerated to $\sim$ TeV and radio emission will occur through synchrotron radiation and IC scattering that can produce γ rays (Cheng et al. 2011). A schematic of the FB mechanism is shown in Figure 5.5 to summarize the observations.

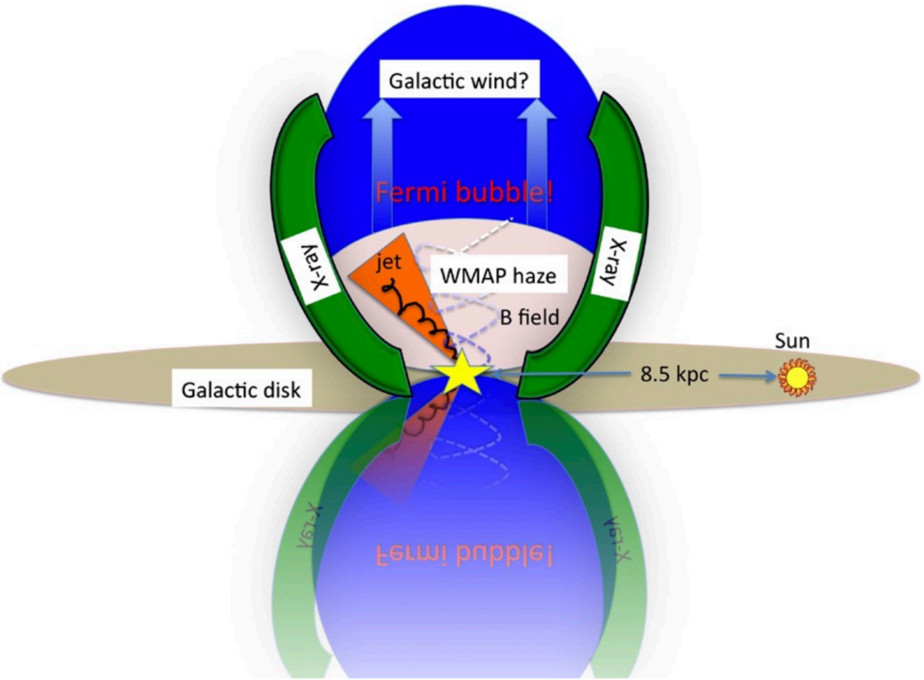

Figure 5.5: Schematic of the FB structures from observations showing two symmetric bubbles at the GC (Su et al. 2010).

Two blue bubbles symmetric to the Galactic disk indicate the geometry of the gamma-ray bubbles observed by the Fermi-LAT. Morphologically, it can be observed the features in ROSAT soft X-ray maps, shown as green arcs covering the bubbles. The WMAP haze shares the same edges as the Fermi bubbles (the pink ellipse inside the blue bubbles) with smaller extension in latitude. Such structures can have a similar physical origin: past AGN activities or a nuclear starburst in the GC (represented the yellow star).

The XMM-Newton survey of the $1,5$ degrees of the GC gives a very high spatial resolution that allowed to obtain images of the physical processes occurring in the GC. The Central Molecular Zone (CMZ) concentrates $(3-5)\times 10^7 M_\odot$ in the inner $\sim$ 200 pc, which corresponds to $\sim 1\%$ of all the molecular mass of the Milky Way (Morris and Serabyn 1996). Two lobes were detected in the soft X-ray with dimensions of $\sim$ (5-10) pc, north and south of Sgr A*, known as the bipolar Sgr A* lobes (Markoff 2010).

5.4.1 Sgr A* lobes morphology from XMM-Newton

The north and the south lobes at the GC present a co-aligned major axis that have a perpendicular orientation with respect to the galactic plane. The position of Sgr A* seems to be the point of origin of the lobes (bubbles). The emission of harder soft X-ray from the lobes (with an orange color) can be observed in Figure 5.6.

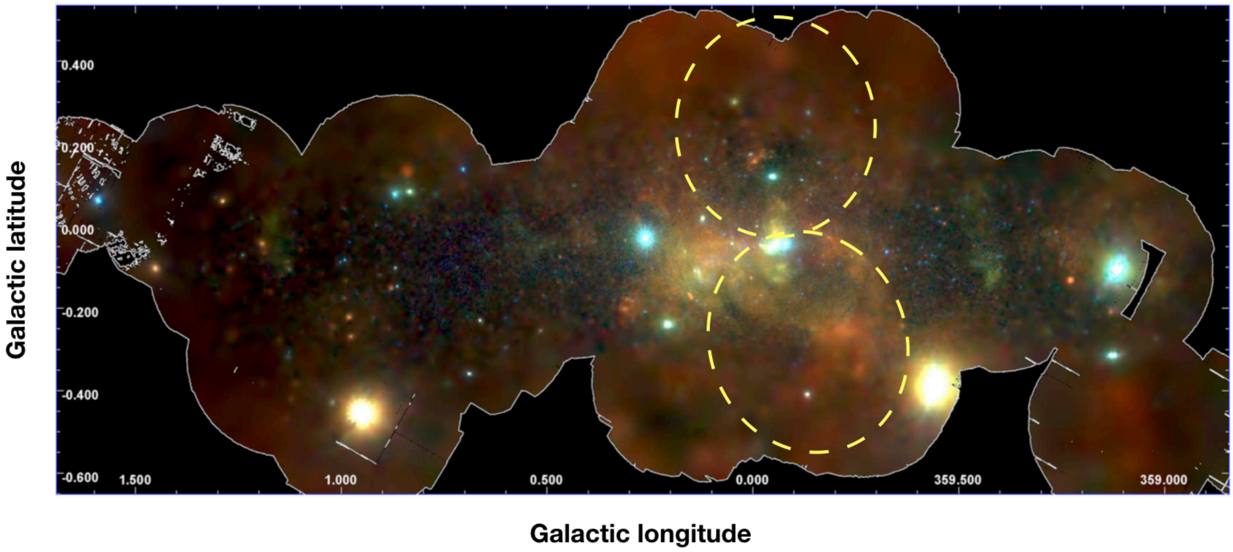

Figure 5.6: The orange colors of the lobes (dashed yellow cirles) indicate a harder soft X-ray emission compared to the surrounding regions (Ponti et al. 2015).

The lobe on top of the galactic plane - the northern lobe, evidences a brighter and harder structure, suggesting the presence of a shock, which might be an indication that this lobe is a bubble involved by a thin shell of hot material that is enhanced by the Chandra data in Figure 5.7 . The southern lobe presents two britght points (one at the center and the other at the tip) that seem to be like two enhancements in the northern lobe as these are located at the same approximate distance in the opposite direction (that of the northern lobe). As both lobes appear to have the same physical origin, also the formation mechanism of the two bubbles seems to be symmetric about the galactic plane and appears to have the same location of Sgr A*, which might be sugestive of a near symmetric ejection of hot gas, above and below the GC during some energetic event. Considering that there is absorption by MCs of the soft X-rays, the symmetry between the two lobes becomes more evidenced (Ponti et al. 2015). The isotropic outflow from Sgr A* is assimilated by the circumnuclear disc which contributes to create the bubbles of hot plasma. These bubbles (lobes) can be the result of a sequential injection of energy from the immediate surroundings of Sgr A* (Morris et al. 2003).

Considering a large scale structure that might be interacting with massive clouds from the CMZ and with a possible magnetic origin is the Galactic Center Lobe (GCL). A possible origin for the GCL is related to the transport of plasma from the galactic plane, due to GC activity like a past AGN (Law et al. 2011).

In terms of the energy involved, the lobes integrate an amount of thermal energy of $E_{th} \sim 9 \times 10^{49}$ erg, over a cylinder of 5 pc in radius and 12 pc in height (corresponding approximately to the size of the lobes; (Ponti et al. 2015)). Within 1 pc of the GC is estimated that massive stars will lose $\sim 5 \times 10^{-3} M_{\odot}$ yr^{-1} due to the effect of stellar winds that can reach to 1000 km s^{-1} (Geballe et al. 1987). During shocks the kinetic energy that is converted to thermal energy is of the order of $E \sim 5 \times 10^{49}$ erg s^{-1}, considering the above mass rate of the outflow (Quataert and Loeb 2005). The time required to inflate the lobes in such scenario is of $\sim 4 \times 10^{3}$ yr, which gives a release of energy of $E \sim 5 \times 10^{49}$ erg (Ponti et al. 2015).

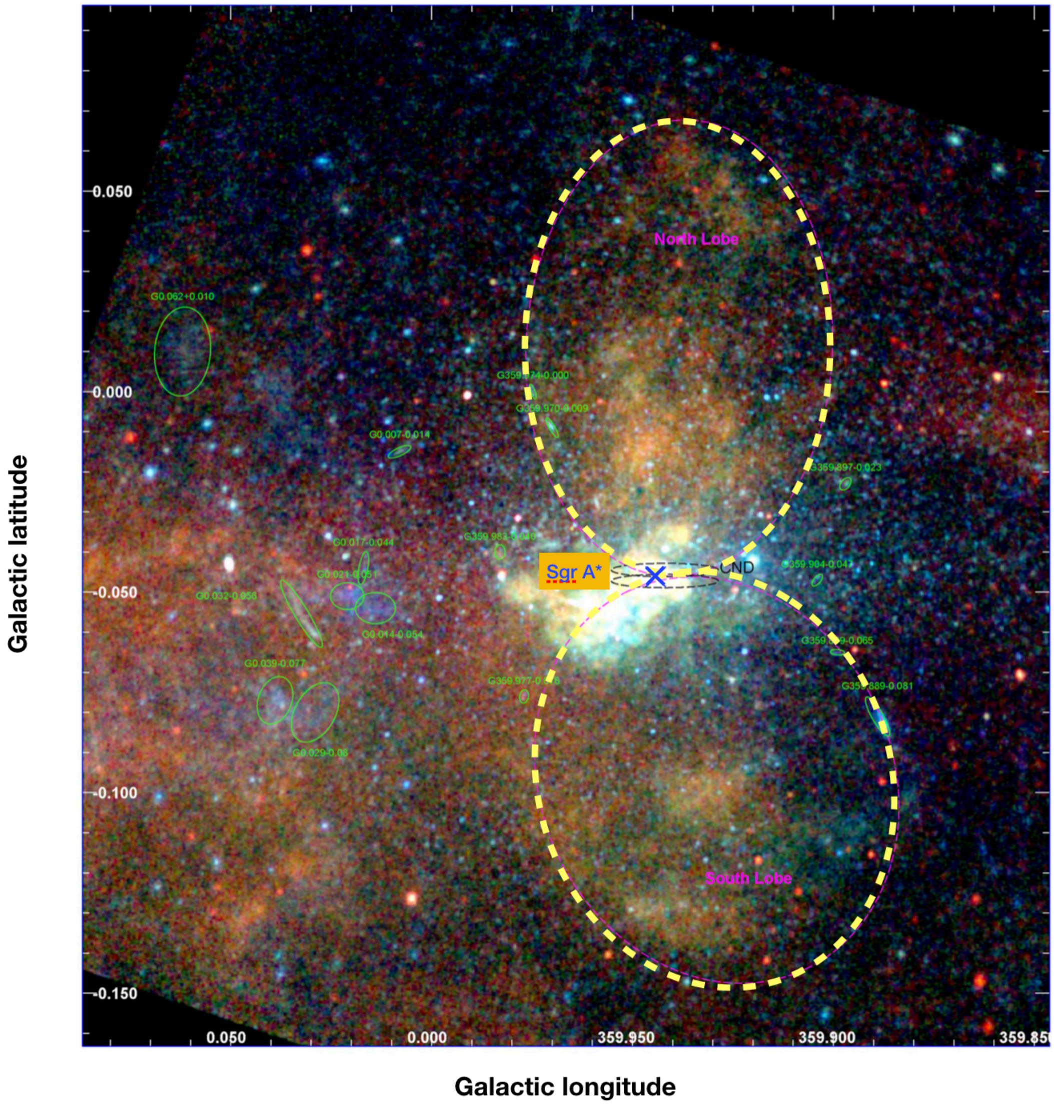

Figure 5.7: Chandra data of the lobes, considering there is absorption by MCs the symmetry between the two structures is more clear (Ponti et al. 2015).

In terms of the accretion flow onto Sgr A*, $\sim 1\%$ of the matter that is captured reaches the central region of Sgr A* (Wang et al. 2013). The remain material represents the accretion power of $\sim 10^{31}$ erg s^{-1} that can be converted into kinetic energy that will carry away the bulk material in an outflow, taking $\sim 10^{50}$ erg of total energy to the lobes, within its inflation time (Ponti et al. 2015). Sgr A* was $\sim 10^{6}$ times brighter than it is today witin the Central Molecular Zone (CMZ). About 5% to 10% of the last $\sim 10^{3}$ yr it had a luminosity of $L_X \sim 10^{39}$ erg s^{-1} (Ponti 2012). If such events have occurred over the last (5-10)$\times 10^3$ yr with a luminosity of $L \sim 2 \times 10^{39}$ erg s^{-1} during $\sim 10^3$ yr in the last $\sim 10^4$ yr, then it could have achieved a total energy of $E \sim 5 \times 10^{49}$ erg. Considering that the former activity of Sgr A* might have been due to outburts characterized by outflows with kinetic luminosity reaching the radiated power, then such events could be viewed as the main source to form the lobes (bubbles; Ponti et al. (2015)).

5.4.2 X-ray chimneys in the GC

At the GC, bipolar lobes develop on scales of $\sim$ 15 pc, which can be observed in X-ray and radio parts of the spectrum Zhao et al. (2016) that reveal vast ouflows from the GC and perpendicular to the galactic plane. The SMBH at the center of the Milky Way is the radio source Sgr A* located at the GC in the approximate location of the bipolar lobes as can be seen in Figure 5.8. From the observations of the XMM-Newton between 2016-2018 two new structures of moderate edge-bright at 160 pc both above and below Sgr A* which are refered by Ponti et al. (2019) as the northern and southern GC chimneys. These structures are two extended long channels of well collimated expansion of very hot gas that streams above and below the galactic plane of the Milky Way (Tomisaka and Ikeuchi 1986; de Avillez 2000; de Avillez and Breitschwerdt 2005)

As these chimneys present an approximate X-ray brightness and colour it is likely that they also share a common origin and emission mechanism, probably at the GC.

These chimneys develop more than 1 degree over the galactic plane in both north and south regions where the ROSAT X-ray detected a wider plasma emission, which might be identified as the counterparts of the FB or these observed X-rays were originated from shocks of thermal gas that surrounded the lobes probably due to past activity at the GC (e.g., Active Galactic Nuclei, AGN). The thermal energy of these lobes is $\sim 10^{58}$ erg with an outflow power of $\sim 8 \times 10^{38}$ erg s^{-1} if the age of the lobes is $\sim 3 \times 10^4$ yr. Such energetics could be provided by accretion events onto the SMBH like TDEs that can release thermal energy in the range between $[10^{51} - 10^{52}]$ erg with a stellar capture rate of $\sim 3 \times 10^{-5}$ yr^{-1} or by SNe at the GC.

The X-ray data give a thermal energy in the chimneys of $\sim 4 \times 10^{52}$ erg with an energy filling of the lobes with a power of $pc \simeq 4 \times 10^{39}$ erg s^{-1} (Ponti et al. 2019). These structures are likely to be restricted in the longitudinal direction with sharp edges throughout their vertical extent as shown in Figure 5.9.

The X-ray emitting gas as an estimated pressure in the chimneys of $P \simeq 0.1 - 0.2$ KeV cm^{-3} which seems to be in agreement with this restriction given the magnetic pressure of $p \simeq B^2/8\pi$ for a required 60-90 μG. As these structures appear to have an approximate cylindrical shape of $\sim$ 100 pc width for a latitude of $b > \pm 2$ the latter author cast the possibility that these might be formed by an energy injection mechanism in the GC. Above 1 degree the chimneys appear to mix with the FB as seen in ROSAT X-ray (Figure 5.9) which can be attributed to a decrease in temperature occuring above the galactic plane at $\sim$ 160 pc for the northern chimney Ponti et al. (2019).

On the light of these new data from XMM-Newton (2016-2018 observations) the authors argue the fact that the 160 pc chimneys and the $\sim$ 15 pc bipolar lobes might be parts of an outflow with origin near Sgr A*, though the X-ray data seem to put aside the idea of these structures being the prolongation of the inner lobes, which can represent the most recent event of energy injection in the chimneys within the most inner parsec. One possible hypothesis is the energy release by a SNe justifying the distribution of massive stars in the GC. Though other hypothesis cannot be discarded like TDEs which contribute with very energetic events which are associated to accretion onto the SMBH, where the chimneys could represent a chanel for the propagation of matter and energy to the regions above the disc (Ponti et al. 2019).

5.4.3 Fermi Bubbles and the jet scenario

As refered previously about the location of the FB and its morphology, these structures suggest a large event of energy injection in the GC, which may be attributed to a nuclear starbust in the last $\sim$ 10 Myr or

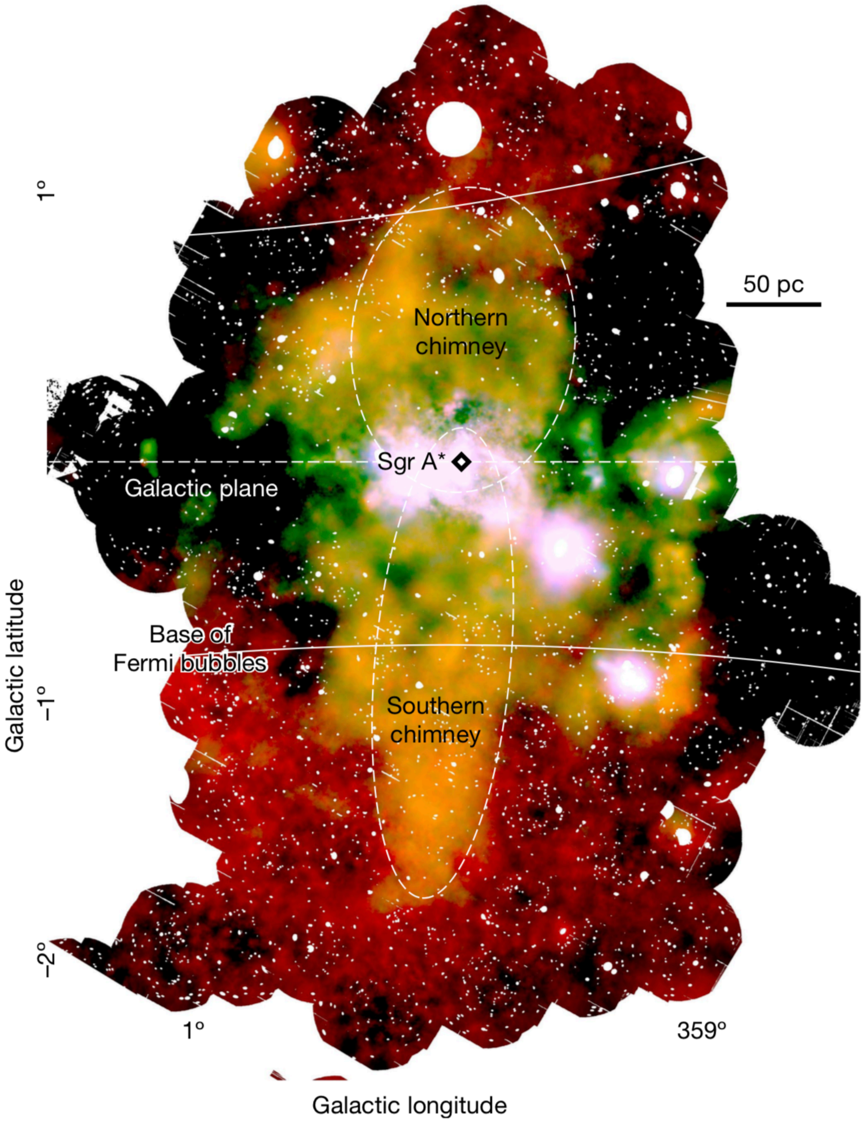

Figure 5.8: The bipolar lobes observed on the X-ray emission from the central region of the Milky Way (Ponti et al. 2019).

some previous accretion event onto the SMBH with energy release in the form of an outflow (Yang et al. 2012), where the relativistic jet scenarios are plausible to occur.

Relativistic jets can be originated from past activity in the GC. These jets can accelerate CRs to higher energies and thus contribute for the γ ray emission. As observed before, the FB present a hard spectrum which implies the CRs to travel from their origin to the FB location where these are effectively observed (Yang et al. 2012). Considering the IC scattering as the primary mechanism for the γ ray emission by CR electrons with energies between $10 \lesssim E_{CR} \lesssim 100$ GeV, then the FB age can be characterized by the IC cooling time with ~ 100 GeV electrons, which give an estimate time of a few Myr (Su et al. 2010).

The transport of CRs from their origin to distances of several kpc, must be very fast. Its transport velocity is given by (Yang et al. 2012)

$$v_{transport} \approx 10^4 \left(\frac{l}{10\ \mathrm{kpc}}\right) \left(\frac{t_{age}}{1\ \mathrm{Myr}}\right)^{-1} \mathrm{kms}^{-1} \tag{5.12}$$

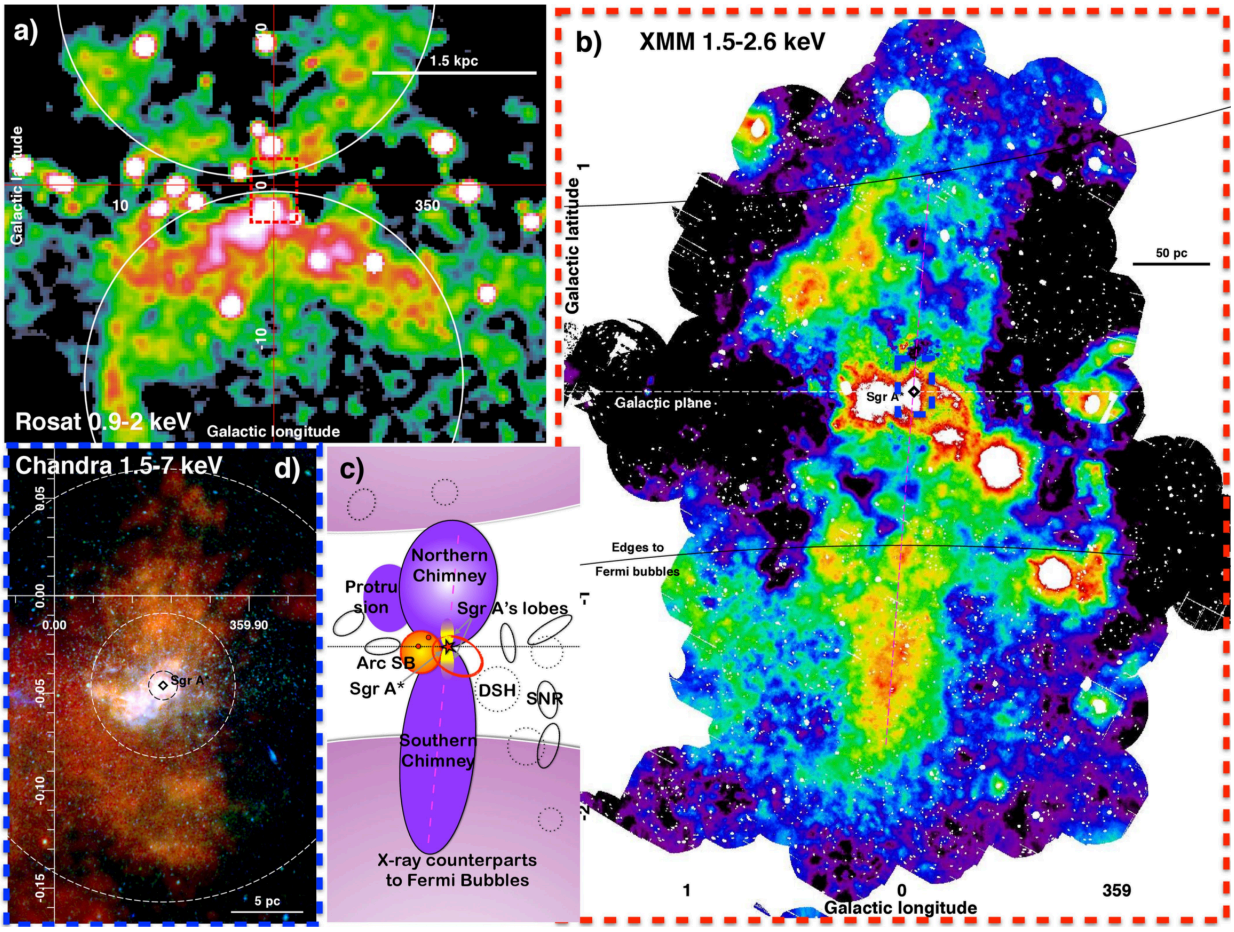

Figure 5.9: The X-ray emission at different scales in the GC. a) represents the ROSAT X-ray large-scale map of the GC; b) the XMM-Newton map of the central degrees of the Milky Way; c) a representation of the diffuse X-ray emitting features of the central 500 pc from gr A*and d) the Chandra RGB map of the central tens of parsecs of the Milky Way (Ponti et al. 2019). of the Galactic Centre

where l is the length and t_{age} the age of the FB.

Considering the scenario for the formation of the FB from relativistic jets Guo and Mathews (2012) implemented hydrodynamic numerical simulations where it was determined that relativistic jets can transport efficiently CRs to a few kpc in a time frame of $\sim$ 1-3 Myr. However they found some differences between their simulations and the observed FB. The simulated bubbles structure present hydrodynamic instabilities that produce spiral structures on the sides of the bubbles against the smoother surface from observations. It was also demonstrated that for the bubbles edges to be sharp it would imply that the CR diffusion could not occur on the bubbles surface because the CRs diffuse in an isotropic way and the bubbles edges should be smoother, with typical galactic coefficients (Guo and Mathews 2012; Yang et al. 2012).

The stellar disruption of a star by a SMBH occurs when the tidal forces of the black hole overcome the self-gravity of the star, which occurs when the R_P lies inside R_T (Rees 1988). When disruption occurs it unbinds $\sim 1/2$ of the stellar debris (Rees 1988) and the rest of the stellar mass describes eccentric orbits Evans and Kochanek (1989). The most bound debris will fallback onto the SMBH and it will collide and shock as it intersects itself, circularizing and being accreted by the black hole Kochanek (1994). As the accretion rate finds its peak at $t \sim t_{fb}$ it will decrease as $\dot{M} \propto t^{-5/3}$ with $\dot{M}$ given by (2.26).

One consequence of accretion by black holes is the relativistic outflows (Yang et al. 2012). There is a substantial fraction of the power from accretion that is transfered to the relativistic jet (Ghisellini et al. 2009; Yang et al. 2012).

Jets that are formed from SMBHs occur when the accretion rate is $\dot{M} \propto t^{-5/3}$ and decreases to $\lesssim 0.03\dot{M}_{Edd} \equiv \dot{M}_t$ for times $\gtrsim 10t_{Edd}$ (Yang et al. 2012). With such low accretion rate the accretion disc that forms (considering the relativistic effects, which are beyond the scope of this work) is expected to be radiatively inefficient (Narayan and Yi 1995; Blandford and Begelman 1999).

Considering that an accretion disc is formed around the SMBH after a TDE, due essentially to the apsidal precession of the stellar debris that self-intersects, collide and shock (Bonnerot et al. 2016), the penetration parameter should lie between $b = [1, 5]$, otherwise with $b \geq 5$ the stellar debris will be greatly swallowed (Guillochon and Ramirez-Ruiz 2013; Guillochon et al. 2009). After its formation the accretion disc can loose its angular momentum through magnetic stresses and it will infall onto the SMBH. With a specific angular momentum $\geq 2R_{SC}$ this infall will stop due to the centrifugal barrier where the pressure and density increase much and will accelerate the disc plasma in the vertical direction (zz) (Koide et al. 1999; Kudoh et al. 2002). If no magnetic fields are applied the accretion disc will fall into the compact object but when the magnetic field is strong enough there will occur the ejection of the debris of the accretion disc on the form of a collimated jet by the magnetic field and a fraction will turn into a fast jet due to the combined acceleration between the gas pressure and the magnetic forces, forming the better known *pressure-driven jet* (Koide et al. 1999; Blandford and Payne 1982). The region outside this pressure-driven jet is known to be the *magnetically driven jet* if the plasma is accelerated by the magnetic forces and so it can be considered that the jet presents a two layered structure where the most inner part is accelerated by the gas pressure and the outer part where it is magnetically accelerated (Koide et al. 1999).

These type of relativistic jets originated from black holes are thought to transport the magnetic field as it represents an important part in the jet collimation[3] and its acceleration (Appl and Camenzind 1993).

The FB morphology presents a bilobular structure which suggests that the CRs in the bubbles may not be formed from the diffused initial CRs driven and accelerated by SN shocks in the GC. These type of CRs should form a single CR bubble instead of two symmetric ones at the GC and also the sharp edges of the FB would consequently imply that across the bubbles surface the diffusion would be very much supressed (Guo and Mathews 2012).

The large event of energy injection scenario in the GC might be responsible for the formation of the FB as pointed by Su et al. (2010). A possible contribution for this is the relativistic jet scenario resultant from past activity in the GC. These jets are known to transport high energy CRs, already detected from radio synchrotron emission and even observed creating CR-filled bubbles (Laing et al. 2006).

The bubbles can be observed in the Fermi maps at $1 \lesssim E_\gamma \lesssim 100$ GeV, considering that the γ rays are due to IC scattering (Guo and Mathews 2012). These CR electrons have an IC cooling time of $\sim 10^6$ yr (Su et al. 2010) and due to the age and symmetry of the bubbles these might have a common origin. One important issue pointed by Guo and Mathews (2012) refers to the turbulence being triggered in both bubbles at the approximate same time, as the two structures are quite large ($\sim$ 10 kpc). If CRs could be originated by a single event and carried to the FB, then it would be plausible that the CRs could share the same intermediate point of origin, the GC (Yang et al. 2012).

It is known that the CR particles attain velocities near the speed of light but if these are colectively transported, their speed in the galaxy is considerably smaller (Zirakashvili 2014). Such decrease in the speed of CRs might be due to the magnetic irregularities that scatter the CRs. If this scattering is big enough, then the CRs will be trapped and move with the magnetic irregularities. In this case CRs can be advected with the thermal gas and so the CRs transport is called *advection* (Guo and Mathews 2012).

Another consideration besides advection is that CR may diffuse through the thermal gas where magnetic inhomogeneities are scattered off. The diffusion of CRs is measured by the diffusion coefficient k that depends on the magnetic field structure and the energy of CR. For a 1 GeV CRs the diffusion coefficient has values of $k \sim (3-5) \times 10^{28}$ cm^2 s^{-1} (Strong et al. 2010). If CRs in the bubbles are originated in the GC, these must be carried very quickly with a speed of $v_{transport} \sim 10\mathrm{kpc}/t_{age} \sim 10^4 (t_{age}/10^6 yr)^{-1}$ km s^{-1} to produce the structures of the bubbles (Guo and Mathews 2012).

---

[3] To narrow a beam of particles or waves

The FB should have an age of a few 10^6 yr because of the small IC cooling times of CR emissions that produce the detected γ ray emission. The principal mechanism of CR transport should not be diffusion because in this case it would form one single γ ray bubble centered at the GC. To carry CRs by diffusion to a distance of $l \sim 10$ kpc in the time t_{age} of the FB, the diffusion coefficient should be $k \sim l^2/t_{age} \sim 3 \times 10^{31}(t_{age}/10^6 yr)^{-1}$ cm^2 s^{-1}, which is about three orders of magnitude higher in respect to typical CR diffusivity in the galaxy (Mulcahy et al. 2016). Another fact about diffusion is that it tends to develop blurred boundaries instead of the sharp edges in γ ray for the observed FB (Attallah 2016).

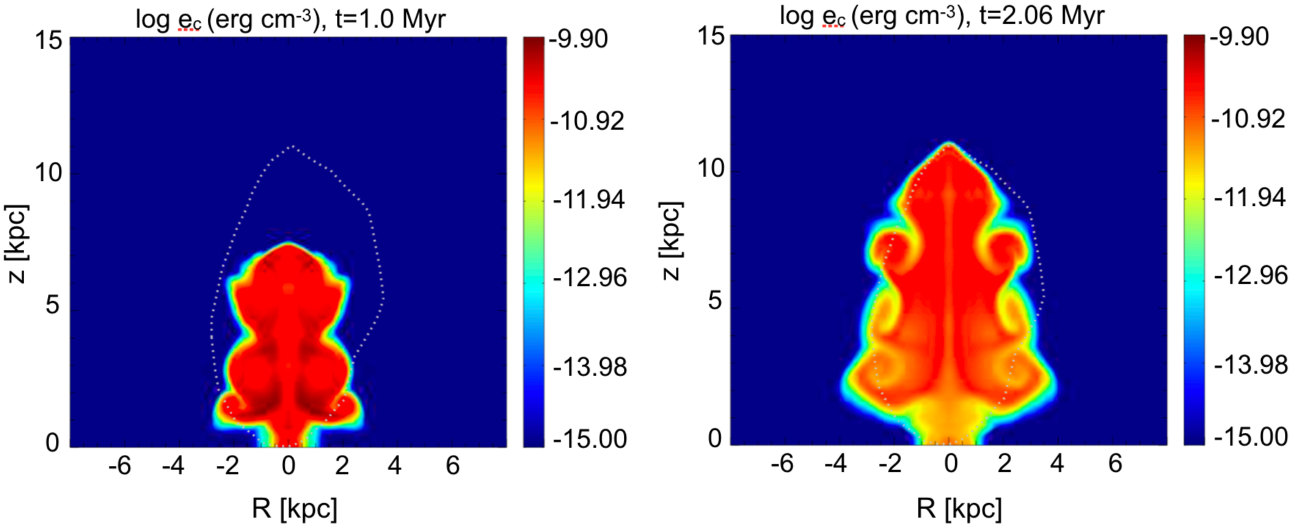

Figure 5.10: The CR energy density at times $t = 1.0$ Myr and $t = 2.06$ Myr for a propagation time of the jet of $t_{jet} = 0.3$ Myr. The dotted regions represent the enclose the observed northern FB. R and z are respectively the radius and vertical component in kpc (Guo and Mathews 2012).

The main transport mechanim of CRs from the GC to the FB cannot be diffusion and so the alternative mechanism should lie on advection of CRs with the thermal gas (Yang et al. 2012). Relativistic jets can transport CRs which can attain sub-relativistic or relativistic velocities on pc and kpc scales and so these will propagate much faster then galactic winds (Guo and Mathews 2012). These authors implemented numerical simulations to adress the issue of the FB formation due to CR transport by jets in the GC, with the focus on the morphology and dynamical evolution of the FB.

In Figure 5.10 the evolution of CR density (left panel) from $t = 1$ Myr to $t = 2.06$ Myr is shown. The thermal electron number density evolution is shown in Figure 5.11 for the same time interval. It can be observed that the jet expands rapidly producing a CR bubble that is similar to the actual north FB that is observed at $t = 2.06$ Myr.

It is implied that the transport of CR is dominated by advection as the jet results from the high velocities of the thermal gas. The low diffusivity parameter $k = 3 \times 10^{27}$ cm^2 s^{-1} for the CR diffusivity plays a very small effect as the sharp edges of the CR bubble show, which represents an important feature in the observed FB (Guo and Mathews 2012).

The high internal pressure in the bubbles can explain the lateral expansion that can be the result of both the CRs and the shocked thermal gas associated to a fast decrease of the ambient gas pressure with distance to the GC. With lower internal preessure the initial jet should be much narrow and the expansion of the gas density is much lower inside the bubbles, as shown in Figure 5.11. This way the X-ray cavities that are observed, towards the center of the FB, from ROSAT X-ray can be explained (Guo and Mathews 2012). Figure 5.12 shows the thermal electron number density at $t = t_{Fermi}$ (t_{Fermi} corresponds to the time at which the FB are observed) where the dashed line indicates the outer edge of the ROSAT X-ray emission

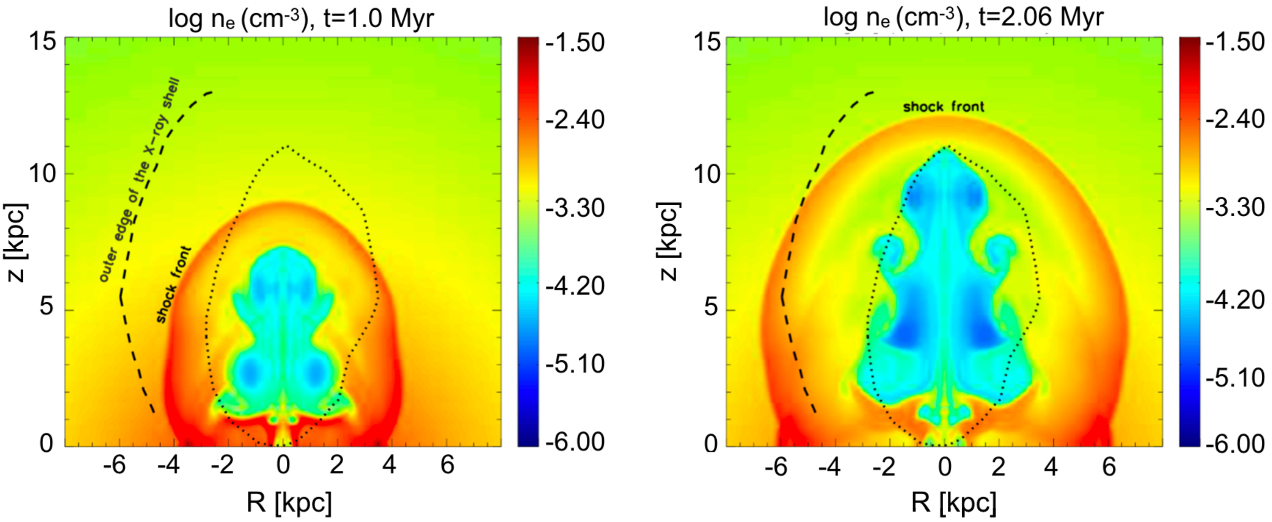

Figure 5.11: The CR thermal electron number density at times $t = 1.0$ Myr and $t = 2.06$ Myr for a propagation time of the jet of $t_{jet} = 0.3$ Myr. The dotted regions represent the enclose the observed northern FB. The dashed lines represent the ROSAT X-ray shell feature. R and z are respectively the radius and vertical component in kpc (Guo and Mathews 2012).

of the northern FB. The latter authors found a good matching between their model and the observed FB, even with varying jet parameters and also fiind that their simulations reproduce the CR bubbles with a similar match when compared to the observed FB.

The CRs can be accelerated to very high energies near the SMBH, considering the jet scenario. The time considered for the CR bubbles to be filled is a few Myr with a time of the jet propagation of $t_{jet} = 0.3$ Myr. The age of the FB can be inferred from the γ ray emission being dominated by IC emission of electron CRs (Dobler et al. 2010; Su et al. 2010) which allow the acceleration and transport of CRs through the $\sim$ 10 kpc FB length. The FB present a bilobular morphology with the symmetry in respect to the GC, which can also be explained by jet event in two opposite directions.

With the jet duration of $t_{jet} = 0.3$ Myr which is much shorter then the FB age it can suggest that the CRs have about the same age at present time through the whole bubbles. This can justify the fact that the γ ray spectral index must be uniform along a considerable region within the FB. The ROSAT X-ray shell features that surround the bubbles can be explained by the strong shocks from jets that heat and compress the surrounding gas in the galactic halo.
Finally, the FB expansion may be due to CR advection that can explain the sharp edges of the observed FB and where the CR diffusion is highly supressed (Guo and Mathews 2012).

5.5 Summary

The resident SMBH in the center of the Milky Way presents strong evidences in terms of its nature and its position has been accurately determined. Its mass has been also determined with good accuracy from stellar orbits, in fact it is the most well determined compact object to present. The SMBH mass is highly associated to the compact radio source Sgr A*, which is located in the GC and presents no proper motion - typical for a massive compact object. The radio polarization observations and X-ray imaging has allowed to constrain the accretion rate onto the Sgr A*, which has a low bolometric luminosity and presents a *cut-off* in the submm (THz) waves that support the existence of the event horizon. The radio emitting region gets smaller with the increase of the frequency and attains event horizon scales for frequencies $\simeq$ 230 GHz (from radio interferometric measurements).

The *quasi-symmetric* bubbles detected north and south of Sgr A* at the GC are still enshrouded by

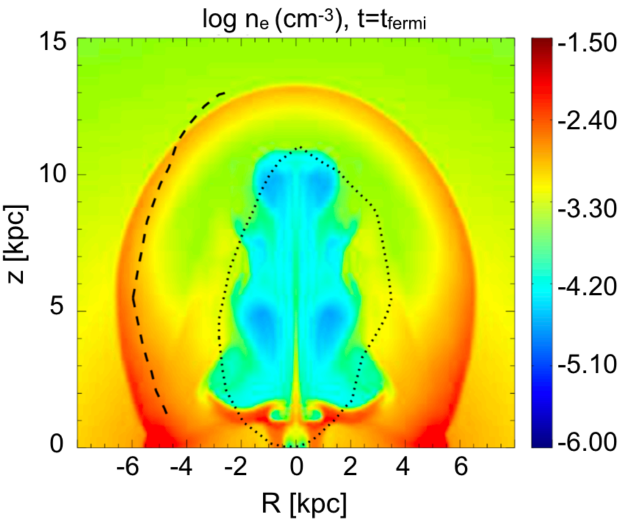

Figure 5.12: The CR thermal electron number density at time $t = t_{Fermi}$ for a propagation time of the jet of $t_{jet} = 0.3$ Myr. The dotted regions represent the enclose the observed northern FB. The dashed lines represent the ROSAT X-ray shell feature. R and z are respectively the radius and vertical component in kpc (Guo and Mathews 2012).

some uncertainty related to their origin. The contributions from some past activity at the GC such as SNe or TDEs are good candidates for the formation of such structures. More accurate suggestions were brought to discussion on this subject. The northern lobe presents a sharp and bright edge which can be associated to a shock, probably a SNR. The two lobes can also be the result of an outflow due to: i) winds from young stars originated from the GC cluster, ii) accretion flow onto Sgr A* by winds and iii) an X-ray generating process. Some features (south-west) of Sgr A* suggest that the soft X-ray can be some shell-like structure presenting thermal energy $E_{th} \sim 10 \times 10^{51}$ erg which makes such feature a superbubble candidate at the GC or it may represent a remnant structure of a TDE, due to its high energy. The GCL may be a structure with enhanced soft X-ray emission and might correspond to the base of larger structures, such as the Fermi Bubbles (Ponti et al. 2015).

In a more recent work and on the sight of new data from the XMM-Newton satellite, there were detected two bilobular lobes extending to approximately 15 pc above and below the GC and refered to as the northern and southern chimneys, which seem to share the same origin, the GC. From this latest developments Ponti et al. (2019) casts the hypothesis for the 160 pc chimneys and $\sim$ 15 pc bipolar lobes to be parts of an outflow that has its origin very close to the center of the galaxy near Sgr A*. Due to the energetics involved related to the chimneys there is the chance that the energy release might be explained by a SNe justifying the distribution of massive stars in the GC. Another hypothesis is related to TDEs as the very energetic events related to the disruption of stars associated to large accretion episodes onto the SMBH find in the chimneys structures a channel for the propagation of matter and energy to the surrounding areas of the GC Ponti et al. (2019).

Past activity in the GC like energy injection episodes associated to high accretion rates onto the SMBH or even nuclear starbust events in the last $\sim$ 10 Myr might have contributed to the formation of the large structures detected at the GC and known as the Fermi Bubbles (FB). The energy release from accretion events from the central black hole are thought to produce outflows from the GC which may develop other phenomena like relativistic jets (Yang et al. 2012).

The relativistic jet scenario can be interpreted as a consequence of accretion episodes from the SMBH where the power from accretion can be substantially transfered to the relativistic jet (Ghisellini et al. 2009). After a TDE and if relativity is to play a role on the accretion process, this fact may contribute to the formation of an accretion disc around the SMBH due to the circularization stellar debris that remains bound to it. An important relativistic effect is the apsidal precession of the stellar debris that implies the material to self intersect between the incoming debris and the outgoing one, which will collide and shock. These shocks can release large amounts of energy (e.g., thermal energy). After the formation of the accretion disc and if no magnetic fields develop influence the accretion disc will collapse into the SMBH but if the magnetic fields are strong enough the stellar debris that circularizes around the black hole will be ejected on the form of a collimated jet by the magnetic field (Koide et al. 1999).

The principal mechanism to transport CRs from the GC to the FB must be due to advection of CRs that are carried with the thermal gas (Yang et al. 2012). Relativistic jets can accelerate efficiently the CRs to very high energies with sub-relativistic or relativistic velocities on pc and kpc scales. The CR bubbles can be replenished in a few Myr considering a certain time of duration of the relativistic jet (as shown in the hydrodynamical numerical simulations of Guo and Mathews (2012)) and the age of the FB can be estimated from the γ ray emission which is dominated by the IC emission of electron CRs (Dobler et al. 2010; Su et al. 2010) that accelerate and transport the CRs for the $\sim$ 10 kpc FB. The observed FB structures may be the result of CR advection that can explain its sharp edges and where the CR diffusion is highly supressed (Guo and Mathews 2012).

6

Final remarks and future work

6.1 Summary of the thesis contents

The research described in this thesis born from the need to describe the formation and evolution of the Fermi Bubbles as its origin may be linked to the captures of stars by the black hole Sgr A* releasing at least 10^{53} erg of energy per capture. Hence, 100 captures are needed to comply with the energy of 10^{55} erg determined for the FB. Another option is the explosion of 10^4 massive stars (m$> 8\,\mathrm{M}_\odot$ with an energy release of 10^{51} erg (the canonical value). However, such hypothesis is unlikely as there is no evidence of such large activity that would leave an imprint in the soft X-ray emission from the Galactic center and the central molecular zone as shown in the high-resolution X-ray surveys of these areas by Ponti et al. (2015) and Ponti et al. (2019).

The most relevant theoretical aspects concerning TDEs were presented along Chapter 2, where the influence of Sgr A* over the surrounding stars and their orbits on the central region of the galaxy can determine the fate of the stars when they enter on the sphere of influence of the black hole. Such influence is presented within the loss cone theory focused to the relevant aspects to TDEs. The approach of a solar type star to an SMBH and the effects that it suffers under the influence of its tidal forces leads to the deformation and disruption of the star. Such effects are determined by the penetration parameter (b) during the pancake phase. After a TDE the material that is removed from the stellar surface is described in terms of its dynamics - most evident effect is the formation of two tidal tails with each portion evolving in different ways: one part of the stellar debris stays bound to the black hole and the other is ejected on hyperbolic trajectories. The accretion disc that forms around the black hole constitutes a strong mechanism of dissipation of energy of the orbiting stellar debris whose emission can be traced using different space telescopes (e.g., XMM-Newton, Suzaku, Nustar).

A detailed study of TDEs is only possible through the use of a Smoothed Particle Hydrodynamics (SPH), such as the Phantom code Price et al. (2017) whose description and tests (and comparison with the results obtained with the Zeus-MP (Hayes et al. 2006) code) are presented in Chapter 3. Phantom treats the fluid equations with discrete particles that are used with hydrodynamic properties and their evaluation is carried out at particle positions from weighted average values on other particles. The method is implicitly adaptive and is well suited to deal with vacuum boundary conditions and large regions that are devoid of gas (particles).

Chapter 4 deals with the details and results of the parametric (penetration parameter b and eccentricity ecc) study of TDEs where a solar mass star describes parabolic and elliptic trajectories around Sgr A* ($M_{BH} \sim 4 \times 10^6 M_\odot$) in the keplerian regime. The spatial distribution of the debris that results after the passage of the star at R_P, evolves in different fashion among the two types of trajectories:

i) Parabolic trajectories: For $ecc = 1$) the passage of the star at R_P causes deformation of its structure due to the tidal forces exerted by the black hole (depending on b) and resulting in the formation of two tidal tails produced by the debris that is depleted from the stellar surface (the least bound material of the star). Approximately half of the stellar debris removed from the star is ejected, while the rest is accreted by the black hole at a fallback rate.
The encounters with $b = 0.5$ and $b = 1$ are characterized by small deformation as the tidal forces exerted on the stellar surface are small. Hence, the star can keep its core unperturbed or with a few percent perturbation. For $b \geq 2$ encounters the star is gradually deformed with its core being stretched with increasing b, until the binding energy of the star no longer balances the tidal forces of the black hole. Consequently the star is partially or completely disrupted (*pancake phase*).

ii) Elliptic tractories: The spatial distribution of the debris is characterized by the circularization of the debris resultant from the crossing of the star at R_P. As the orbits have an eccentricity of $ecc = 0.3$, the resultant debris from the tidal disruption will settle in a near circular orbit. After a few P_* the debris will settle around the black hole, though the mass of the star is continuously removed and the stellar core is progressively deformed until disruption occurs. The consecutive passages of the star at R_P will produce a stream of debris that describes near circular orbits until it starts to be accreted, after several orbital periods. The debris that attains enough angular momentum and do not fall into the black hole will settle on a circularization radius defined by the specific circularization energy resultant from the debris that is redistributed.

The debris that returns to the SMBH is characterized by the peak of the mass fallback rate. The Milky Way's SMBH is $\approx 4 \times 10^6 M_\odot$ which gives a fallback time of $t_{fb} = 7.077 \times 10^6$ s $\approx$ 82 days. The return of the debris to the black hole is estimated by the peak of the fallback mass rate $\dot{M} \simeq 3 M_\odot$ yr^{-1}.

By the passage at R_P the star will have a kinetic energy of the order of $(M_{BH}/M_*)^{2/3}$ and will be distorted and compressed due to tidal forces in a way that thermal energy will be released and will be imparted to the resultant debris at the expense of the kinetic energy. The gravitational binding energy of the gas to the SMBH will be converted in thermal energy until it reaches the last stable orbit around the black hole.

If the gas can dissipate the heat by the emission of radiation or acceleration of particles, then the thermal energy can be extracted by the time it reaches the last stable orbit. If the dissipation of energy is inefficient, the heat can be advected onto the SMBH where it will be added to its rest mass (Rees 1988; Alexander 2005).

Due to the tidal forces of the black hole the kinetic energy is imparted into thermal energy, which is released for the surrounding medium. The thermal energy released can be of the order $\sim 10^{47}$ erg for the $b = 0.5$ encounter in both parabolic and elliptic TDEs and can go up to $\sim 10^{50}$ erg for the highest $b = 8$ encounters for the parabolic case and of the order $\sim 10^{48}$ erg for the elliptic case.

The results obtained from the simulations show that the parabolic TDEs release more thermal energy than the elliptic TDES by the first passage of the star at R_P.

Chapter 5 deals with the most important characteristics of Sgr A* including the latest X-ray observations and the presence of two lobes and chimneys on either side of the Galactic Center associated to activity near or in the Sgr A*. The Fermi Bubbles origin is described taking into account the jet scenario.

The SMBH Sgr A* presents strong evidences in terms of its nature with an accurate determined position in the GC. Its mass is well determined from stellar orbits and in fact it is the most well determined compact object to date. The mass of the central black hole is highly associated to the compact radio source Sgr A* located at the GC and presents no proper motion. Observations of radio polarization and X-ray imaging have constrained the accretion rate onto the Sgr A* that has a low bolometric luminosity with a *cut-off* in the submm (THz) waves confirming the existence of the event horizon.

The *quasi-symmetric* lobes detected north and south of Sgr A* at the GC still cast doubts related to their origin. The contributions from some past activity at the GC such as SNe or TDEs might have contributed for the formation of such structures. The lobes can be the result of an outflow due to winds from young stars originated from the GC, an accretion flow onto Sgr A* or an X-ray generating process. Some features suggest that the soft X-ray might be attributed to a shell-like structure presenting thermal energy $E_{th} \sim 10 \times 10^{51}$ erg turning it potentially in a superbubble candidate at the GC or it may be a remnant structure of a TDE, due to its high energy. The GCL may be a structure with enhanced soft X-ray emission and might correspond to the base of larger structures, such as the Fermi Bubbles (Ponti et al. 2015).

Recent data from the XMM-Newton satellite detected two lobes that extend $\sim$ 15 pc above and below the GC which are designated by the northern and southern chimneys and apparently share the same origin which is the GC. This more recent developments Ponti et al. (2019) unveil the hypothesis for the chimneys and the bipolar lobes to be parts of an outflow with origin very close to the center of the galaxy near Sgr A*. Due to the energetics involved the energy release might be explained by a SNe which explains the distribution of massive stars in the GC. TDEs might be another hypothesis as the very energetic events related to the disruption of stars are associated to large accretion episodes onto the SMBH finding in the chimneys a way to propagate the matter and energy to the surroundings of the GC (Ponti et al. 2019).

The past activity in the GC in the last $\sim$ 10 Myr might have contributed to form the large structures at the GC, known as the Fermi Bubbles (FB). Accretion events may contribute for the energy release from the central black hole which are thought to produce outflows from the GC and develop other phenomena like relativistic jets (Yang et al. 2012).

The jet scenario can be the consequence of accretion episodes from the SMBH and the energy resultant from the accretion process can be transfered to the relativistic jet (Ghisellini et al. 2009). After a TDE an accretion disc around the SMBH can be formed due to the circularization stellar debris that remains bound to it. Important relativistic effects like the apsidal precession of the stellar debris can release large amounts of energy (e.g., thermal energy). After the formation of the disc and if no magnetic fields develop influence the accretion disc will collapse into the SMBH. In the presence of strong magnetic fields the stellar debris that orbits around the black hole can be ejected on the form of a collimated jet by the magnetic field (Koide et al. 1999).

The main mechanism of CRs transport from the GC to the FB must be due to advection of CRs that are carried with the thermal gas (Yang et al. 2012). Relativistic jets can accelerate CRs to very high energies with sub-relativistic or relativistic velocities on pc and kpc scales. The CR bubbles can be filled in a few Myr according to the duration of the jet and the age of the FB can be estimated from the γ ray emission which is dominated by the IC emission of electron CRs (Dobler et al. 2010; Su et al. 2010) accelerating and transporting the CRs to the $\sim$ 10 kpc FB. CR advection can explain the observed FB due to its sharp edges and where the CR diffusion is highly supressed (Guo and Mathews 2012).

In a recent work Curd and Narayan (2019) studies the jetted TDEs with General Relativity Radiation MagnetoHydrodynamics (GRRMHD) which enlights new and important information on the complex process from the initial TDEs to the formation of accretion disc and relativistic jets.

6.2 Future work

The work presented in this thesis is just the beginning of a long research program to carry out in the next few years. This program comprises four lines of work:

(a) Inclusion of relativistic effects. These effects are important for the circularization of debris and the formation/evolution of the accretion disc. The latter results from the settling of the debris under an accretion rate of the stellar matter onto the black hole. An accretion disc can form from the debris and is essentially driven by relativistic apsidal precession (another relativistic effect) that causes the stream to self-intersect, leading to shocks and therefore more energetic events to account for. The structure of the disc depends on the cooling efficiency of the gas by considering two extreme cases. If efficient cooling occurs, the debris will settle in a thin and narrow ring of gas but on the other way if the cooling is inefficient it will settle into a thick and extended torus.

(b) The smoking gun and the formation of the Fermi Bubbles. The recent X-ray emission observations by Ponti et al. (2015) and Ponti et al. (2019) show hot plasma moving away from the GC and forming chimneys. Their origin and evolution was the subject of intense studies over the last 30 years (see, e.g., review by de Avillez and Breitschwerdt (2010) and references therein). Knowing the amount of thermal energy released (and thus the heat up of the interstellar gas) by the TDE and their time of occurrence one needs to bring together high resolution simulations of the TDE evolution and the expansion of the hot plasma on either side of the GC by combining the SPH and adaptive mesh refinement grid simulations. Thus, tracing the formation of the superbubbles and their emission properties using the Collisional+Photo Ionization Plasma Emission Software (CPIPES; de Avillez and Breitschwerdt 2017; de Avillez 2018; de Avillez et al. 2018).

(c) Study of the emission properties of the accretion disk and corona. With CPIPES study the time dependent ionization structure and the emission processes in the accretion disk and corona. The latter is a high-energetic hot and optically thin region that reprocesses the thermal photons from the accretion disk. The corona emission feeds back into the accretion disk and thus its emission properties have to be traced jointly with a radiative transfer calculation. The emission spectra of the two regions is then passed through the X-ray telescope response matrices and be used to compare with real observations using the spectral fitting package XSPEC[1] and the KY relativistic accretion disk model package of (Dovčiak et al. 2004).

(d) Study of the vertical structure of the accretion disk in a consistent way with the radiation field. Taking into account the emission from the accretion disk and from the corona, which feedback into the dynamics of the accretion disk through the equation of state and momentum equation (see, e.g., Schmutzler and Tscharnuter (1993); de Avillez and Breitschwerdt (2012), carry out high-resolution multi-fluid simulations of the accretion disk using radiative transfer and taking into account the photons emitted from the different components and absorbed by the accretion disk. This is important as in general it is assumed that the accretion disk has a constant density atmosphere as this simplifies the energetic and emission calculations and simplifying radiative transfer calculations.

In summary we favour the formation of the Fermi Bubbles within a short period of time (not longer than 10 Myr) mainly due to captures of stars by the SMBH residing in the Sgr A* region. Supernova

---

[1] https://heasarc.gsfc.nasa.gov/xanadu/xspec

activity in the vicinity only contributed to energize the bubbles within a sound crossing time, preventing the plasma to cool and making difficult their detection.

The End

Bibliography

Alexander, T.: 2005, *Phys. Rep.* **419**, 65 1, 3, 4, 5, 6, 10, 63, 69, 76, 77, 92

Alexander, T. and Hopman, C.: 2003, *ApJ* **590**, L29 5

Appl, S. and Camenzind, M.: 1993, *A&A* **274**, 699 86

Attallah, R.: 2016, *Journal of Cosmology and Astroparticle Physics* **2016(12)**, 025 87

Ayal, S., Livio, M., and Piran, T.: 2000, *ApJ* **545**, 772 3, 4, 20, 59

Baganoff, F. K., Maeda, Y., Morris, M., Bautz, M. W., Brandt, W. N., Cui, W., Doty, J. P., Feigelson, E. D., Garmire, G. P., Pravdo, S. H., Ricker, G. R., and Townsley, L. K.: 2003, *ApJ* **591**, 891 72, 75

Balick, B. and Brown, R. L.: 1974, *ApJ* **194**, 265 1

Balsara, D. S.: 1998, *ApJS* **116**, 133 36

Barrière, N. M., Tomsick, J. A., Baganoff, F. K., Boggs, S. E., Christensen, F. E., Craig, W. W., Dexter, J., Grefenstette, B., Hailey, C. J., Harrison, F. A., Madsen, K. K., Mori, K., Stern, D., Zhang, W. W., Zhang, S., and Zoglauer, A.: 2014, *ApJ* **786**, 46 74

Belloni, M. and Robinett, R. W.: 2014, *Phys. Rep.* **540**, 25 26

Blandford, R. D. and Begelman, M. C.: 1999, *MNRAS* **303**, L1 86

Blandford, R. D. and Königl, A.: 1979, *ApJ* **232**, 34 78

Blandford, R. D. and Payne, D. G.: 1982, *MNRAS* **199**, 883 86

Bondi, H. and Hoyle, F.: 1944, *MNRAS* **104**, 273 75

Bonnerot, C., Price, D. J., Lodato, G., and Rossi, E. M.: 2017a, *MNRAS* **469**, 4879 19

Bonnerot, C., Rossi, E. M., and Lodato, G.: 2017b, *MNRAS* **464**, 2816 20

Bonnerot, C., Rossi, E. M., Lodato, G., and Price, D. J.: 2016, *MNRAS* **455**, 2253 5, 6, 14, 15, 20, 45, 56, 57, 86

Bower, G. C., Backer, D. C., Zhao, J.-H., Goss, M., and Falcke, H.: 1999, *ApJ* **521**, 582 75

Bower, G. C., Falcke, H., Herrnstein, R. M., Zhao, J.-H., Goss, W. M., and Backer, D. C.: 2004, *Science* **304**, 704 74

Bower, G. C., Falcke, H., Herrnstein, R. M., Zhao, J.-H., Goss, W. M., and Backer, D. C.: 2004, *Science* **304(5671)**, 704 78

Bower, G. C., Falcke, H., Wright, M. C. H., and Backer, D. C.: 2005, *The Astrophysical Journal Letters* **618(1)**, L29 75

Bower, G. C., Wright, M. C. H., Backer, D. C., and Falcke, H.: 1999, *The Astrophysical Journal* **527(2)**, 851 75, 77

Bremer, M., Witzel, G., Eckart, A., Zamaninasab, M., Buchholz, R. M., Schödel, R., Straubmeier, C., García-Marín, M., and Duschl, W.: 2011, *A&A* **532**, A26 74

Brio, M. and Wu, C.: 1988, **75**, 400 35, 36

Canizares, C. R., Davis, J. E., Dewey, D., Flanagan, K. A., Galton, E. B., Huenemoerder, D. P., Ishibashi, K., Markert, T. H., Marshall, H. L., McGuirk, M., Schattenburg, M. L., Schulz, N. S., Smith, H. I., and Wise, M.: 2005, *Publications of the Astronomical Society of the Pacific* **117(836)**, 1144 78

Cannizzo, J. K., Lee, H. M., and Goodman, J.: 1990, *ApJ* **351**, 38 5

Cavaliere, A. and Fusco-Femiano, R.: 1976, *A&A* **49**, 137 42

Chandrasekhar, S.: 1967, *An introduction to the study of stellar structure* 59

Chen, X., Gómez-Vargas, G. A., and Guillochon, J.: 2016, *MNRAS* **458**, 3314 79, 80

Cheng, K.-S., Chernyshov, D. O., Dogiel, V. A., Ko, C.-M., and Ip, W.-H.: 2011, *ApJ* **731**, L17 1, 2, 3, 9, 59, 79, 80

Cirnu, M. and Badralexi, I.: 1995, *Romanian Economic Business Review* **5**, 91 34

Clarke, J. N.: 1981, *Icarus* **46**, 94 77

Cohn, H. and Kulsrud, R. M.: 1978, *ApJ* **226**, 1087 12

Coker, R. F. and Melia, F.: 1997, *The Astrophysical Journal Letters* **488(2)**, L149 75

Cossins, P. J.: 2010, *Ph.D. thesis*, PhD Thesis, 2010 23, 24, 25, 26, 27

Couchman, H. M. P., Thomas, P. A., and Pearce, F. R.: 1995, *ApJ* **452**, 797 42

Coughlin, E. R.: 2016, *Ph.D. thesis*, University of Colorado at Boulder 15, 19, 49

Crocker, R. M., Fatuzzo, M., Jokipii, J. R., Melia, F., and Volkas, R. R.: 2005, *ApJ* **622**, 892 79

Curd, B. and Narayan, R.: 2019, *MNRAS* **483(1)**, 565 94

Dai, L., McKinney, J. C., and Miller, M. C.: 2015, *ApJ* **812**, L39 19

Dai, W. and Woodward, P. R.: 1994, *Journal of Plasma Physics* **51**, 381 35

Dai, W. and Woodward, P. R.: 1998, *The Astrophysical Journal* **494(1)**, 317 39

Davies, R. D., Walsh, D., and Booth, R. S.: 1976, *MNRAS* **177**, 319 74 de Avillez, M.: 2018, in *Cosmic Rays and the InterStellar Medium*, p. 28 94

de Avillez, M. A.: 2000, *MNRAS* **315**, 479 83

de Avillez, M. A., Anela, G. J., and Breitschwerdt, D.: 2018, *A&A* **616**, A58 94

de Avillez, M. A. and Breitschwerdt, D.: 2005, *A&A* **436**, 585 83

de Avillez, M. A. and Breitschwerdt, D.: 2010, in R. Kothes, T. L. Landecker, and A. G. Willis (eds.), *The Dynamic Interstellar Medium: A Celebration of the Canadian Galactic Plane Survey*, Vol. 438 of *Astronomical Society of the Pacific Conference Series*, p. 313 94

de Avillez, M. A. and Breitschwerdt, D.: 2012, *ApJ* **756**, L3 94

de Avillez, M. A. and Breitschwerdt, D.: 2017, *ApJS* **232**, 12 94

Dobler, G., Finkbeiner, D. P., Cholis, I., Slatyer, T., and Weiner, N.: 2010, *ApJ* **717(2)**, 825 88, 90, 93

Dodds-Eden, K., Porquet, D., Trap, G., Quataert, E., Haubois, X., Gillessen, S., Grosso, N., Pantin, E., Falcke, H., Rouan, D., Genzel, R., Hasinger, G., Goldwurm, A., Yusef-Zadeh, F., Clenet, Y., Trippe, S., Lagage, P. O., Bartko, H., Eisenhauer, F., Ott, T., Paumard, T., Perrin, G., Yuan, F., Fritz, T. K., and Mascetti, L.: 2009, *ApJ* **698**, 676 78

Dogiel, V., Cheng, K.-S., Chernyshov, D., Bamba, A., Ichimura, A., Inoue, H., Ko, C.-M., Kokubun, M., Maeda, Y., Mitsuda, K., and Yamasaki, N. Y.: 2009, *ArXiv e-prints* 5

Dovčiak, M., Karas, V., and Yaqoob, T.: 2004, *ApJS* **153**, 205 94

Eastwood, D. S. and Khochfar, S.: 2018, *MNRAS* **480**, 5673 51

Eatough, R. P., Falcke, H., Karuppusamy, R., Lee, K. J., Champion, D. J., Keane, E. F., Desvignes, G., Schnitzeler, D. H. F. M., Spitler, L. G., Kramer, M., Klein, B., Bassa, C., Bower, G. C., Brunthaler, A., Cognard, I., Deller, A. T., Demorest, P. B., Freire, P. C. C., Kraus, A., Lyne, A. G., Noutsos, A., Stappers, B., and Wex, N.: 2013, *Nature* **501**, 391 75

Eckart, A., Baganoff, F. K., Morris, M., Bautz, M. W., Brandt, W. N., Garmire, G. P., Genzel, R., Ott, T., Ricker, G. R., Straubmeier, C., Viehmann, T., Schödel, R., Bower, G. C., and Goldston, J. E.: 2004, *A&A* **427**, 1 78

Eckart, A. and Genzel, R.: 1996, *Nature* **383**, 415 72

Eddington, A. S.: 1926, *Nature* **117**, 25 17

Eisenhauer, F., Schödel, R., Genzel, R., Ott, T., Tecza, M., Abuter, R., Eckart, A., and Alexander, T.: 2003, *ApJ* **597**, L121 72

Ettori, S.: 2000, *MNRAS* **318(4)**, 1041 42

Evans, C. R. and Kochanek, C. S.: 1989, in *Bulletin of the American Astronomical Society*, Vol. 21 of *BAAS* , p. 1158 2, 4, 5, 6, 15, 16, 17, 45, 53, 85

Falcke, H., Goss, W. M., Matsuo, H., Teuben, P., Zhao, J.-H., and Zylka, R.: 1998, *The Astrophysical Journal* **499(2)**, 731 72

Falcke, H., Körding, E., and Markoff, S.: 2004, *A&A* **414**, 895 78

Falcke, H., Mannheim, K., and Biermann, P. L.: 1993, *A&A* **278**, L1 78

Falcke, H. and Markoff, S.: 2000, *A&A* **362**, 113 78

Falcke, H., Markoff, S., and Bower, G. C.: 2009, *A&A* **496**, 77 74, 75

Falcke, H., Markoff, S., Bower, G. C., Gammie, C. F., Mościbrodzka, M., and Maitra, D.: 2011, in G. E. Romero, R. A. Sunyaev, and T. Belloni (eds.), *Jets at All Scales*, Vol. 275 of *IAU Symposium*, pp 68–76 74

Falcke, H. and Markoff, S. B.: 2013, *Classical and Quantum Gravity* **30(24)**, 244003 73

Fatuzzo, M., Adams, F. C., and Melia, F.: 2006, *ApJ* **653**, L49 79

Fermi, E.: 1949, *Phys. Rev.* **75**, 1169 78

Ferrarese, L. and Merritt, D.: 2000, *ApJ* **539**, L9 6, 10

Frank, A., Jones, T. W., Ryu, D., and Gaalaas, J. B.: 1996, *ApJ* **460**, 777 40

Frank, J.: 1978, *MNRAS* **184**, 87 2

Frank, J. and Rees, M. J.: 1976, *MNRAS* **176**, 633 2, 5, 6, 10

Freitag, M. and Benz, W.: 2002, *A&A* **394**, 345 11

Geballe, T. R., Wade, R., Krisciunas, K., Gatley, I., and Bird, M. C.: 1987, *ApJ* **320**, 562 82

Genzel, R., Eisenhauer, F., and Gillessen, S.: 2010, *Reviews of Modern Physics* **82**, 3121 73

Genzel, R., Hollenbach, D., and Townes, C. H.: 1994, *Reports on Progress in Physics* **57**, 417 75

Genzel, R., Pichon, C., Eckart, A., Gerhard, O. E., and Ott, T.: 2000, *MNRAS* **317**, 348 72

Genzel, R., Schödel, R., Ott, T., Eckart, A., Alexander, T., Lacombe, F., Rouan, D., and Aschenbach, B.: 2003, *Nature* **425**, 934 74

Ghez, A. M., Klein, B. L., Morris, M., and Becklin, E. E.: 1998, *The Astrophysical Journal* **509(2)**, 678 72

Ghez, A. M., Morris, M., Becklin, E. E., Tanner, A., and Kremenek, T.: 2000, *Nature* **407**, 349 72

Ghez, A. M., Salim, S., Weinberg, N. N., Lu, J. R., Do, T., Dunn, J. K., Matthews, K., Morris, M. R., Yelda, S., Becklin, E. E., Kremenek, T., Milosavljevic, M., and Naiman, J.: 2008, *ApJ* **689**, 1044 72

Ghez, A. M., Wright, S. A., Matthews, K., Thompson, D., Le Mignant, D., Tanner, A., Hornstein, S. D., Morris, M., Becklin, E. E., and Soifer, B. T.: 2004, *ApJ* **601**, L159 74

Ghisellini, G., Maraschi, L., and Tavecchio, F.: 2009, *MNRAS* **396(1)**, L105 85, 89, 93

Gillessen, S., Eisenhauer, F., Fritz, T. K., Bartko, H., Dodds-Eden, K., Pfuhl, O., Ott, T., and Genzel, R.: 2009, *ApJ* **707**, L114 73

Gillessen, S., Eisenhauer, F., Trippe, S., Alexander, T., Genzel, R., Martins, F., and Ott, T.: 2009, *The Astrophysical Journal* **692(2)**, 1075 72

Gingold, R. A. and Monaghan, J. J.: 1977, *MNRAS* **181**, 375 6, 7, 23, 30, 31, 35

Guillochon, J., Loeb, A., MacLeod, M., and Ramirez-Ruiz, E.: 2014a, *ApJ* **786**, L12 51, 57, 60, 62

Guillochon, J., Manukian, H., and Ramirez-Ruiz, E.: 2014b, *ApJ* **783**, 23 3, 6, 16, 18, 19, 20, 60

Guillochon, J., McCourt, M., Chen, X., Johnson, M. D., and Berger, E.: 2016, *ApJ* **822**, 48 51, 58

Guillochon, J. and Ramirez-Ruiz, E.: 2013, *ApJ* **767**, 25 1, 3, 9, 15, 16, 47, 48, 49, 51, 67, 86

Guillochon, J. and Ramirez-Ruiz, E.: 2015, *ApJ* **809**, 166 14, 15, 51, 58

Guillochon, J., Ramirez-Ruiz, E., and Lin, D.: 2011, *ApJ* **732**, 74 45

Guillochon, J., Ramirez-Ruiz, E., Rosswog, S., and Kasen, D.: 2009, *ApJ* **705**, 844 47, 86

Guo, F. and Mathews, W. G.: 2012, *ApJ* **756(2)**, 181 2, 85, 86, 87, 88, 89, 90, 94

Haubois, X., Dodds-Eden, K., Weiss, A., Paumard, T., Perrin, G., Clénet, Y., Gillessen, S., Kervella, P., Eisenhauer, F., Genzel, R., and Rouan, D.: 2012, *A&A* **540**, A41 77

Hayasaki, K., Stone, N., and Loeb, A.: 2016, *MNRAS* **461**, 3760 14, 16, 20

Hayes, J. C., Norman, M. L., Fiedler, R. A., Bordner, J. O., Li, P. S., Clark, S. E., ud-Doula, A., and Mac Low, M.-M.: 2006, *ApJS* **165(1)**, 188 44, 92

Herant, M.: 1994, in *American Astronomical Society Meeting Abstracts*, Vol. 26 of *Bulletin of the American Astronomical Society*, p. 1357 34

Hills, J. G.: 1975, *Nature* **254**, 295 2, 3

Hinton, J. A. and Hofmann, W.: 2009, *Annual Review of Astronomy and Astrophysics* **47**, 523 79

Hjellming, M. S. and Webbink, R. F.: 1987, *ApJ* **318**, 794 51, 68

Jiang, Y.-F., Guillochon, J., and Loeb, A.: 2016, *ApJ* **830**, 125 61

Kaufmann, T., Mayer, L., Wadsley, J., Stadel, J., and Moore, B.: 2007, *MNRAS* **375(1)**, 53 42

Khokhlov, A. and Melia, F.: 1996, *The Astrophysical Journal Letters* **457(2)**, L61 60

Kochanek, C. S.: 1994, *ApJ* **422**, 508 4, 45, 85

Kocsis, B. and Loeb, A.: 2014, *Space Science Reviews* **183(1)**, 163 16

Koide, S., Shibata, K., and Kudoh, T.: 1999, *The Astrophysical Journal* **522(2)**, 727 86, 90, 93

Kozlowski, M., Jaroszynski, M., and Abramowicz, M. A.: 1978, *A&A* **63**, 209 59

Kudoh, T., Matsumoto, R., and Shibata, K.: 2002, *PASJ* **54**, 267 86

Kuijken, K. and Dubinski, J.: 1995, *MNRAS* **277**, 1341 42

Lacy, J. H., Baas, F., Townes, C. H., and Geballe, T. R.: 1979, *ApJ* **227**, L17 72

Lacy, J. H., Townes, C. H., and Hollenbach, D. J.: 1982, *ApJ* **262**, 120 5, 6

Laing, R. A., Canvin, J. R., Bridle, A. H., and Hardcastle, M. J.: 2006, *MNRAS* **372**, 510 86

Langer, N., Sanyal, D., Grassitelli, L., and Szésci, D.: 2015, in W.-R. Hamann, A. Sander, and H. Todt (eds.), *Wolf-Rayet Stars: Proceedings of an International Workshop held in Potsdam, Germany, 1-5 June 2015. Edited by Wolf-Rainer Hamann, Andreas Sander, Helge Todt. Universitätsverlag Potsdam, 2015., p.241-244*, pp 241–244 17, 18

Law, C. J., Brentjens, M. A., and Novak, G.: 2011, *The Astrophysical Journal* **731(1)**, 36 82

Lightman, A. P. and Shapiro, S. L.: 1977, *ApJ* **211**, 244 2, 3, 12

Liu, S., Petrosian, V., and Melia, F.: 2004, *The Astrophysical Journal Letters* **611(2)**, L101 78

Liu, S., Petrosian, V., and Melia, F.: 2004, *ApJ* **611**, L101 78

Lo, K. Y., Backer, D. C., Ekers, R. D., Kellermann, K. I., Reid, M., and Moran, J. M.: 1985, *Nature* **315**, 124 74

Lo, K. Y., Shen, Z.-Q., Zhao, J.-H., and Ho, P. T. P.: 1998, *The Astrophysical Journal Letters* **508(1)**, L61 74

Lodato, G.: 2012, in *European Physical Journal Web of Conferences*, Vol. 39 of *European Physical Journal Web of Conferences*, p. 01001 20

Lodato, G., Franchini, A., Bonnerot, C., and Rossi, E. M.: 2015, *Journal of High Energy Astrophysics* **7**, 158 16

Lodato, G. and Rossi, E. M.: 2011, *MNRAS* **410**, 359 18

Loeb, A. and Ulmer, A.: 1997, *ApJ* **489**, 573 4, 17

Lucy, L. B.: 1977, *AJ* **82**, 1013 6, 23

Luminet, J.-P. and Barbuy, B.: 1990, *AJ* **99**, 838 49, 56, 60

Lynden-Bell, D. and Rees, M. J.: 1971, *MNRAS* **152**, 461 72

Macquart, J.-P., Bower, G. C., Wright, M. C. H., Backer, D. C., and Falcke, H.: 2006, *ApJ* **646**, L111 75

Magorrian, J. and Tremaine, S.: 1999, *MNRAS* **309**, 447 2, 5, 17, 46

Mainetti, D., Lupi, A., Campana, S., Colpi, M., Coughlin, E. R., Guillochon, J., and Ramirez-Ruiz, E.: 2017, *A&A* **600**, A124 16, 49

Maitra, D., Markoff, S., and Falcke, H.: 2009, *A&A* **508**, L13 74

Markoff, S.: 2010, *Proceedings of the National Academy of Sciences* **107(16)**, 7196 81

Markoff, S., Bower, G. C., and Falcke, H.: 2007, *MNRAS* **379**, 1519 78

Markoff, S., Falcke, H., Yuan, F., and Biermann, P. L.: 2001, *A&A* **379**, L13 78

Marrone, D. P., Moran, J. M., Zhao, J.-H., and Rao, R.: 2006, *The Astrophysical Journal* **640(1)**, 308 75

Melia, F.: 1992, *ApJ* **387**, L25 75

Menou, K. and Quataert, E.: 2001, *ApJ* **562**, L137 5

Menten, K. M., Reid, M. J., Eckart, A., and Genzel, R.: 1997, *ApJ* **475**, L111 72

Merloni, A., Heinz, S., and di Matteo, T.: 2003, *MNRAS* **345**, 1057 78

Merritt, D.: 2010, *ApJ* **718**, 739 11, 13

Merritt, D.: 2013, *Classical and Quantum Gravity* **30(24)**, 244005 10

Metzger, B. D. and Stone, N. C.: 2016, *MNRAS* **461**, 948 20

Mezger, P. G., Zylka, R., Salter, C. J., Wink, J. E., Chini, R., Kreysa, E., and Tuffs, R.: 1989, *A&A* **209**, 337 72

Miller, A. A.: 2015, *VizieR Online Data Catalog* 181 18

Monaghan, J.: 1997, *Journal of Computational Physics* **136(2)**, 298 23

Monaghan, J. J.: 1992, *ARA&A* **30**, 543 7, 25, 27, 29, 30

Monaghan, J. J.: 2005, *Reports on Progress in Physics* **68**, 1703 23

Monaghan, J. J. and Lattanzio, J. C.: 1985, *A&A* **149**, 135 28, 29, 30

Monaghan, J. J. and Price, D. J.: 2005, *Monthly Notices of the Royal Astronomical Society* **364(2)**, 384 41

Morris, M., Baganoff, F., Muno, M., Howard, C., Maeda, Y., Feigelson, E., Bautz, M., Brandt, N., Chartas, G., Garmire, G., and Townsley, L.: 2003, *Astronomische Nachrichten Supplement* **324**, 167 81

Morris, M. and Serabyn, E.: 1996, *ARA&A* **34**, 645 81

Mulcahy, D. D., Fletcher, A., Beck, R., Mitra, D., and Scaife, A. M. M.: 2016, *A&A* **592**, A123 87

Nagar, N. M., Falcke, H., and Wilson, A. S.: 2005, *A&A* **435**, 521 77

Narayan, R., Igumenshchev, I. V., and Abramowicz, M. A.: 2000, *ApJ* **539**, 798 76

Narayan, R., Mahadevan, R., Grindlay, J. E., Popham, R. G., and Gammie, C.: 1998, *The Astrophysical Journal* **492(2)**, 554 77

Narayan, R. and Yi, I.: 1995, *ApJ* **452**, 710 4, 76, 77, 86

Neilsen, J., Nowak, M. A., Gammie, C., Dexter, J., Markoff, S., Haggard, D., Nayakshin, S., Wang, Q. D., Grosso, N., Porquet, D., Tomsick, J. A., Degenaar, N., Fragile, P. C., Houck, J. C., Wijnands, R., Miller, J. M., and Baganoff, F. K.: 2013, *ApJ* **774**, 42 72

Nord, M. E., Lazio, T. J. W., Kassim, N. E., Goss, W. M., and Duric, N.: 2004, *ApJ* **601**, L51 72

Novikov, I. D., Pethick, C. J., and Polnarev, A. G.: 1992, *MNRAS* **255**, 276 13

Nowak, M. A., Neilsen, J., Markoff, S. B., Baganoff, F. K., Porquet, D., Grosso, N., Levin, Y., Houck, J., Eckart, A., Falcke, H., Ji, L., Miller, J. M., and Wang, Q. D.: 2012, *ApJ* **759**, 95 74

Orszag, S. A. and Tang, C.-M.: 1979, *Journal of Fluid Mechanics* **90**, 129 39

Phinney, E. S.: 1989, in M. Morris (ed.), *The Center of the Galaxy*, Vol. 136 of *IAU Symposium*, p. 543 16, 17

Piran, T., Sadowski, A., and Tchekhovskoy, A.: 2015a, *MNRAS* **453**, 157 17, 18, 20

Piran, T., Svirski, G., Krolik, J., Cheng, R. M., and Shiokawa, H.: 2015b, *ApJ* **806**, 164 20

Ponti, G.: 2012, *X-ray monitoring of Sgr A* during outburst*, Chandra Proposal 82

Ponti, G., Hofmann, F., Churazov, E., Morris, M., Haberl, F., Nandra, K., Terrier, R., Clavel, M., and Goldwurm, A.: 2019, *Nature* **567**, 347 7, 83, 84, 85, 89, 91, 93, 94

Ponti, G., Morris, M. R., Terrier, R., Haberl, F., Sturm, R., Clavel, M., Soldi, S., Goldwurm, A., Predehl, P., Nandra, K., Bélanger, G., Warwick, R. S., and Tatischeff, V.: 2015, *MNRAS* **453**, 172 7, 81, 82, 83, 89, 91, 93, 94

Price, D.: 2005, *Ph.D. thesis*, PhD Thesis, 2005 24, 25, 26, 27, 28, 29

Price, D. J.: 2011, in J. Alves, B. G. Elmegreen, J. M. Girart, and V. Trimble (eds.), *Computational Star Formation*, Vol. 270 of *IAU Symposium*, pp 169–177 7

Price, D. J.: 2012a, *Journal of Computational Physics* **231**, 759 23

Price, D. J.: 2012b, in R. Capuzzo-Dolcetta, M. Limongi, and A. Tornambè (eds.), *Advances in Computational Astrophysics: Methods, Tools, and Outcome*, Vol. 453 of *Astronomical Society of the Pacific Conference Series*, p. 249 32

Price, D. J. and Monaghan, J. J.: 2004, *MNRAS* **348**, 139 34

Price, D. J., Wurster, J., Nixon, C., Tricco, T. S., Toupin, S., Pettitt, A., Chan, C., Laibe, G., Glover, S., Dobbs, C., Nealon, R., Liptai, D., Worpel, H., Bonnerot, C., Dipierro, G., Ragusa, E., Federrath, C., Iaconi, R., Reichardt, T., Forgan, D., Hutchison, M., Constantino, T., Ayliffe, B., Mentiplay, D., Hirsh, K., and Lodato, G.: 2017, *PHANTOM: Smoothed particle hydrodynamics and magnetohydrodynamics code*, Astrophysics Source Code Library 6, 7, 31, 32, 33, 34, 39, 42, 43, 44, 92

Pringle, J. E.: 1981, *ARA&A* **19**, 137 20

Quataert, E. and Loeb, A.: 2005, *ApJ* **635**, L45 82

Ramirez-Ruiz, E. and Rosswog, S.: 2009, *ApJ* **697**, L77 20

Raymond, S. N.: 2014, *Hill Radius/Sphere*, pp 1–1, Springer Berlin Heidelberg, Berlin, Heidelberg 48

Rees, M. J.: 1988, *Nature* **333**, 523 2, 3, 4, 5, 6, 9, 10, 14, 15, 16, 17, 18, 20, 45, 51, 53, 57, 58, 63, 66, 69, 85, 92

Reid, M. J. and Brunthaler, A.: 2004, *ApJ* **616**, 872 72

Reid, M. J., Readhead, A. C. S., Vermeulen, R. C., and Treuhaft, R. N.: 1999, *ApJ* **524**, 816 72

Reynolds, S. P. and McKee, C. F.: 1980, *ApJ* **239**, 893 78

Richtmyer, R. D. and Dill, E. H.: 1959, *Physics Today* **12**, 50 29

Roberts, D. A. and Goss, W. M.: 1993, *ApJS* **86**, 133 72

Robertson, B. E., Kravtsov, A. V., Gnedin, N. Y., Abel, T., and Rudd, D. H.: 2010, *MNRAS* **401**, 2463 40, 41

Rosswog, S., Ramirez-Ruiz, E., and Hix, W. R.: 2009, *ApJ* **695**, 404 20

Roy, S. and Pramesh Rao, A.: 2004, *MNRAS* **349**, L25 72

Saitoh, T. R. and Makino, J.: 2009, *ApJ* **697**, L99 37

Schmutzler, T. and Tscharnuter, W. M.: 1993, *A&A* **273**, 318 94

Schödel, R., Morris, M. R., Muzic, K., Alberdi, A., Meyer, L., Eckart, A., and Gezari, D. Y.: 2011, *A&A* **532**, A83 73

Schödel, R., Ott, T., Genzel, R., Hofmann, R., Lehnert, M., Eckart, A., Mouawad, N., Alexander, T., Reid, M. J., Lenzen, R., Hartung, M., Lacombe, F., Rouan, D., Gendron, E., Rousset, G., Lagrange, A.-M., Brandner, W., Ageorges, N., Lidman, C., Moorwood, A. F. M., Spyromilio, J., Hubin, N., and Menten, K. M.: 2002, *Nature* **419**, 694 72

Schwarzschild, K.: 1916, *Abh. Konigl. Preuss. Akad. Wissenschaften Jahre 1906,92, Berlin,1907* 1916 34

Sedov, L.: 1959, in L. Sedov (ed.), *Similarity and Dimensional Methods in Mechanics*, pp 305 – 353, Academic Press 37

Serabyn, E., Lacy, J. H., Townes, C. H., and Bharat, R.: 1988, *ApJ* **326**, 171 72

Shakura, N. I. and Sunyaev, R. A.: 1973, *A&A* **24**, 337 17

Sharma, P., Quataert, E., and Stone, J. M.: 2007, *ApJ* **671**, 1696 75

Shcherbakov, R. V. and Baganoff, F. K.: 2010, *The Astrophysical Journal* **716(1)**, 504 78

Shen, R.-F. and Matzner, C. D.: 2014, *The Astrophysical Journal* **784(2)**, 87 14, 17

Shiokawa, H., Krolik, J. H., Cheng, R. M., Piran, T., and Noble, S. C.: 2015, *ApJ* **804**, 85 20

Sod, G. A.: 1978, *Journal of Computational Physics* **27(1)**, 1 35

Spitzer, L.: 1987, *Dynamical evolution of globular clusters* 11

Stone, J. M., Gardiner, T. A., Teuben, P., Hawley, J. F., and Simon, J. B.: 2008, *ApJS* **178**, 137 39, 42

Stone, J. M. and Norman, M. L.: 1992, *ApJS* **80**, 753 36

Strong, A. W., Porter, T. A., Digel, S. W., Jóhannesson, G., Martin, P., Moskalenko, I. V., Murphy, E. J., and Orlando, E.: 2010, *The Astrophysical Journal* **722(1)**, L58 86

Strubbe, L. E. and Quataert, E.: 2009, *MNRAS* **400**, 2070 3, 17, 59

Su, M., Slatyer, T. R., and Finkbeiner, D. P.: 2010, *ApJ* **724**, 1044 80, 88, 90, 93

Su, M., Slatyer, T. R., and Finkbeiner, D. P.: 2010, *The Astrophysical Journal* **724(2)**, 1044 84, 86

Svirski, G., Piran, T., and Krolik, J.: 2017, *MNRAS* **467**, 1426 20

Syer, D. and Ulmer, A.: 1999, *MNRAS* **306**, 35 2, 3, 13

Taylor, G.: 1950, *Proceedings of the Royal Society of London Series A* **201**, 159 37

Tejeda, E., Gafton, E., Rosswog, S., and Miller, J. C.: 2017, *MNRAS* **469**, 4483 3, 48, 55

Tejeda, E. and Rosswog, S.: 2013, *MNRAS* **433**, 1930 3, 34

Thacker, R. J. and Couchman, H. M. P.: 2006, *Computer Physics Communications* **174(7)**, 540 42

Tomisaka, K. and Ikeuchi, S.: 1986, *PASJ* **38**, 697 83

Tóth, G.: 2000, *Journal of Computational Physics* **161**, 605 41

Tremaine, S., Gebhardt, K., Bender, R., Bower, G., Dressler, A., Faber, S. M., Filippenko, A. V., Green, R., Grillmair, C., Ho, L. C., Kormendy, J., Lauer, T. R., Magorrian, J., Pinkney, J., and Richstone, D.: 2002, *ApJ* **574**, 740 6, 10

Treumann, R. A.: 2009, *The Astronomy and Astrophysics Review* **17(4)**, 409 79

Ulmer, A.: 1999, *ApJ* **514**, 180 4, 18

Van Den Bergh, S.: 1982, *Science* **218**, 992 76

Verlet, L.: 1967, *Phys. Rev.* **159**, 98 32

Wang, J. and Merritt, D.: 2004, *ApJ* **600**, 149 2, 12, 13, 17, 46

Wang, Q. D., Nowak, M. A., Markoff, S. B., Baganoff, F. K., Nayakshin, S., Yuan, F., Cuadra, J., Davis, J., Dexter, J., Fabian, A. C., Grosso, N., Haggard, D., Houck, J., Ji, L., Li, Z., Neilsen, J., Porquet, D., Ripple, F., and Shcherbakov, R. V.: 2013, *Science* **341(6149)**, 981 75, 78, 82

Widrow, L. M. and Dubinski, J.: 2005, *The Astrophysical Journal* **631(2)**, 838 42

Widrow, L. M., Pym, B., and Dubinski, J.: 2008, *The Astrophysical Journal* **679(2)**, 1239 42

Willson, L. A., Bowen, G. H., and Struck-Marcell, C.: 1987, *Comments on Astrophysics* **12**, 17 68

Wu, C. C.: 1988, *J. Geophys. Res.* **93**, 987 35

Wurster, J. and Thacker, R. J.: 2013, *MNRAS* **431**, 2513 42

Yang, H.-Y. K., Ruszkowski, M., Ricker, P. M., Zweibel, E., and Lee, D.: 2012, *The Astrophysical Journal* **761(2)**, 185 84, 85, 86, 87, 89, 90, 93

Young, P. J., Shields, G. A., and Wheeler, J. C.: 1977, *ApJ* **212**, 367 2

Yuan, F., Quataert, E., and Narayan, R.: 2003, *ApJ* **598**, 301 78

Yuan, F., Quataert, E., and Narayan, R.: 2004, *ApJ* **606**, 894 78

Yusef-Zadeh, F., Roberts, D. A., Goss, W. M., Frail, D. A., and Green, A. J.: 1996, *ApJ* **466**, L25 79

Zhao, J.-H., Blundell, R., Moran, J. M., Downes, D., Schuster, K. F., and Marrone, D. P.: 2010, *ApJ* **723**, 1097 72

Zhao, J.-H., Morris, M. R., and Goss, W. M.: 2016, *ApJ* **817(2)**, 171 83

Zhao, J.-H., Young, K. H., Herrnstein, R. M., Ho, P. T. P., Tsutsumi, T., Lo, K. Y., Goss, W. M., and Bower, G. C.: 2003, *The Astrophysical Journal Letters* **586(1)**, L29 72

Zirakashvili, V.: 2014, *Nuclear Physics B - Proceedings Supplements* **256-257**, 101 , Cosmic Ray Origin – Beyond the Standard Models 86

Zubovas, K., Nayakshin, S., and Markoff, S.: 2012, *MNRAS* **421**, 1315 78

Zylka, R. and Mezger, P. G.: 1988, *A&A* **190**, L25 72

UNIVERSIDADE DE ÉVORA
INSTITUTO DE INVESTIGAÇÃO
E FORMAÇÃO AVANÇADA

Contactos:
Universidade de Évora
Instituto de Investigação e Formação Avançada — IIFA
Palácio do Vimioso | Largo Marquês de Marialva, Apart. 94
7002 - 554 Évora | Portugal
Tel: (+351) 266 706 581
Fax: (+351) 266 744 677
email: iifa@uevora.pt